DISSERTATION

SPIN WAVES IN MAGNETIC THIN FILMS: NEW TYPES OF SOLITONS AND ELECTRICAL CONTROL

Submitted by

Zihui Wang

Department of Physics

In partial fulfillment of the requirements

For the Degree of Doctor of Philosophy

Colorado State University

Fort Collins, Colorado

Spring 2017

Doctoral Committee:

Advisor: Mingzhong Wu

Carl Patton
Richard Eykholt
Robert E. Camley
Mario C. Marconi

ABSTRACT

SPIN WAVES IN MAGNETIC THIN FILMS: NEW TYPES OF SOLITONS AND ELECTRICAL CONTROL

New types of spin-wave solitons in magnetic thin films and the methods to control spin waves electrically are studied in this thesis. In the first part, the first observation of chaotic spin-wave solitons in yttrium iron garnet (YIG) thin film-based active feedback rings is presented. At some ring gain levels, one observes the self-generation of a single spin-wave soliton pulse in the ring. When the pulse circulates in the ring, its amplitude varies chaotically with time. The excitation of dark spin-wave envelope solitons in YIG thin film strips is also described. The formation of a pair of black solitons with a phase jump of 180^{o} is observed for the first time. The excitation of bright solitons in the case of repulsive nonlinearity is also observed and is reproduced by a numerical simulation based on a high-order nonlinear Schrödinger equation.

In the second part, the control of magnetization relaxation in ferromagnetic insulators via interfacial spin scattering is presented. In the experiments nanometer-thick YIG/Pt bi-layered structures are used, with the Pt layer biased by an electric voltage. The bias voltage produces a spin current across the Pt layer thickness due to the spin Hall effect. As this current scatters off the YIG surface, it exerts a torque on the YIG surface spins. This torque can reduce or increase the damping and thereby compress or broaden the ferromagnetic resonance linewidth of the YIG film, depending on the field/current configuration. The control of spin waves in a YIG thin film via interfacial spin scattering is also presented. In the experiments a 4.6-μm-thick YIG film strip

with a 20-nm-thick Pt capping layer is used. A DC current pulse is applied to the Pt layer and produced a spin current across the Pt layer. As the spin current scatters off the YIG surface, it can either amplify or attenuate spin-wave pulses that travel in the YIG strip, depending on the current/field configuration.

ACKNOWLEDGEMENTS

There are many people to whom I would like to express my gratitude for their helps and support during my graduate study.

First of all, I would like to sincerely and gratefully thank my advisor Dr. Mingzhong Wu. Without his guidance, help, and encouragement, this thesis would have not been possible. Without the countless efforts and time he spent on me, I cannot imagine that my graduate study can be anywhere close as fruitful as it has been. His very positive lifestyle has greatly shaped my attitude, towards both work and life.

I would also like to thank all of the members of the CSU Magnetic Lab. I very much appreciated their friendships as well as great advices and collaborations. I am especially grateful for Dr. Boris Kalinikos, who spent a lot of time with me sitting in the lab and teaching me hand by hand how to do experiments and provide me with a foundation of knowledge in spin waves and solitons. I am also grateful for Dr. Carl E. Patton, who has always been encouraging and has set an excellent example of a successful scientist. I also want to thank Dr. Patton for his prudent comments and editing of this thesis. I also thank Dr. Tong Wei and Dr. Young-Yeal Song, who had taught me a lot of basic knowledge on magnetism and experimental techniques. Additionally, I want to thank Yiyan Sun, who prepared numerous samples for this study, Aaron Hagerstrom, who helped with the calculations of the correlation dimensions and Lyapunov exponents of chaotic signals, as well as Mike Kabatek and Praveen Janantha, who helped edit this thesis.

Last but not least, to all of my friends and family, my parents, as well as my grandmother, each of you can share in this accomplishment. Without your support, I would not have been able to complete this work.

TABLE OF CONTENTS

ABSTRACT ii

ACKNOWLEDGEMENTS iv

1. OVERVIEW 1

1.1 Background and motivations 1

1.2 Thesis overview 2

2. INTRODUCTION TO SPIN WAVE THEORY AND EXPERIMENT 3

2.1 Uniform precession mode 3

2.2 Propagating spin-wave mode 6

2.2.1 Spin-wave dispersion relation in an unbounded medium 6

2.2.2 Spin-wave dispersion relation in a bounded medium 9

2.3 Introduction to nonlinear spin waves 12

2.3.1 Nonlinear coefficients for different types of spin waves 12

2.3.2 Introduction to nonlinear Schrödinger equation 14

2.3.3 Soliton solutions of the nonlinear Schrödinger equation 17

2.4 Excitation and detection of spin waves in magnetic thin films 20

2.5 Ferromagnetic resonance system 23

3. ELETCTIC CONTROL OF MANGETIZATION RELAXATION 26

3.1 Introduction to the spin Hall effect 26

3.2 Control of magnetization relaxation 28

3.3 Experimental configurations and parameters 30

3.4 Experimental results 32

4. CONTROL OF SPIN-WAVE AMPLITUDE IN FERRIMAGNETIC INSULATORS 39
4.1 Spin wave damping and parametric pumping 39
4.2 Amplification of spin waves through interfacial spin scattering 40
4.3 Experimental configuration and parameters 42
4.4 Experimental results and discussions 44
4.5 Control of spin waves with large input currents 52
5. CHAOTIC SPIN-WAVE SOLITONS IN MAGNETIC FILM FEEDBACK RINGS 64
5.1 Introduction to chaotic spin-wave solitons 64
5.2 Magnetic film active feedback rings 66
5.3 Experimental observation of chaotic solitons 68
5.4 Numerical simulations of chaotic solitons 73
6. OBSERVATION OF SPIN-WAVE DARK SOLITON PAIRS IN YTTRIUM IRON GARNET THIN FILMS 77
6.1 Introduction 77
6.2 Experiment setup and parameters 79
6.3 Experiment results on black solitons 81
7. FORMATION OF BRIGHT SOLITONS FORM WAVE PACKETS WITH REPULSIVE NONLINEARITY 90
7.1 Introduction 90
7.2 Experimental results obtained with transducer structures 91
7.3 Experiment results obtained with a scanning probe 94
7.4 Simulation results with modified NLS equation 98
8. SUMMARY AND OUTLOOK 102

8.1 Summary and conclusion.....102

8.2 Future work.....103

REFERENCES 105

CHAPTER 1

OVERVIEW

1.1 Background and motivations

Magneto-static spin waves (MSW) which propagate in magnetic thin films, such as yttrium iron garnet (YIG) thin films, have been extensively studied in the past decades for two main reasons. First, MSW in YIG films are well suited for investigation of nonlinear wave properties due to their low loss and low power thresholds for nonlinear excitations. A wide variety of nonlinear wave phenomena have already been studied in MSW systems. These include the studies of envelope soliton excitations (for example: Kalinikos, Kovshikov, and Slavin, 1983; Wu, Kalinikos, and Patton, 2004; Scott, Kostylev, Kalinikos, and Patton, 2005), soliton fractals (Wu, Kalinikos, Carr, and Patton, 2006), chaotic excitations (Wu, Kalinikos, and Patton, 2005; Hagerstrom, Tong, Wu, Kalinikos, and Eykholt, 2009), and modulational instability (Wu and Kalinikos, 2008), among others. Aside from nonlinear dynamics studies, the potential applications of MSW-based devices have also been extensively studied. These devices include nonlinear spin-wave phase shifters (Ustinov and Kalinikos, 2008), nonlinear microwave interferometers (Ustinov and Kalinikos, 2007), and broad-band chaotic oscillators (Hagerstrom, Wu, Eykholt, and Kalinikos, 2011), among others. Beside these more traditional applications of MSW in microwave devices, there has also been a tremendous growth of interest very recently in spin wave-based spintronic devices. This growth is attributed to the fact that spin waves in insulating magnetic materials are an idea carrier of spin currents due to the magnetic material's low energy dissipation (Liu and Vignale, 2011). Therefore, such spintronic devices have the potential to be smaller and more energy efficient than traditional electronic circuits.

The motivations for this investigation are twofold. From the fundamental point of view, even after decades of extensive research, the nonlinear dynamics of spin waves are still not fully understood. Previous studies of nonlinear spin waves have mostly been conducted under the scope of the nonlinear Schrödinger equation. However, the use of a more complex model leads to more enriched possibilities (Akhmediev, Soto-Crespo, and Town, 2001). On the other hand, recent advances in spintronic (Takahashi, Saitoh, and Maekawa, 2009; Liu, Moriyama, Ralph, and Buhrman, 2011; Kajiwara, *et al.*, 2010) have opened a new area for the study of spin waves and spin wave-based devices. In spite of the promising future for the applications of those spin wave-based spintronic devices, a number of fundamental questions are still unanswered. These questions include the reduction of spin-wave damping, electronic control of spin waves, efficient spin injections and detections, and many others.

1.2 **Thesis overview**

This thesis is organized into eight chapters. The first chapter addresses the motivations and overview for this study. The second chapter gives a brief introduction to both linear and nonlinear spin-wave theories, and also the experimental methods used to study spin waves. Chapter three and Chapter four discuss the experimental control of magnetization relaxation and spin-wave amplitude based on the spin Hall effect. Chapter five to Chapter seven are devoted to discussions on the experimental and numerical studies of nonlinear spin wave phenomena which include chaotic solitons, black soliton excitations, and excitations of bright solitons in repulsive nonlinear media. Chapter eight gives the conclusions of the thesis and an outlook for future studies.

CHAPTER 2

INTRODUCTION TO SPIN WAVE THEORY AND EXPERIMENT

2.1 Uniform precession mode

If considering a classical picture of an atom, i.e. an electron on a circular orbit around a nucleus, one finds that the electron's angular momentum gives rise to a magnetic moment. In addition to orbital angular momentum, the electron also possesses spin angular momentum, which is of quantum mechanical origin. Generally speaking, the total magnetic moment of the atom can be obtained by the combination of the orbital and spin angular momenta which follows the equation (Hook and Hall, 1991):

$$\boldsymbol{\mu} = -\mu_{\mathrm{B}}(\mathbf{L} + 2\mathbf{S})/\hbar \tag{2.1}$$

where **L** and **S** are the quantum numbers for the orbital and spin angular momenta of the atom, and μ_{B} is Bohr magneton, which is the magnitude of the magnetic dipole moment of an orbiting electron with an orbital angular moment of one $\hbar$.

The magnetization **M** is defined as net macroscopic magnetic moment per unit volume. If the magnetic momenta of all the atoms in a magnetic material are collinear, the magnetization **M** can be expressed in the following equation:

$$\mathbf{M} = \frac{\mathrm{N}}{\mathrm{V}}\boldsymbol{\mu} \tag{2.2}$$

Here V represents the volume of the magnetic material and N is the number of atoms. The potential energy density related to the magnetization **M** in the presence of a magnetic field **H** is given by:

$$E = -\mathbf{M}\cdot\mathbf{H} \tag{2.3}$$

This equation states that (1) the energy associated with the magnetization is minimized when the magnetization is parallel to an externally applied magnetic field, and (2) magnetic moments in the presence of an external applied magnetic field tend to align with the field. However, rather than simply aligning with the magnetic field due to this potential energy, the magnetization will experience a torque $\boldsymbol{\tau}$ which drives the magnetization to precess around the magnetic field. The equation that describes this rotational motion was introduced by (Laudau and Lifshitz, 1935):

$$\frac{d\mathbf{M}}{dt} = -|\gamma|\mathbf{M}\times\mathbf{H} \tag{2.4}$$

where $|\gamma|$ is the absolute electron gyromagnetic ratio. This equation is also called the magnetic torque equation. In the above equation both **M** and **H** have static and dynamic components:

$$\begin{aligned}\mathbf{M} &= \mathbf{M}_z + \mathbf{m}(t)\\ \mathbf{H} &= \mathbf{H}_{eff} + \mathbf{h}(t)\end{aligned} \tag{2.5}$$

where $\mathbf{m}(t)$ and $\mathbf{h}(t)$ are the dynamic components of magnetization and magnetic field, respectively. The dynamic components here are perpendicular to the static components for simplicity. $\mathbf{H}_{eff}$ is the effective magnetic field which is a combination of external field, demagnetization field, anisotropy field, and other magnetic fields if present. If one assumes $\mathbf{m}(t) = \mathbf{m}_\omega e^{i\omega t}$ and magnetic field is a uniform field along z direction $\mathbf{H} = \mathbf{e}_z H_{eff}$, one can solve the above torque equation and obtain,

$$\omega = \omega_0 \equiv |\gamma| H_{eff} \tag{2.6}$$

where ω_0 is the magnetization precession frequency about the static magnetic field. Also it is easy to realize from the above toque equation that $\frac{d\mathbf{M}}{dt}\cdot\mathbf{M} = 0$, which indicates $\frac{d|\mathbf{M}|^2}{dt} = 0$ or $|\mathbf{M}| = \text{constant}$. In other words, the magnitude of magnetization is a constant.

Now if one considers the response of magnetization with respect to a small dynamic magnetic field, the susceptibility of the magnetic material can then be calculated with a linear approximation of torque equation, i.e.

$$|\mathbf{m}_\omega| \ll |\mathrm{M}|, |\mathbf{h}_\omega| \ll \mathrm{H_{eff}} \tag{2.7}$$

One obtains,

$$\begin{pmatrix} \mathrm{m_x} \\ \mathrm{m_y} \\ \mathrm{m_z} \end{pmatrix} = \begin{pmatrix} \chi & \mathrm{i}\chi_\mathrm{a} & 0 \\ -\mathrm{i}\chi_\mathrm{a} & \chi & 0 \\ 0 & 0 & 0 \end{pmatrix} \begin{pmatrix} \mathrm{h_x} \\ \mathrm{h_y} \\ \mathrm{h_z} \end{pmatrix} \tag{2.8}$$

In this equation, $\chi = \frac{\omega_0 \omega_\mathrm{M}}{{\omega_0}^2 - \omega^2}$ and $\chi_\mathrm{a} = \frac{\omega_0 \omega}{{\omega_0}^2 - \omega^2}$, where ω_M is defined as $|\gamma| 4\pi |\mathbf{M}|$. It is interesting to see that when ω is very close to ω_0, the susceptibility will be approaching infinity, which means at this frequency, a small magnetic field will be able to drive a very large magnetization precession motion if damping is not considered. This frequency is called the ferromagnetic resonance frequency.

Now consider a thin magnetic film with an external magnetic field applied out of the film plane. In this case the ferromagnetic resonance frequency can be found in a very straightforward manner. The internal magnetic field is the applied field combined with demagnetization field,

$$\mathrm{H_{eff}} = \mathrm{H_{external}} - 4\pi \mathrm{M_s} \tag{2.9}$$

Here one does not consider the anisotropy field and assumes that the applied field is strong enough to overcome the demagnetization field and saturate the magnetic film. The resonance frequency is then given by,

$$\omega = |\gamma| (\mathrm{H_{external}} - 4\pi \mathrm{M_s}) \tag{2.10}$$

Now consider the case in which the magnetic field is applied in the film plane. Notice the fact

that the dynamic component of magnetization will have an out-of-plane component. As a result, a small dynamic demagnetization magnetic field will be generated. In this case, the resonance frequency is given by,

$$\omega = \sqrt{\omega_0(\omega_0 + \omega_M)} \tag{2.11}$$

2.2 **Propagating spin-wave mode**

In the last section, the discussion is only about uniform precession mode where all the magnetic moments are collinear and precess in phase throughout the entire sample. However, the magnetic moments are coupled to each other through dipole-dipole and/or exchange interactions. The result of these interactions can be seen if one excites some magnetic moments locally, the precession motion of those moments can propagate spatially in the magnetic material like a wave. This wave is therefore a collective excitation of magnetic moments and is usually termed as a spin wave. Spin waves in magnetic materials are analyzed by solving Maxwell's equations, which naturally take dipolar interactions into account, together with the magnetic torque equation and boundary conditions.

2.2.1 Spin-wave dispersion relation in an unbounded medium

In an unbounded sample, the spin-wave dispersion relation is solved by a combination of Maxwell's equations and the magnetic torque equation. For the unbounded case one takes the magneto-static wave approximation or slow wave approximation (Stancil, 1993). This approximation is taken because, over the frequency range which typical spin–wave experiments deal with, the spin-wave wavenumbers are much larger than those of electromagnetic waves. In other words, for a given wavenumber, the corresponding spin-wave frequency is much smaller than that of an electromagnetic wave. With this approximation, one can write the Maxwell's

equations for spin waves (magneto-static waves) as:

$$\begin{aligned} &\nabla \times \mathbf{h} = 0 \\ &\nabla \times \mathbf{b} = 0 \Rightarrow \nabla \cdot \mathbf{h} = -\nabla \cdot \mathbf{m} \end{aligned} \tag{2.12}$$

It is important to note that the Maxwell's equations are linear equations. Thus, one can write **m** and **h** in the following form,

$$\begin{aligned} \mathbf{m} &= \mathbf{m}_{\omega \mathrm{k}} \mathrm{e}^{\mathrm{i}(\mathbf{k}\cdot\mathbf{r}-\omega \mathrm{t})} \\ \mathbf{h} &= \mathbf{h}_{\omega \mathrm{k}} \mathrm{e}^{-\mathrm{i}(\mathbf{k}\cdot\mathbf{r}-\omega \mathrm{t})} \end{aligned} \tag{2.13}$$

By substituting **m** and **h** into (2.13), one can obtain the dipolar field generated by magnetic moment,

$$\mathbf{h}(\mathbf{r}, \mathrm{t}) = \mathbf{h}_{\omega \mathrm{k}} \mathrm{e}^{-\mathrm{i}(\mathbf{k}\cdot\mathbf{r}-\omega \mathrm{t})} = -\frac{\mathbf{k}(\mathbf{k} \cdot \mathbf{m}_{\omega \mathrm{k}})}{\mathrm{k}^2} \mathrm{e}^{-\mathrm{i}(\mathbf{k}\cdot\mathbf{r}-\omega \mathrm{t})} \tag{2.14}$$

The exchange field in a magnetic material can be written as

$$\mathbf{h}_{\mathrm{exch}}(\mathbf{r}, \mathrm{t}) = \lambda_{\mathrm{ex}} \nabla^2 \mathbf{m}(\mathbf{r}, \mathrm{t}) = -\lambda_{\mathrm{ex}} \mathrm{k}^2 \mathbf{m}_{\omega \mathrm{k}} \mathrm{e}^{-\mathrm{i}(\mathbf{k}\cdot\mathbf{r}-\omega \mathrm{t})} \tag{2.15}$$

where λ_{ex} is the exchange constant. For YIG materials, this value is $\partial = 3.2 \times 10^{-12} \mathrm{cm}^2$.

With the above approximations, the field can be written as,

$$\mathbf{H}_{\mathrm{eff}} = \mathbf{e_z} \mathrm{H_i} + \mathbf{h}(\mathrm{r}, \mathrm{t}) + \mathbf{h}_{\mathrm{exch}}(\mathrm{r}, \mathrm{t}) \tag{2.16}$$

One can now derive from the magnetic torque equation the following resonance frequency and propagation angle:

$$\begin{aligned} \omega^2 &= (\omega_{\mathrm{H}} + \omega_{\mathrm{M}} \partial \mathrm{k}^2)(\omega_{\mathrm{H}} + \omega_{\mathrm{M}} \partial \mathrm{k}^2 + \omega_{\mathrm{M}} \sin^2 \theta_{\mathrm{k}}) \\ \sin^2 \theta_{\mathrm{k}} &= \frac{\mathrm{k_x}^2 + \mathrm{k_y}^2}{\mathrm{k_x}^2 + \mathrm{k_y}^2 + \mathrm{k_z}^2} \end{aligned} \tag{2.17}$$

Figure 1 shows a schematic of the dispersion for two different θ_{k} values: 0° and 90°, where θ_{k} is the angle between spin wave propagation direction and the magnetic field direction.

Depending on the wavenumber value, the dispersion relation is separated into three different regions: (1) dipolar spin wave region, (2) the dipole-exchange wave region, and (3) the exchange wave region. Dipolar spin wave region roughly correspond to the region where the wavenumbers are below 10^4 rad/cm and above the lower limit below which the magneto-static approximation is invalid. In this region, the frequency has a weak dependence on the wavenumber. This region is the one in which most of the experiments in this study are carried out.

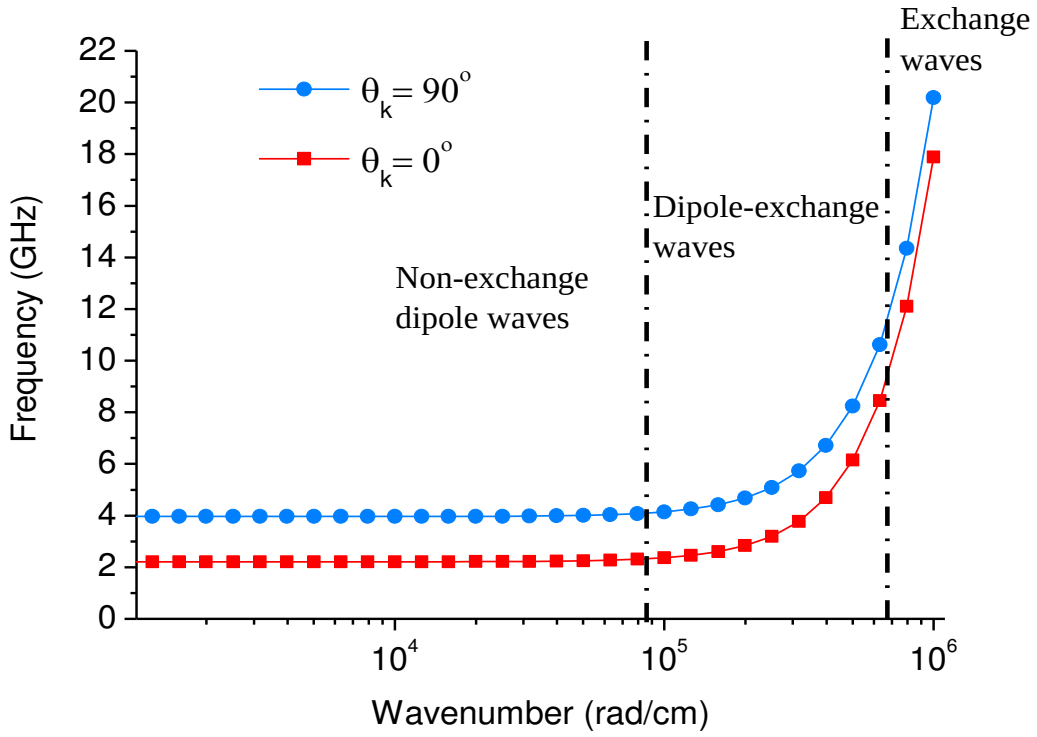

Figure 1. Dispersion relations for spin waves in an unbounded medium. The circles correspond to the case in which spin waves propagate in a direction perpendicular to the magnetic field direction, while the squares correspond to the case in which spin waves propagate in a direction parallel to the magnetic field direction. The calculations used H = 800 Oe, $4\pi\mathbf{M} = 1750$ G and $\lambda_{ex} = 3.2\times10^{-12}\,\mathrm{cm}^2$.

2.2.2 Spin-wave dispersion relation in a bounded medium

In this section, the main features of spin waves propagating in a long and narrow magnetic film strip are discussed. Three types of magnetic field/film configurations are considered which correspond to three different classes of spin waves. In all discussions below, the external static magnetic field is applied along the z-axis (as indicated in Figure 2) and the spin waves propagate along the film strip from left to right.

Consider first the geometry where a magnetic field is applied out of the film plane. In this case, the boundary conditions require $\mathbf{h}_{x,y}$ to be continuous across the upper and lower film surfaces, and b_z to be continuous across the upper and lower film surfaces. Also it is important to notice that the film thickness L is much smaller than the spin-wave decay length. Thus, spin waves will have reflections back and forth along z axis and the z-component of the wave vector k_z will be quantized. A detailed derivation can be carried out with the above boundary conditions, Maxwell's equations, and the magnetic torque equation. This derivation, however, will not be discussed here in details. For the lowest-order mode, a useful approximate dispersion relation has been derived by Kalinikos (Eshbach & Damon, 1960; Kalinikos, 1980),

$$\omega(k) = \sqrt{\omega_H \left[\omega_H + \omega_M \left(1 - \frac{1 - e^{-kd}}{kd} \right) \right]} \tag{2.18}$$

where k is the spin-wave wavenumber in the film plane and d is the thickness of the film. This notation is followed in the rest of this thesis unless otherwise specified. This type of spin waves is the so-called magneto-static forward volume waves. Several additional points should be made for forward volume waves. First of all, the notation "forward" comes from the fact that the group velocity is in the same direction as the phase velocity. This can be seen directly from

the positive slope of the dispersion curve. See Figure 2(a). The positive slope of the dispersion curve corresponds to a positive group velocity. "Volume" in the notation denotes that the spin-wave excitations are extended throughout the entire film thickness, as opposed to a surface mode (Stancil, 1993; Wu, 2011). Second, the slope of dispersion curve or group velocity is decreasing with an increase in wavenumber. One can define the dispersion coefficient as follows,

$$D = \frac{\partial^2 \omega(k)}{\partial k^2} \tag{2.19}$$

This dispersion coefficient has a negative value for forward volume spin waves. It should be mentioned that the sign of the dispersion coefficient is very important for the formation of solitons, as discussed in the following sections.

Forward volume waves have a rotation symmetry in the film plane due to the fact that the magnetic field is applied out of plane. If the magnetic field is applied tangentially, the symmetry is broken and one needs to consider the angle between the magnetic field and the wave vector (Stancil, 1993). Two special field/wave vector configurations are as follows: (1) the wave vector is parallel to the magnetic field direction and (2) the wave vector direction is perpendicular to the field.

The first configuration supports the propagation of backward volume waves. The dispersion relation can be derived using a similar method described above for forward volume waves. An approximate dispersion relation for the lowest-order mode has also been derived by Kalinikos (Kalinikos, 1980),

$$\omega(k) = \sqrt{\omega_H \left[\omega_H + \omega_M \left(\frac{1 - e^{-kd}}{kd} \right) \right]} \tag{2.20}$$

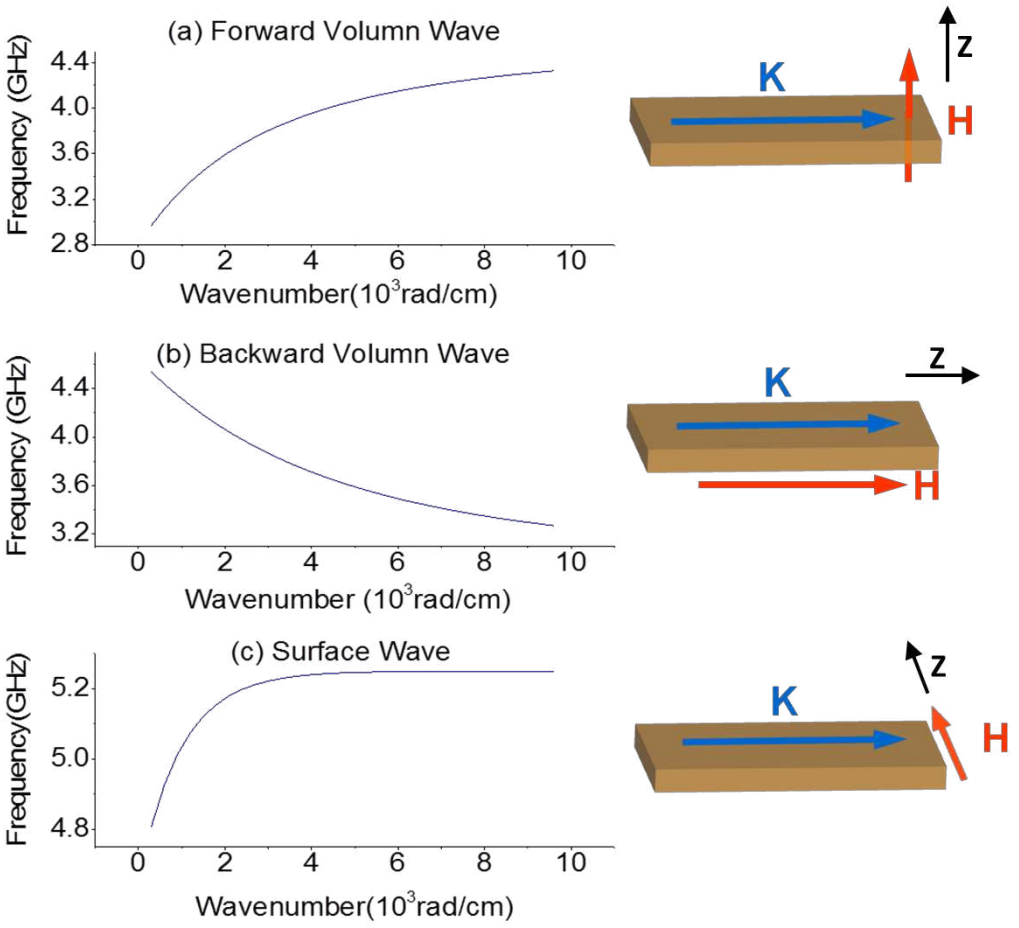

Figure 2. Examples of dispersion curves for: (a) magneto-static forward volume waves; (b) magneto-static backward volume waves; and (c) magneto-static surface waves. The calculations used H = 1000 Oe and $4\pi\mathbf{M} = 1750\,\mathrm{G}$.

Figure 2(b) shows an example of this dispersion curve. As opposed to forward volume waves, the phase velocity of the backward volume wave has an opposite sign with respect to the group velocity, which explains the "backward" nature of such waves. Also, the dispersion coefficient of the backward volume wave is positive.

The second configuration supports the propagation of surface waves. This configuration is different from forward and backward volume waves, because the wavenumber of surface waves in out-of- plane direction is imaginary. The meaning of this imaginary wavenumber is that the wave amplitude exponentially decays in this direction. In the case where k is larger than $1/d$,

spin waves propagate on one of the surfaces of the film. For the film/field configuration showed in Figure 2(c), the waves with a wave vector pointing to the right propagate along the top surface of the film while the waves with a wave vector pointing to the left propagate along the bottom surface of the film. Therefore, the surface waves are non-reciprocal waves (Wu, 2011). Also there is only a single propagating mode for surface waves instead of a series of modes with different thickness variations (Stancil, 1993). The dispersion relation equation for surface waves has also been derived by Kalinikos (Kalinikos, 1980),

$$\omega(k)=\sqrt{\omega_H\left(\omega_H+\omega_M\right)+\frac{\omega_M^2}{4}\left(1-e^{-2kd}\right)} \tag{2.21}$$

It is evident from Figure 2(c) that for surface waves the group velocity and the phase velocity are in the same direction, the same for forward volume waves. The dispersion coefficient of surface waves is negative. Note that the dispersion coefficient is negative for forward volume waves and positive for backward volume waves.

2.3 **Introduction to nonlinear spin waves**

2.3.1 Nonlinear coefficients for different types of spin waves

The discussions in the last two sections are based on the assumption that the input signal is small and the magnetization precesses at a small angle. For this reason, the values of ω_H and ω_M are calculated by using the saturation magnetization value $|\mathrm{M_s}|$ and all of these parameters are constant. However, when the spin-wave signal is strong and the magnetization precession angle is large, $\mathrm{M_s}$ in those equations has to be replaced by $\mathrm{M_z}$, which is the z-component of the magnetization (along the precession axis as indicated in Figure 2). An increase in spin-wave amplitude $|\mathbf{m}|$ leads to a decrease in $\mathrm{M_z}$, and the latter leads to a corresponding

change in spin-wave frequency. In other words, the spin-wave frequency not only depends on the wavenumber, but also on the spin-wave amplitude. The dependence of the spin-wave frequency on amplitude is the origin of spin-wave nonlinearity.

It is useful to define a complex, dimensionless function $u(t)$ to describe the amplitude and relative phase of a nonlinear spin wave. For forward volume waves, due to the fact that the precession is circular, one can write M_z as (Wu, 2011),

$$M_z \approx M_s\left(1-|u|^2\right) \tag{2.22}$$

Notice here that the Z axis is out of plane indicating that the $u(t)$ describe the spin wave amplitude in the plane. The spin-wave nonlinearity coefficient is then defined as,

$$N=\frac{\partial\omega}{\partial|u|^2} \tag{2.23}$$

For forward volume waves with ω close to ω_H, one can estimate the nonlinearity coefficient as (Wu, 2011),

$$N=\frac{\partial}{\partial|u|^2}\left[\gamma\left(H-4\pi M_z\right)\right]=\frac{\partial}{\partial|u|^2}\left[\gamma\left(H-4\pi M_s+4\pi M_s|u|^2\right)\right]=\omega_M \tag{2.24}$$

For surface wave and backward volume waves, due to the existents of demagnetizing field, the precession is elliptical instead of circular. As described in Figure 2, now the Z axis is in the plane and the dynamic magnetization has both in-plane and out-of-plane components. If we use $u(t)$ to describe the spin wave amplitude out of plane, in this case, M_z is given by

$$M_z=M_s\left[1-\frac{1}{2}\left(1+\frac{\omega_B^2}{\omega_H^2}\right)|u|^2\right] \tag{2.25}$$

The nonlinearity coefficient for both surface waves and backward volume waves with wavenumbers close to zero is given by,

$$N = \frac{\partial}{\partial |u|^2}\left[\gamma\sqrt{H\left(H+4\pi M_z\right)}\right] = -\frac{\omega_H \omega_M}{4\omega_B}\left(1+\frac{\omega_B^2}{\omega_H^2}\right) \tag{2.26}$$

However, if we define $u(t)$ as the spin wave amplitude in the film plane, then the nonli nearity coefficient is different which is given by,

$$N = -\frac{\omega_H \omega_M}{4\omega_B}\left(1+\frac{\omega_H^2}{\omega_B^2}\right) \tag{2.27}$$

Two important points are evident from the above equations. First, the nonlinearity coefficient for forward volume waves always has a positive value. In contrast, for both surface and backward volume waves the nonlinearity coefficient has a negative value. The physical meaning of these coefficients is straightforward: by increasing spin wave amplitude, it is expected that the spin-wave transmission band for a forward volume wave in the frequency domain shifts up, while that for a backward wave or a surface wave in the frequency domain shifts down. Second, the nonlinearity coefficient is not constant. Rather, it depends on both the saturation magnetization and the magnetic field magnitude.

It should be noted that the product of the signs of the dispersion coefficient (D) and nonlinearity coefficient (N) gives rise to different types of spin-wave nonlinearity. It is said that a spin wave has repulsive nonlinearity when $DN>0$ and attractive nonlinearity when $DN<0$. The reason for those definitions is explained in the next section.

2.3.2 Introduction to nonlinear Schrödinger equation

One can use the nonlinear Schrödinger (NLS) equation to describe the propagation of nonlinear spin waves in magnetic thin films. There exist two methods for the derivation of the NLS equation for nonlinear spin waves. The first method is based on the Taylor expansion of

the dispersion relation, which is well documented by Scott (Scott, 2002). The other method is based on the Hamiltonian formulation of spin-wave dynamics which is discussed below.

A very good review of the Hamiltonian formulation of spin waves is given by (Krivosik and Patton, 2010). Instead of using the magnetic torque equation, a scalar Hamiltonian form in terms of canonical variables is used to solve the problem of spin-wave dynamic. Following the notation by (Krivosik and Patton, 2010), the spin-wave dynamical equation is given by the Hamiltonian equation,

$$i\frac{da_{\mathbf{k}}(t)}{dt}=\frac{\partial \mathcal{U}}{\partial a_{\mathbf{k}}^{*}(t)} \quad -i\frac{da_{\mathbf{k}}^{*}(t)}{dt}=\frac{\partial \mathcal{U}}{\partial a_{\mathbf{k}}(t)} \tag{2.28}$$

Here $a_{\mathbf{k}}(t)$ and $a_{\mathbf{k}}^{*}(t)$ are obtained by a series of canonical transformations from the magnetization component **M,** and are the complex amplitude of a plane spin wave with a propagation direction defined by **k**. $\mathcal{U}$ is converted from the magnetic system's Hamiltonian $\mathcal{H}$ which has the unit of frequency,

$$\mathcal{U}=\frac{|\gamma|\mathcal{H}}{M_s V} \tag{2.29}$$

The effective magnetic field $\mathbf{H}_{\text{eff}}$ is connected with Hamiltonian $\mathcal{H}$ through,

$$\mathbf{H}_{\text{eff}}=-\frac{1}{V}\frac{\delta \mathcal{H}}{\delta \mathbf{M}} \tag{2.30}$$

In general, if one takes the Taylor expansion $\mathcal{U}$ as a function of $a_{\mathbf{k}}(t)$ and $a_{\mathbf{k}}^{*}(t)$, only the first-order terms are significant and can be written as,

$$\mathcal{U}=\mathcal{U}^{(2)}+\mathcal{U}^{(3)}+\mathcal{U}^{(4)}+... \tag{2.3}$$

where $\mathcal{U}^{(2)}$ leads to the linear spin-wave dispersion, $\mathcal{U}^{(3)}$ leads to so-called three-wave processes, and $\mathcal{U}^{(4)}$ leads to so-called four-wave process.

If three-wave processes are non-resonant (in other words, the magnetic field is sufficiently high so that the Suhl first-order spin-wave instability is prohibited), the three-wave interaction term in the Hamiltonian can then be folded. Then Equation (2.31) can be written as (Krivosik and Patton, 2010),

$$\mathcal{H} = \int \omega_{\mathbf{k}} a_k^* a_{\mathbf{k}} d\mathbf{k} + \frac{1}{2}\int T_{1234} a_1^* a_2^* a_3 a_4 \delta(\mathbf{k}_1 + \mathbf{k}_2 - \mathbf{k}_3 - \mathbf{k}_4) d\mathbf{k}_1 d\mathbf{k}_2 d\mathbf{k}_3 d\mathbf{k}_4 \quad (2.32)$$

If one substitutes this Hamiltonian into Equation (2.28), one obtains the following equation for spin-wave dynamics (Bouchbinder, 2003),

$$i\frac{\partial a_{\mathbf{k}}}{\partial t} - \omega_{\mathbf{k}} a_{\mathbf{k}} = \frac{1}{2}\int T_{\mathbf{k}123} a_1^* a_2 a_3 \delta(\mathbf{k} + \mathbf{k}_1 - \mathbf{k}_2 - \mathbf{k}_3) d\mathbf{k}_1 d\mathbf{k}_2 d\mathbf{k}_3 \quad (2.33)$$

If one takes a Taylor expansion of $\omega_{\mathbf{k}}$ about $\mathbf{k}_0$ and assumes $\mathbf{k} = \mathbf{k}_0 + \mathbf{q}$ and $|\mathbf{q}| \ll |\mathbf{k}_0|$, one obtains,

$$\omega_{\mathbf{k}} = \omega_0 + \mathbf{q}\cdot\mathbf{v} + \frac{1}{2} q_i q_j \left(\frac{\partial^2 \omega}{\partial k_i \partial k_j}\right) \quad (2.34)$$

where **v** is the group velocity. If one further assumes a one-dimensional wave propagation and considers the envelope $a_{\mathbf{k}}(t) = \exp(-i\omega_0 t)\varphi(q,t)$ where φ is the spin wave amplitude, we obtain:

$$[i\frac{\partial}{\partial t} - qv_g - \frac{q^2}{2}D]\varphi_q = \frac{1}{2}T_{0123}\int \varphi_1^* \varphi_2 \varphi_3 \delta(\mathbf{q} + \mathbf{q}_1 - \mathbf{q}_2 - \mathbf{q}_3) d\mathbf{q}_1 d\mathbf{q}_2 d\mathbf{q}_3 \quad (2.35)$$

If one then transforms this equation into the time domain and takes $N = \frac{1}{2}T_{0123}$, one obtains the famous NLS equation as

$$i[\frac{\partial\varphi}{\partial t} + v_g \frac{\partial\varphi}{\partial x}] + \frac{D}{2}\frac{\partial^2\varphi}{\partial x^2} - N|\varphi|^2\varphi = 0 \quad (2.36)$$

2.3.3 Soliton solutions of the nonlinear Schrödinger equation

The NLS equation admits the solution of a soliton – a large-amplitude pulse excitation that can propagate with constant shape and velocity in a nonlinear dispersive system. Physically, a soliton results from a fine balance between dispersion-caused pulse broadening and nonlinearity-associated self-narrowing.

The exact soliton solution of the NLS equation is determined by the sign of *DN*, which is the product of the dispersion and nonlinearity coefficients. When *DN* is negtive, the solution of the NLS equation is a bright soliton described by (Xia, kabos, Staudinger, Patton, and Slavin, 1998; Wu, 2011),

$$u(z,t) = u_0 \operatorname{sech}\left[u_0\sqrt{-\frac{N}{D}}(z - v_s t)\right]\exp\left[i(k_s z - \omega_s t)\right] \tag{2.37}$$

where u_0 is the peak amplitude, v_s is the soliton velocity, k_s is the wavenumber shift, and ω_s is the frequency shift. Note that k_s and ω_s are additions to the wavenumber and frequency of the original carrier wave. The soliton velocity v_s is given by

$$v_s = v_g + k_s D \tag{2.38}$$

where one usually has $|v_g| >> |k_s D|$. The frequency shift ω_s is given by

$$\omega_s = v_g k_s + \frac{1}{2} D k_s^2 + \frac{1}{2} N u_0^2 \tag{2.39}$$

Figure 3(a) shows the typical shape of a bright soliton. The soliton considered here is an envelope soliton. Namely, it is the envelope of the carrier spin wave that shows a soliton feature. The term ($k_s z$-$\omega_s t$) in Equation (2.37) represents the extra phase added to the original carrier phase of the overall wave packet. One can see form Equation (2.39) that, as a result of *DN being negtive*, the frequency shift due to the dispersion is compensated by the frequency shift

due to the nonlinearity. The net result is that the phase change across the center of a bright soliton is constant.

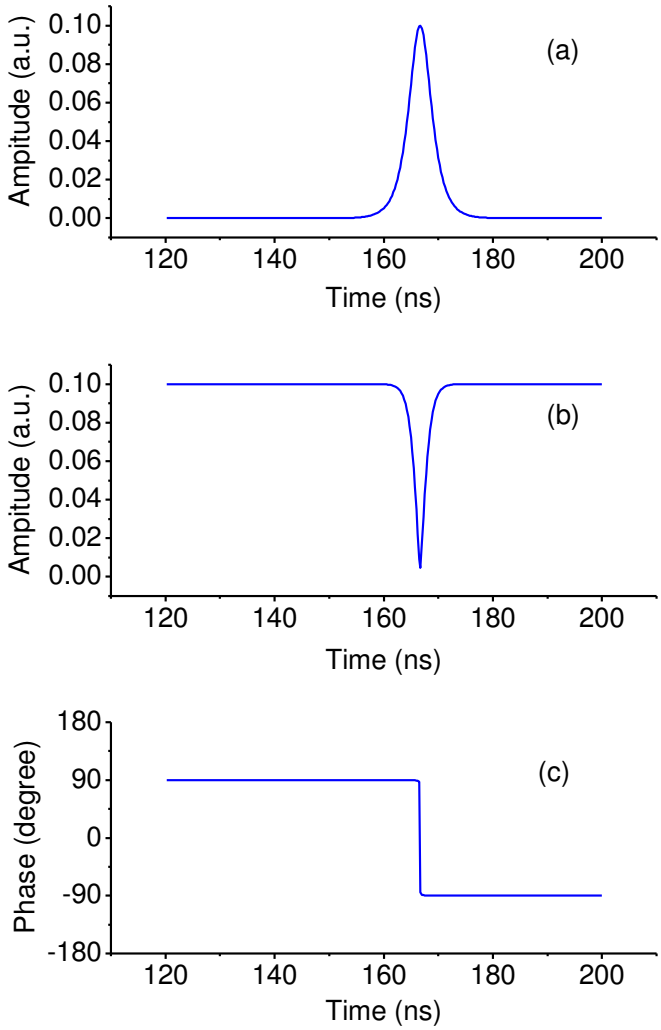

Figure 3. (a) Example of a bright soliton. (b) Example of a black soliton. (c) The phase response of a black soliton.

In the case of *DN* is positive, the NLS equation has a dark soliton solution given by (Lukomskii, 1978),

$$u(z,t)=u_0\left\{\sqrt{1-m^2}+im\tanh\left[mu_0\sqrt{\frac{N}{D}}(z-v_st)\right]\right\}\exp\left[i\left(k_s-\sqrt{1-m^2}u_0\sqrt{\frac{N}{D}}\right)z-i\omega_st\right] \quad (2.40)$$

where m denotes the depth of the dip relative to the amplitude of the continuous wave background and is given by

$$m=\frac{u_0^2-u_{\min}^2}{u_0^2} \quad (2.41)$$

where u_0 is the amplitude of the background wave and the $u_{\min}$ is the wave amplitude at the dip center.

The frequency shift ω_s is given by

$$\omega_s=v_gk_s+\frac{1}{2}Dk_s^2+\frac{1}{2}Nu_0^2(3-m^2)-\sqrt{1-m^2}u_0\sqrt{\frac{N}{D}}v_g \quad (2.42)$$

The shape of a dark soliton is given by

$$|u(z,t)|=u_0\sqrt{1-m^2\operatorname{sech}^2\left[mu_0\sqrt{\frac{N}{D}}(z-v_st)\right]} \quad (2.43)$$

The phase of a dark soliton is

$$\phi(z,t)=\arctan\left\{\frac{m}{\sqrt{1-m^2}}\tanh\left[mu_0\sqrt{\frac{N}{D}}(z-v_st)\right]\right\} \quad (2.44)$$

It can be seen from the above equations that m is actually a critical parameter. When m=1, the amplitude level at the center of a dark soliton goes to zero, and the phase shift at the soliton center equals exactly to 180°. In this special case, the soliton is called a black soliton. See Figs. 3(b) and 3(c). When m is smaller than 1, the amplitude at the soliton center is larger than zero, and the phase shift is less than 180°. In this case, the soliton is termed as a gray soliton.

It is important to emphasize that, from the NLS equation model, only bright solitons are allowed when *DN* is negtive and only black solitons are allowed when *DN* is positive. Therefore, in the surface spin wave configuration, one will only be able to excite dark solitons because bright solitons are not allowed due to the fact that for this configuration both the dispersion and nonlinearity coefficients are negative. For forward and backward volume waves, however, the two coefficients have opposite signs and one can excite bright solitons only.

2.4 **Excitation and detection of spin waves in magnetic thin films**

This section provides a brief overview of the experimental method utilized in this thesis for the excitation and detection of spin waves in magnetic thin films. Specifically, spin-wave detection using microstrip transducers and inductive probes is discussed.

Microstrip antennas are the most commonly used structures for the excitation and detection of spin waves. A microstrip antenna typically consists of a narrow metal strip deposited on a low-loss dielectric substrate. The other side of the dielectric substrate is a continuous metal layer which serves as the ground plane of the structure. A via is made at the end of the microstrip element across the dielectric substrate to connect the microstrip to the ground plane. An SMA (SubMininature version A) connecter is often used for external connection to the microstrip antenna. Due to the fact that the microstrip element can be easily manufactured in any shape, a microstrip antenna is one of the most useful antennas at microwave frequencies.

Figure 4 shows the typical configuration of a spin-wave excitation and detection setup based on a pair of microstrip transducer antennas. The microstrip antennas are placed so that the microstrip elements are in close contact with the magnetic film surface. The magnetic moments in the area close to an antenna element can be excited due to the antenna-produced microwave

magnetic field. The wavenumber limit of the spin waves that a microstrip antenna can excite is determined by the width of the microstrip transducer. For a transducer element with a width of 50 μm, the maximum wavenumber is about 1000 rad/cm.

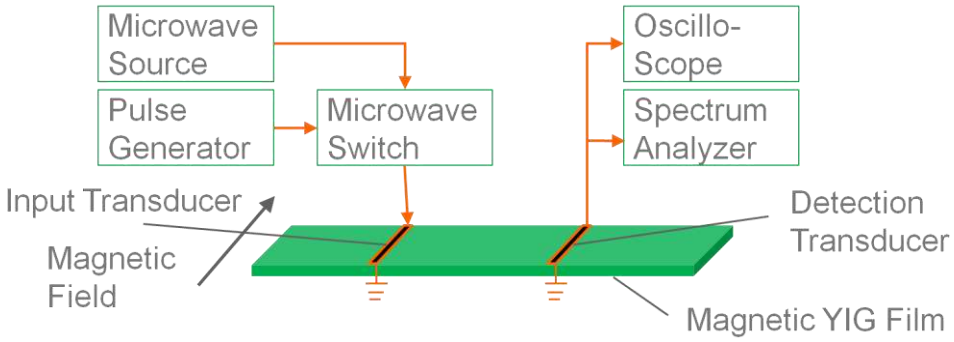

Figure 4. A typical spin wave experiment setup consists of an input transducer and a detection transducer.

Physically, the power loss of a microstrip transducer consists of the intrinsic loss of the antenna and the loss due to spin-wave radiation (Dmitriev and Kalinikos, 1988). The complex resistance of the antenna can be written as,

$$Z = R + iX = (R_0 + R_r) + i(X_0 + X_r) \tag{2.45}$$

where $R_0 + iX_0$ is the primary parameter of the antenna in the absence of radiation and $Z_r = R_r + iX_r$ is the complex resistance due to the spin-wave excitation. The linear radiation resistance is related to the power of radiation by

$$Z_r = I^{-2} P_{rad} \tag{2.46}$$

where I is the current in the antenna. If there is no spin-wave excitation, this term is zero. One can also use the microstrip transducer to detect spin-wave signals in magnetic films. The oscillating magnetic fields produced by spin waves generate an electrical signal in the microstrip antenna, and the intensity of this electric signal is proportional to the spin-wave amplitude. The spin-wave propagation distance is determined by the distance between the excitation and

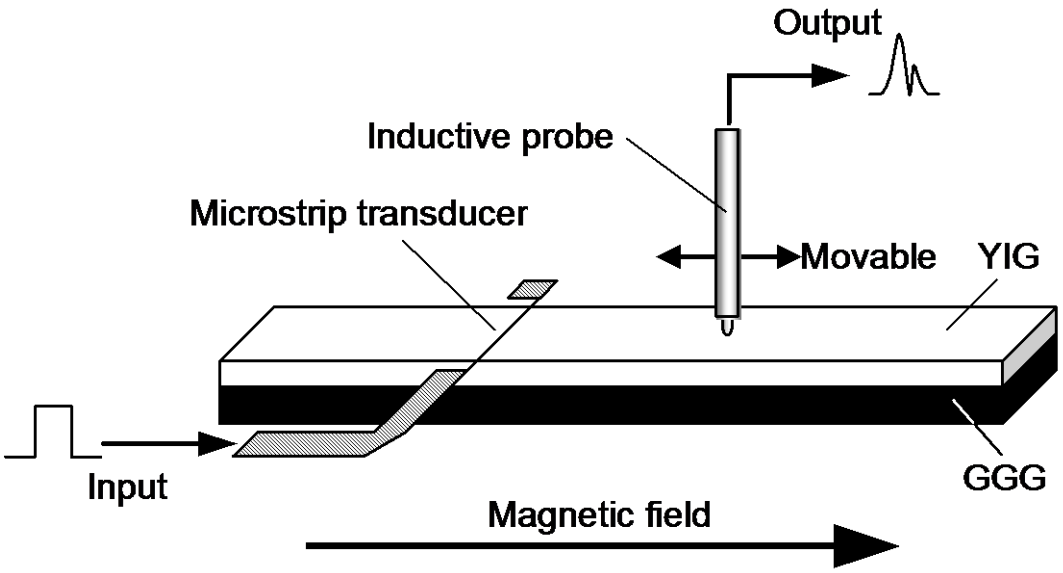

Figure 5. Schematic setup of inductive probe system (Wu, Kraemer, Scott, Patton, and Kalinikos, 2004).

detection transducers. See Figure 4. One can excite a spin-wave pulse by sending a microwave pulse into the excitation transducer. The output signal from the detection transducer is usually sent to a fast oscilloscope for time-domain measurements or a spectrum analyzer for frequency-domain analysis.

One can also detect spin-wave signals in magnetic films with an inductive magneto-dynamic probe (IMP). See Figure 5. Different from the microstrip detection, the IMP detection can be both time- and space-resolved. The probe consists of a small loop attached to the end of a rigid coaxial line and can be scanned above the surface of magnetic films. The IMP system at the CSU Magnetics Laboratory has a spatial resolution of about 50 μm and a temporal resolution of about 1 ns.

2.5 **Ferromagnetic resonance system**

The discussion on the uniform mode in Section 2.1 has not taken into account the damping of magnetization oscillation. To analyze the effects of the damping, one can add a damping term to the magnetic torque equation. One of the widely used equations is the Gilbert equation (Gilbert, 1955),

$$\frac{d\mathbf{M}}{dt} = -|\gamma|\mathbf{M}\times\mathbf{H} + \frac{\alpha}{M_s}\mathbf{M}\times\frac{d\mathbf{M}}{dt} \tag{2.47}$$

where α is the damping constant. If one follows the procedure in Section 2.1 and solve Equation (2.47) for the magnetic susceptibility with the small precession angle assumption, the results can be written as

$$\begin{aligned}
&\chi = \chi' - i\chi'' \\
&\chi' = \frac{1}{4\pi}\frac{\omega_M(\omega_x\omega_y^2 - \omega_y\omega^2 + \alpha^2\omega^2(\omega_x+\omega_y))}{(\omega^2-\omega_x\omega_y)^2+\alpha^2\omega^2(\omega_x+\omega_y)^2} \\
&\chi'' = \frac{1}{4\pi}\frac{\alpha\omega\omega_M(\omega^2+\omega_y^2)}{(\omega^2-\omega_x\omega_y)^2+\alpha^2\omega^2(\omega_x+\omega_y)^2}
\end{aligned} \tag{2.48}$$

where $\omega_x = |\gamma|H_x$ and $\omega_y = |\gamma|H_y$. Here $H_x = H - 4\pi M_s N_z + 4\pi M_s N_x$ and $H_x = H - 4\pi M_s N_z + 4\pi M_s N_y$. Notice that the imaginary part of the susceptibility is responsible for damping (Stancil, 1993).

Ferromagnetic resonance (FMR) measurements are commonly used to determine the damping parameters of a magnetic material. A typical setup is shown in Figure 6. In this type of measurement, the sample is placed either at the end of a shorted waveguide or in a microwave resonance cavity. Note that the sample should be sufficiently small so that the microwave field applied on the sample is spatially uniform. Due to the damping of the magnetic material, the microwave power will be absorbed. The power absorption can be determined by measuring the reflected microwave power. Since the sample is very small, the amount of power that is

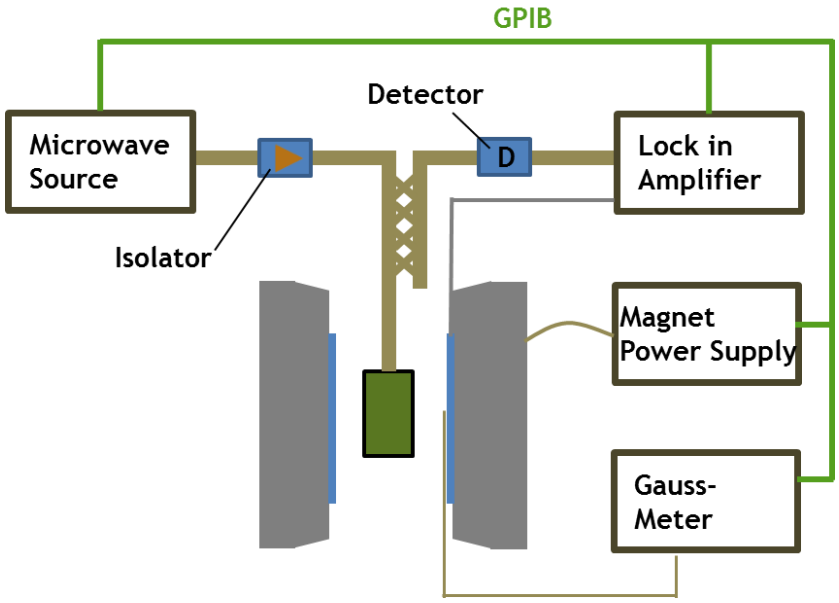

Figure 6. A schematic setup of a ferromagnetic resonance system.

absorbed is also very small. For this reason, it is very difficult (i.e. expensive) to measure the absorbed power directly. The use of a modulation scheme and lock–in amplifier allows for the extraction of very small signals in the presence of large noise with relative ease. The quantity that is to be modulated is the external DC magnetic field. Rather than measuring the absorbed power, we are in fact measuring the slope of the absorbed power with respect to DC magnetic field. During the field sweeping, the microwave power absorbed by the sample exhibits a peak when the FMR condition is satisfied. The width of this absorption peak is associated with the damping constant as discussed below.

From Equation (2.48), one can obtain the field linewidth of the FMR power absorption for a fixed input microwave frequency. Assuming that the $\alpha \ll 1$, which is generally true, then the value of χ'' is maximal at $\sqrt{\omega_x \omega_y} = \omega$ or at

$$H = \frac{1}{2}[-(4\pi M_s N_x + 4\pi M_s N_y) + \sqrt{(4\pi M_s N_x - 4\pi M_s N_y)^2 + 4\left(\frac{\omega}{|\gamma|}\right)^2}] + 4\pi M_s N_z \tag{2.49}$$

The value of χ'' equals to $\frac{1}{2}\chi''_{\max}$ at

$$\begin{aligned} H_+ &= \frac{1}{2}[-(4\pi M_s N_x + 4\pi M_s N_y) + \sqrt{(4\pi M_s N_x - 4\pi M_s N_y)^2 + 4\left(\frac{\omega}{|\gamma|}\right)^2} + \frac{2\partial\omega}{|\gamma|}] + 4\pi M_s N_z \\ H_- &= \frac{1}{2}[-(4\pi M_s N_x + 4\pi M_s N_y) + \sqrt{(4\pi M_s N_x - 4\pi M_s N_y)^2 + 4\left(\frac{\omega}{|\gamma|}\right)^2} - \frac{2\partial\omega}{|\gamma|}] + 4\pi M_s N_z \end{aligned} \tag{2.50}$$

Thus, the FMR half-magnitude frequency linewidth is given by

$$\Delta H_{\text{FMR}} = H_+ - H_- \tag{2.51}$$

As a result, the FMR field linewidth is given by,

$$\Delta H_{\text{FMR}} = \frac{2\alpha}{|\gamma|}\omega \tag{2.52}$$

One can see that, by using Equation (2.52), the damping constant can be evaluated from the FMR field linewidth. It is important to note that the damping term introduced in Equation (2.47) is only a phenomenological term.

CHAPTER 3

ELETCTIC CONTROL OF MANGETIZATION RELAXATION

In this chapter the control of magnetization relaxation in ferromagnetic insulators via interfacial spin scattering is demonstrated. The experiments use nanometer-thick yttrium iron garnet (YIG)/Pt layered structures, with the Pt layer biased by an electric voltage. The bias voltage produces a spin current across the Pt thickness. As this current scatters off the YIG surface, it exerts a torque on the YIG surface spins. This torque can reduce or increase the damping and thereby compress or broaden the ferromagnetic resonance linewidth of the YIG film, depending on the field/current configuration. The linewidth vs. current response shows a threshold effect and nonlinear behavior.

3.1 Introduction to the spin Hall effect

The spin Hall effect was first introduced by Hirsch (Hirsch, 1999) and is in analog with the classical Hall effect. In the classical Hall effect, charge accumulation in the lateral direction across an electrical conductor is produced when the magnetic field is applied perpendicular to the electron moving direction. The spin Hall effect, however, consists of the accumulation of spins on the lateral direction of a current carrying sample in the absence of magnetic fields. If a very strong magnetic field is applied, the spin Hall effect will not take place.

The origin of the spin Hall effect is spin-orbit coupling. Consider, for example, an electron passing through the adjacent area of a non-magnetic ion. According to the Lorentz transformation, the electron will experience an effective magnetic field,

$$\mathbf{B} = -\frac{1}{c}\mathbf{v}\times\mathbf{E} = -\frac{1}{c}\mathbf{v}\times\left(\frac{kq}{r^3}\mathbf{r}\right) \tag{3.1}$$

where **E** is the electric field produced by the ion, **v** is the velocity of electron, and **r** is the position vector of the electron relative to the ion. Assuming that the electron has a magnetic moment **μ**, the spin-orbit coupling energy can be written as,

$$H = -\boldsymbol{\mu}\cdot\mathbf{B} = \frac{\mu_B kq}{cr^3}\left(\mathbf{v}\times\mathbf{r}\right)\cdot\hat{\boldsymbol{\sigma}} \tag{3.2}$$

where the unit vector $\hat{\boldsymbol{\sigma}}$ denotes the direction of the electron's magnetic moment. For the configuration in Figure 7, the effective magnetic field direction is pointing upward and out of plane, with the magnitude larger when closer to the ion. Therefore, for an electron with a magnetic moment pointing up, the trajectory bends to the left to minimize the spin-orbit coupling energy. For an electron with a magnetic moment pointing down, the trajectory bends to the right. It can also be shown that when the ion is on the left side of the electron, the same conclusion will be drawn. The net effect is that a charge current induces a spin current in a direction transverse to the electron's initial velocity, and the latter results in the accumulations of spin-up and spin-down electrons on the opposite edges of the film element. This phenomenon is the so-called spin Hall effect. Inversely, a spin current can also excite an electric current in a direction transverse to itself. This phenomenon is referred to as the inverse spin Hall effect.

Several points need to be made here. First, the diagrams in Figure 7 correspond to a situation where the width of the film element is on the same order of the spin diffusion length λ_{sd} while the thickness of the film element is significantly smaller than λ_{sd}. In the case that the width is significantly larger than λ_{sd} and the thickness is on the same order of λ_{sd}, one has only a spin

current along the thickness direction and spin accumulations on the top and bottom surfaces. Second, strong spin Hall and inverse spin Hall effects only occur in materials with strong spin-orbit interaction due to the origin of the effects.

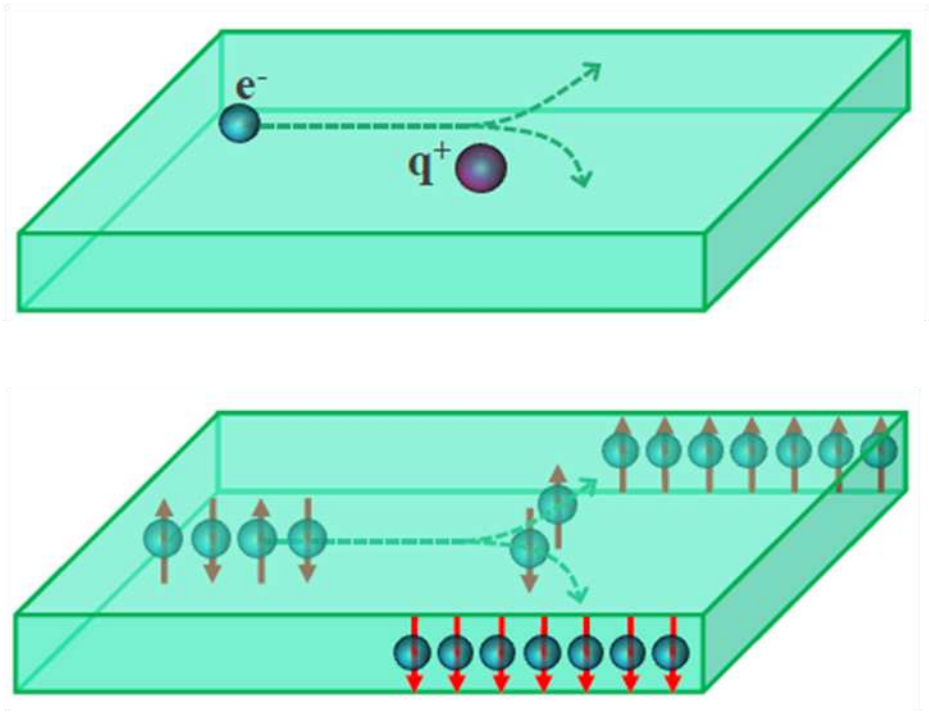

Figure 7. Cartoons for the spin Hall effects in a normal metal film element.

3.2 **Control of magnetization relaxation**

The magnetization in a magnetic material can precess around the direction of a static magnetic field. Such a magnetization precession can be excited by the application of an external radio-frequency (rf) magnetic field. However, once the rf field is removed, the magnetization will relax back to its equilibrium direction. This magnetization relaxation can be due to energy redistribution within the magnetic subsystem, energy transfer out of the magnetic subsystem to non-magnetic subsystems such as phonons and electrons, or energy transfer out of the material to external systems (Heinrich and Bland, 2005; Sparks, 1964).

One can change the rate of the magnetization relaxation of a magnetic material through controlling the material fabrication processes. However, once the material is made, the relaxation rate is generally considered to be unchangeable at certain external field. In contrast, recently two approaches have been demonstrated that can control magnetization relaxations in magnetic thin films: one makes use of the *flow* of spin-polarized electrons through the films, (Fuchs, *et al.*, 2007; Ralph and Stiles, 2008) and the other takes the advantage of the *injection* of spin-polarized electrons into the films (Ando, *et al.*, 2008; Liu, Moriyama, Ralph, and Buhrman, 2011). Although both approaches rely on angular momentum transfer between the polarized conduction electrons and the spins in the films, there exists a substantial difference: the first approach involves the flows of net charge currents through the film materials, while the second does not. The demonstration of such relaxation control is of great significance, both fundamentally and practically. In practical terms, the control of magnetization relaxation is highly desirable because the magnetization relaxation not only plays a critical role in the dynamics of spin-based devices but also sets a natural limit to the response time of a device and determines the magnetization noise.

The two approaches demonstrated so far apply to *metallic* films only. This chapter presents the control of magnetization relaxations in thin film magnetic *insulators.* Specifically, it is demonstrated that one can control ferromagnetic resonance (FMR) linewidth in thin film magnetic insulators *via interfacial spin scattering* (ISS). The experiments use nanometer-thick ferrimagnetic YIG films capped with a nanometer-thick Pt layer. An electric voltage signal is applied to the Pt layer that produces a spin current along the Pt thickness direction via the spin Hall effect (Dyakonov and Perel, 1971; Hirsch, 1999). As the spin current scatters off the surface of the YIG film, it exerts a torque on the YIG surface spins. Due to the exchange interactions,

the effect of this torque is extended to other spins across the YIG thickness and, thereby, changes the FMR response in the whole YIG film.

3.3 **Experimental configurations and parameters**

The net effect of the ISS process on the FMR response depends critically on the relative orientation between (1) the magnetic moments of the electrons in the Pt layer, which move toward the YIG surface, and (2) the precession axis of the magnetic moments in the YIG film. When they are anti-parallel, the FMR linewidth is reduced, which indicates a decrease in the relaxation rate. In contrast, for a parallel configuration, the FMR linewidth is broadened, which indicates an increase in the relaxation rate. Moreover, the FMR linewidth vs. spin current response shows a current threshold and nonlinear behavior. It is important to emphasize that, as the parallel/anti-parallel configuration can be changed simply by reversing the direction of the current or the field, the results demonstrate a simple approach for relaxation control in magnetic insulators.

Figure 8 shows a schematic of the experimental configuration. The YIG film is magnetized by an in-plane static magnetic field H. The Pt film is biased by a *dc* voltage V_a. This voltage signal leads to a current I along $+x$ direction and a flow of electrons along the $-x$ direction, and the latter produces a spin current in the Pt thickness direction via the spin Hall effect. The spins moving towards the YIG film have their magnetic moments in the $-y$ direction, while those moving towards the Pt top surface have their moments in the $+y$ direction. In Figure 8, these directions are indicated by the short arrows in the Pt layer. The YIG/Pt element is placed inside a shorted rectangular waveguide, and the latter produces a microwave magnetic

field *h* which is in the film plane and perpendicular to *H*. For the discussions below, "+*I*" denotes a *dc* current along the +*x* direction; while "-*I*" denotes a *dc* current along the -*x* direction.

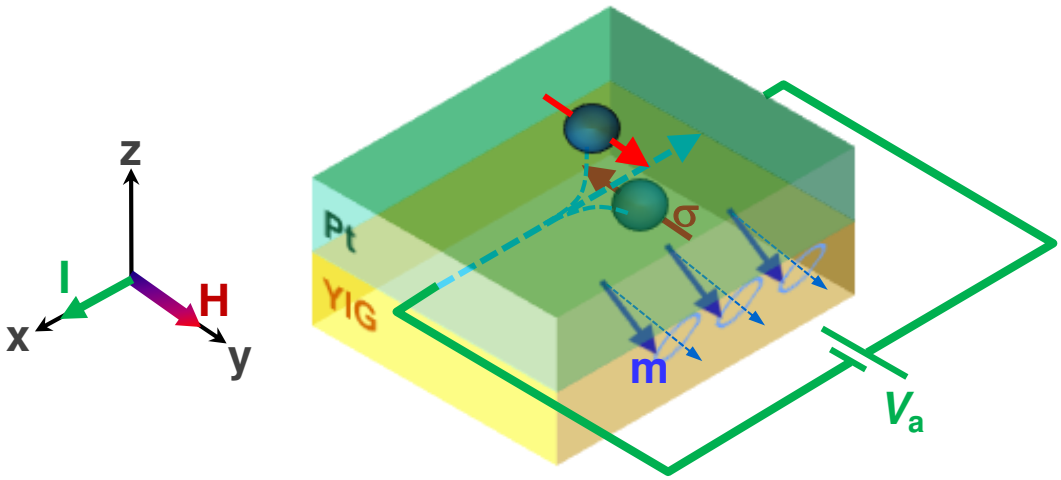

Figure 8. Experimental configuration for control of ferromagnetic resonance through interfacial spin scattering.

The YIG films were deposited with pulsed laser deposition (PLD) techniques. The deposition used a 1 inch-diameter YIG target and a single-crystal (111) gadolinium gallium garnet substrate. The target-to-substrate distance was kept constant at 7 cm. The deposition was done in high-purity (99.999%) oxygen for several minutes. Prior to the deposition, the system had a base pressure of 3.4×10^{-7} Torr. During the deposition, the substrate temperature was kept constant at 790 °C and the oxygen pressure was 0.1 Torr. Right after the deposition, the film sample was annealed at the same temperature in the same oxygen atmoasphere for 10 minutes. The cooling of the films was in a 400 Torr oxygen environment at a rate of 2 °C per minute. The deposition used 248 nm KrF excimer laser pulses with an energy fluence of 1.7 J/cm^2, a pulse duration of 30 ns, and a pulse repetition rate of 2 Hz. These laser parameters together with the target-to-substrate distance yielded a YIG growth rate of about 1 nm per minute. After the deposition, each YIG film was capped by a Pt layer with the PLD technique. The Pt

deposition was done at room temperature with a base pressure of 4.0×10^{-7} Torr and other PLD parameters described above.

For the data presented below, the YIG/Pt element was 4.7 mm long and 3.7 mm wide; and the thicknesses of the YIG and Pt films were 10.0 nm and 5.6 nm, respectively, as determined by X-ray reflectivity measurements. Atomic force microscopy measurements indicated that the YIG film had a surface roughness of about 0.5 nm. Static magnetic measurements yielded a saturation induction of 1858 G. This value is about 6% larger than that for YIG bulk materials. Possible reasons for this difference include the error in film thickness determination and small deviations in chemical composition near YIG film surfaces. All FMR measurements were done by sweeping the field at a fixed microwave frequency of 11.5 GHz. The measurements used field modulation and lock-in detection techniques.

3.4 **Experimental results**

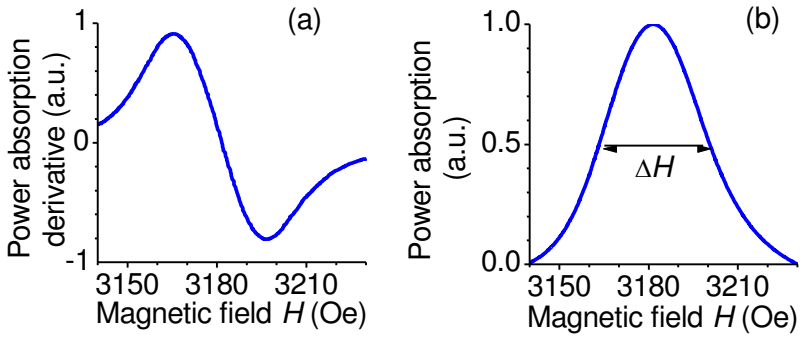

Figure 9. Ferromagnetic resonance profiles: (a) derivative signal and (b) integrated intensity.

Figure 9 shows representative FMR profiles measured in the absence of a *dc* current ($I = 0$). Figure 9(a) shows the power absorption derivative profile. The profile in Figure 9(b) is

obtained through the integration of the profile in Figure 9(a) with the field. The "full linewidth at half maximum" of the profile in Figure 9(b) is the so-called FMR linewidth ΔH. One can see that the ΔH value of the YIG film is much larger than that of YIG single-crystals. Frequency-dependent FMR measurements indicated that this large value is mainly due to inhomogeneity-caused line broadening and two magnon scattering. (Kalarickal, *et al.*, 2008).

In the presence of a *dc* current *I*, the FMR linewidth is

$$\Delta H_I = \Delta H_0 + \Delta H_{heating} + \frac{2\omega}{|\gamma|}\Delta\alpha_I \tag{3.3}$$

where ΔH_0 is the FMR linewidth measured for $I = 0$, $\Delta H_{\text{heating}}$ denotes the change in linewidth due to *dc* current-produced heating, and the last term describes the ISS-produced change in linewidth. In the last term, $|\gamma| = 2.8$ MHz/Oe is the absolute Gyromagnetic ratio; and $\Delta\alpha_{\text{I}}$ denotes the ISS-caused change in Gilbert constant α. Note that the Gilbert constant has been widely used to describe magnetization relaxations (Heinrich and Bland, 2005; Sparks, 1964) and Equation (3.3) has assumed a Gilbert-like damping for the ISS contribution to the relaxation. It is important to emphasize that the value of $\Delta H_{\text{heating}}$ depends on the magnitude of the *dc* current, not the direction of the current; while the value of $\Delta\alpha_{\text{I}}$ depends on both. One can in fact expect $\Delta\alpha_{+\text{I}} = -\Delta\alpha_{-\text{I}}$, as discussed below. For this reason, one can simply use the following equation to describe the ISS-associated damping:

$$\Delta H_I - \Delta H_{-I} = \frac{2\omega}{|\gamma|}(\Delta\alpha_{+I} - \Delta\alpha_{-I}) = \frac{4\omega\Delta\alpha_{+I}}{|\gamma|} \tag{3.4}$$

Figures 10 (a), (b), and (c) show $\Delta H_I - \Delta H_{-I}$ for the field H along the $+y$, $+x$, and $-y$ directions, respectively, with each configuration measured ten times. For all measurements, the magnitude of the *dc* current was 80 mA. One can see in Figure 10 completely different $\Delta H_I - \Delta H_{-I}$ values for different field configurations. All values in Figure 10(a) are negative and indicate a negative $\Delta\alpha_{+I}$ for the $H||(+y)$ configuration. In stark contrast, all values in Figure 10(b) for $H||(+x)$ are small and indicate $\Delta\alpha_{+I}\approx 0$; and all values in Figure 10(c) for $H||(-y)$ are positive and indicate $\Delta\alpha_{+I}>0$.

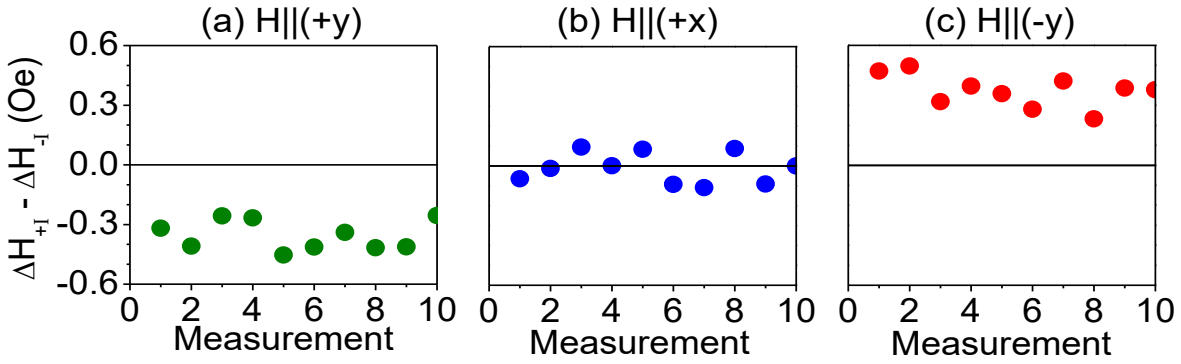

Figure 10. ΔH_{+I}-ΔH_{-I} values measured at different times for different field configurations, as indicated.

These results can be interpreted as follows. When spin-polarized electrons scatter off the YIG surface, they transfer a certain angular momentum to the surface spins in the YIG film (Takahashi, Saitoh, and Maekawa, 2009). This momentum transfer is realized through the s-d exchange interactions at the Pt/YIG interface. Here, "s" refers to spin-polarized electrons in the Pt layer and "d" refers to localized electrons on the surface of the YIG film. The interfacial momentum transfer results in a net torque on the YIG surface spins (Ando, *et al.*, 2008; Liu, Moriyama, Ralph, and Buhrman, 2011):

$$\boldsymbol{\tau} = C\hat{\mathbf{m}}\times\hat{\boldsymbol{\sigma}}\times\hat{\mathbf{m}} \tag{3.5}$$

where $\hat{\mathbf{m}}$ denotes the magnetic moment direction of the YIG surface spins, $\hat{\boldsymbol{\sigma}}$ denotes the magnetic moment direction of the spin-polarized electrons in the Pt film which moves toward the YIG surface, and the coefficient C is associated with the strength of the spin current and the properties of the YIG and Pt layers. For the $H||(+y)$ configuration, the precession of $\hat{\mathbf{m}}$ is around the $+y$ direction and the torque $\boldsymbol{\tau}$ counters the damping of the $\hat{\mathbf{m}}$ precession. The net effect is a decrease in α. For the $H||(-y)$ configuration, in contrast, the precession of $\hat{\mathbf{m}}$ is around the $-y$ direction and the torque $\boldsymbol{\tau}$ leads to an additional damping. One can expect that the changes in α in the two cases have the same magnitude, even though they have opposite signs. This is because the magnitude of $\boldsymbol{\tau}$ is the same for both configurations. Thus, one can expect $\Delta\alpha_{+\mathrm{I}} = -\Delta\alpha_{-\mathrm{I}}$, as mentioned above. In the case of $H||(+x)$, the precession axis is perpendicular to $\hat{\boldsymbol{\sigma}}$, and the average of the torque $\boldsymbol{\tau}$ over each precession period is very small. As a result, the torque produces negligible effects. It is important to emphasize that, although the torque $\boldsymbol{\tau}$ is exerted on the surface spins in the YIG film, its effect is extended to other spins across the YIG film thickness due to exchange interactions. This is possible because the YIG film thickness is smaller than the exchange length. Indeed, a similar behavior has even been demonstrated in YIG films with a thickness of several microns (Kajiwara, et al., 2010).

The $\Delta H_{+\mathrm{I}}$-$\Delta H_{-\mathrm{I}}$ values measured at different *dc* currents are shown in Figure 11(a). Each point shows the averaged value over 5-10 measurements, and the error bar for each point shows the corresponding standard deviation. The right axis shows the corresponding $\Delta\alpha$ values evaluated by Equation (3.4). The top axis shows the corresponding spin current densities obtained by $J_s = \theta_{\mathrm{SH}} J_c$, where $\theta_{\mathrm{SH}} = 0.013$ was the Pt spin Hall angle and J_c was the charge current density. (Mosendz, et al., 2010) Three important results are evident in Figure 11(a).

(1) There is a current threshold for the onset of the ISS effect. (2) Above the threshold, the sign of $\Delta\alpha$ agrees with the expectation discussed above. (3) Above the threshold, the magnitude of $\Delta\alpha$ increases nonlinearly with the spin current, with a negative curvature. Similar ISS effects were observed for other YIG/Pt samples. Figure 11(b) shows data for a YIG/Cu control sample. Each point shows the averaged value over 5 measurements, and the error bar for each point shows the corresponding standard deviation. Note that the thickness of the Cu layer is very close to that of the Pt layer in the YIG/Pt sample. Since the spin Hall effect in Cu is very weak (Niimi, et al., 2011), the sample showed no ISS effects. This indicates that the spin current in the Pt layer is critical for the ISS effects presented.

The Oersted field produced by the dc current in the Pt layer was estimated to be less than 0.2 Oe. This field was significantly smaller than the FMR fields which were about 3200 Oe. Although the Oersted field did cause a slightly shift in the FMR field, it resulted in negligible effects in ΔH since the FMR frequency was kept constant. The observed threshold effects are rather unexpected. One possible origin is the change of spin accumulations in the Pt layer with temperature. At low dc currents, the spin diffusion length, which is about 10 nm (Vila, Kimura, and Otani, 2007), is relatively large in comparison with the Pt thickness and the efficiency in building spin accumulations near the Pt surfaces is relatively small. As the *dc* current is increased to a certain level, the current induced heating leads to a decrease in the spin diffusion length and a corresponding increase in the efficiency of building the spin accumulations (Jedema, Filip, and Wees, 2001).

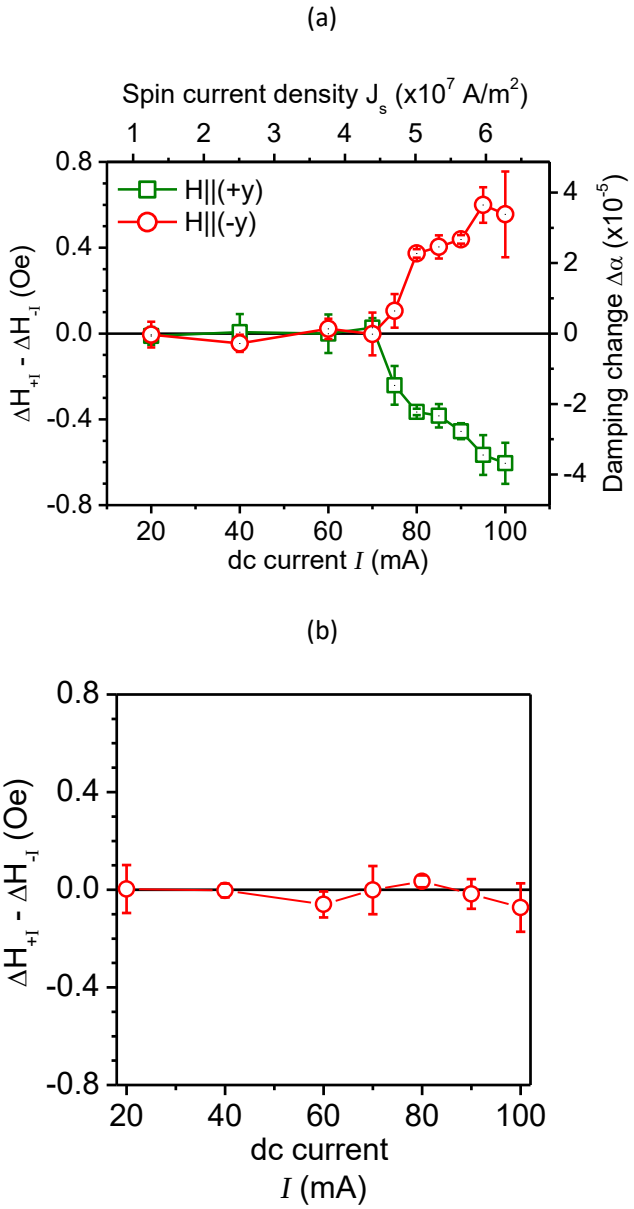

Figure 11. (a) ΔH_{+I}-ΔH_{-I} as a function of *dc* current I and spin current density J_s for the YIG/Pt sample. The right axis shows the corresponding change in damping constant α. (b) ΔH_{+I}-ΔH_{-I} as a function of *dc* current I for a YIG/Cu control sample. The sample is 5.0 mm long and 3.7 mm wide. The YIG film is 6 nm thick and the Cu capping layer is 5 nm thick. The magnetic field is along the +y direction.

In summary, this chapter presented the electric control of magnetization relaxation in YIG thin films via the ISS process. It was found that the ISS effect can play a positive or negative role in the relaxation; and one can control this role by simply changing the strength and direction

of the *dc* current. It was also found that the damping constant vs. spin current response showed a current threshold and nonlinear behavior. Future work that is of great interest includes the study of the roles of YIG and Pt thicknesses on the ISS effects and the demonstration of the ISS effects in other materials. Future study on the origins and features of the observed threshold and nonlinear effects is also of great interest.

CHAPTER 4

CONTROL OF SPIN-WAVE AMPLITUDE IN FERRIMAGNETIC INSULATORS

This chapter describes the control of spin waves in a ferrite thin film via interfacial spin scattering. The experiments used a 4.6 μm-thick YIG film strip with a 20-nm thick Pt capping layer. A dc current pulse was applied to the Pt layer and produced a spin current across the Pt thickness. As the spin current scatters off the YIG surface, it can either amplify or attenuate spin-wave pulses that travel in the YIG strip, depending on the current/field configuration. The spin scattering also affects the saturation behavior of high-power spin waves.

4.1 Spin wave damping and parametric pumping

Spin waves in ferromagnetic films have many unique properties and thereby have potential for applications in microwave signal processing (Kabos and Stalmachov, 1994; Stancil and Prabhakar, 2009; Adam, *et al.*, 2002), logic operations (Bance, *et al.*, 2008; Schneider, *et al.*, 2008; Khitun, Bao, and Wang, 2010), and insulator-based electrical signal transmissions (Kajiwara, *et al.*, 2010; Gurevich and Melkov, 1996). These applications, however, are bottlenecked by the damping of spin waves. Such damping can result from various physical processes, such as spin-orbit coupling, scattering on defects, and three- and four-wave nonlinear interactions.

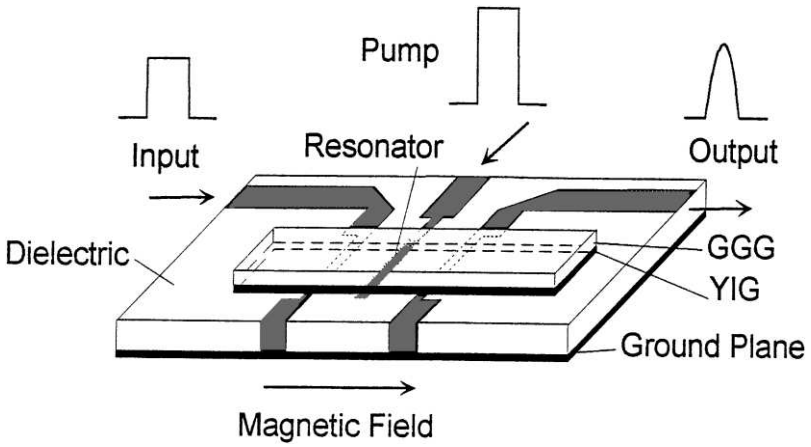

Figure 12. Experimental setup of parametric pumping of spin wave (Kolodin, *et al.*, 1998).

One way to compensate the spin-wave damping is to use *parametric pumping* (Gurevich and Melkov, 1996). Previous experiments have demonstrated that the spin waves in magnetic thin films could be parametrically amplified (Kolodin, *et al.*, 1998; Bagada, Melkov, Serga, and Slavin, 1997). Figure 12 shows a schematic experiment setup for the parametric pumping of spin waves. The spin wave travelling in the YIG film loses energy during propagation. In this setup, the energy lost is compensated by an external microwave source through three-wave parametric pumping. This method, however, requires the use of (1) an external microwave signal with a frequency twice that of the spin wave and (2) a delicate microwave resonator structure for the delivery of this signal to the magnetic film. Moreover, the amplification is limited to a very narrow frequency range, which is determined by the frequency conditions of the parametric resonance.

4.2 **Amplification of spin waves through interfacial spin scattering**

The work described in Chapter 3 demonstrates the control of FMR linewidth through the interfacial spin scattering (ISS) effect. This chapter presents the results on the amplification of

spin waves. Experiments use a 4.6 μm-thick yttrium iron garnet (YIG) film strip with a 20-nm thick platinum (Pt) capping layer. A dc current pulse is applied to the Pt film and produces a spin current along the Pt thickness direction via the spin-Hall effect (Dyakonov and Perel, 1971; Hirsch, 1999; Day, 2005). As the spin current scatters off the surface of the YIG film, it exerts a torque on the YIG surface spins. Due to the dipolar and exchange interactions, the effect of this torque is extended to other spins across the YIG thickness and thereby to spin-wave pulses that travel in the YIG film.

The net effect of the ISS process on spin waves depends critically on the relative orientation of (1) the magnetic moments of the electrons in the Pt layer which scatter off the YIG surface and (2) the precession axis of the magnetic moments on the YIG surface. When they are anti-parallel, the spin-wave damping is reduced and the amplitude of a traveling spin-wave pulse is increased. In contrast, in a parallel configuration, the spin-wave pulse experiences an enhanced attenuation. The ISS process can also raise or reduce the power level to which high-power spin-wave pulses saturate due to nonlinear damping (Gurevich and Melkov, 1996; Scott, Patton, Kostylev, and Kalinikos, 2004).

It is important to emphasize that, as the parallel/anti-parallel configuration can be changed simply by reversing the direction of the dc current, this work demonstrates a rather simple new approach for the control of spin waves. One can expect that in the future this ISS effect would allow for the realization of decay-free spin-wave propagation and the development of a new class of electronic devices (Kabos and Stalmachov, 1994; Stancil and Prabhakar, 2009; Adam, Davis, Dionne, Schloemann, and Stitzer, 2002; Bance, *et al.*, 2008; Schneider, *et al.*, 2008; Khitun, Bao, and Wang, 2010).

4.3 **Experimental configuration and parameters**

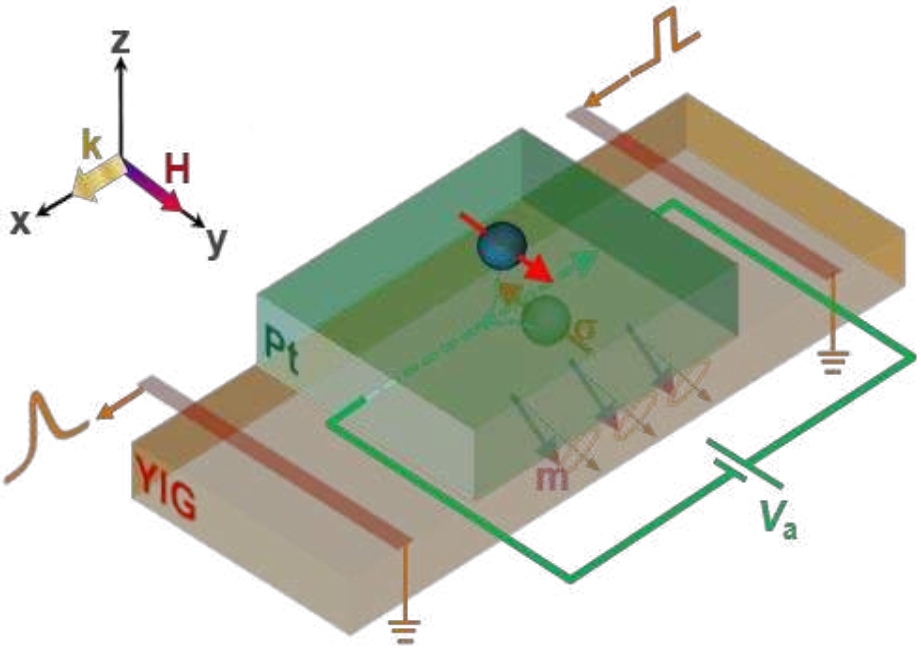

Figure 13. Experimental setup for control of spin waves through interfacial spin scattering in a YIG/Pt structure.

Figure 13 shows a schematic of the experimental configuration. The core component is a long and narrow YIG film strip with its central portion covered by a Pt thin film. The YIG film is magnetized by an in-plane magnetic field H. The field is referred as a "positive field" (H>0) when it is applied along the $+y$ direction and a "negative field" (H<0) when it is in the $-y$ direction. This film/field configuration supports the propagation of *surface* spin waves, of which the amplitude has an exponential distribution along the YIG film thickness. When H>0, the spin wave with a wave vector **k** along the $+x$ direction has a larger amplitude near the top surface of the YIG film. When H<0, the spin wave along the $+x$ direction has a larger amplitude near the bottom surface of the YIG film. Two microstrip transducers are placed on

the right and left ends of the YIG strip for the excitation and detection, respectively, of the spin wave.

A dc voltage V_a is applied to the Pt film. A positive voltage (V_a>0) results in a current flow along the +*x* direction and a flow of electrons along the -*x* direction. The electrical current produces a spin current along the Pt thickness direction via the spin Hall effect. When V_a>0, the electrons moving towards the YIG film have their magnetic moments in the –*y* direction. In Figure 8, the small spheres in the Pt layer represent electrons, and the arrows through the spheres indicate the directions ($\hat{\sigma}$) of the electron magnetic moments.

For the data presented below, the YIG strip was 4.6 μm thick, 2.2 mm wide, and 22 mm long. It was cut from a larger single-crystal (111) YIG film grown on a gadolinium gallium garnet substrate by liquid phase epitaxy. The Pt film was grown on the YIG strip at room temperature by pulsed laser deposition (PLD). Based on the PLD parameters, the thickness of the Pt film was estimated to be about 20 nm. This value matches the estimation based on the resistance of the Pt element, which was 20.1 nm. For this estimation, a resistivity of ρ=371 nΩ·m was used for the Pt film. The Pt element had the same width as the YIG strip and a length of L=3.5 mm. The microstrip transducers were 50 μm wide and 2.0 mm long. The transducer separation was held at 5.5 mm, with each transducer 1.0 mm away from the Pt element.

The signals applied to the excitation transducer were microwave pulses with a width of 50 ns and a repetition period of 10 ms. These signals excited spin-wave pulses in the YIG strip. The signals applied to the Pt element were dc pulses with a width of 300 ns and the same period as the microwave pulses. The microwave pulses had a delay of 20 ns relative to the dc pulses.

These parameters ensure that the spin current was on over the entire propagation time of each spin-wave pulse.

4.4 **Experimental results and discussions**

Figure 14 presents the data measured for H=683 Oe. Graph (a) shows the transmission profile for the transducer-YIG-transducer structure. The dashed line indicates a frequency of 3.636 GHz, which was the carrier frequency of the input microwave pulses for most of the measurements. Graph (b) shows output signals measured for three different dc pulse voltages (V_a) applied to the Pt layer. The time t=0 corresponds to the moment when a microwave pulse enters the excitation transducer. Graph (c) gives the relative change in the peak voltage of the output signal as a function of V_a. Here, the relative change is defined as $(V\text{-}V_0)/V_0$, where V_0 is the peak voltage of the output signal for V_a=0 and V is the peak voltage of the output signal for $V_a \neq 0$. For the data in both (b) and (c), the power of the input microwave pulses was set to 0.68 W. Graph (d) shows the peak power of the output pulse as a function of the peak power of the input microwave pulse for three V_a values.

The data in Figure 14 show three important results. The application of a positive voltage to the Pt element leads to an enhancement in the amplitude of the output signal and an increase in the power level to which the output pulse saturates. This indicates that, when $V_a>0$, the ISS effect leads to the amplification of the spin wave and plays a role of negative damping. (2) In contrast, the application of a negative voltage to the Pt element leads to a decrease in both the amplitude and saturation power level of the output pulse. This indicates that, when $V_a<0$, the ISS effect results in an attenuation in the spin-wave amplitude and plays a role of additional damping. (3) Over the highest available V_a range, the output signal amplitude vs. V_a response

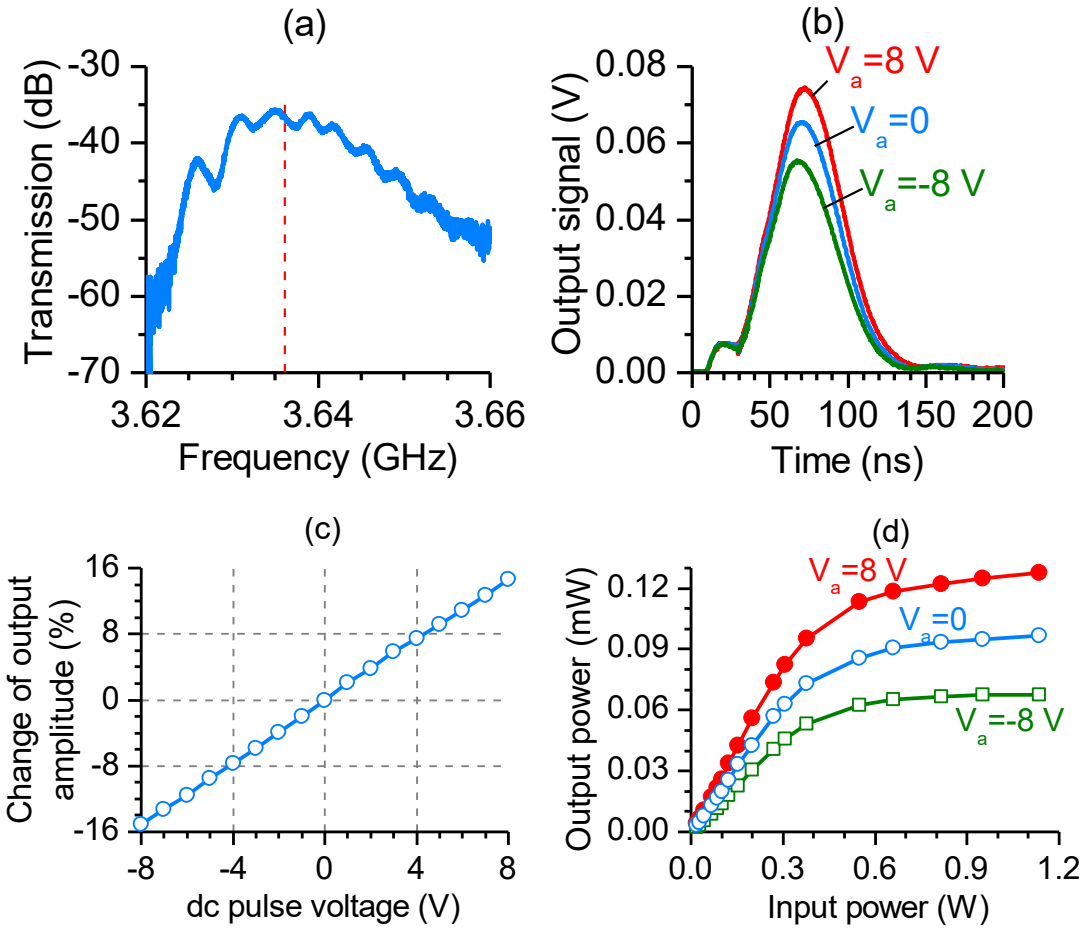

Figure 14. Control of spin waves through interfacial spin scattering. (a) Transmission profile for the transducer-YIG-transducer structure. (b) Time-domain output signals for different dc pulse voltages (V_a) applied to the Pt layer. (c) Relative change in output signal amplitude as a function of V_a. (d) Output power vs. input power responses for three V_a values, as indicated.

shows almost perfect linear behavior. Besides, the data in (b) also indicates that a "short" pulse travels slightly faster than a "tall" pulse. This can be explained by the nonlinearity-associated dependence of the spin-wave group velocity (v_g) on amplitude (Slavin and Zaspel, 2002).

These results can be interpreted as follows. When spin-polarized electrons scatter off the YIG surface, they transfer a certain net angular momentum to the surface spins in the YIG film. This momentum transfer is realized through the *s*-*d* exchange interactions at the Pt/YIG interface. Here, *s* refers to spin-polarized conduction electrons in the Pt layer, while *d* refers to

localized electrons on the YIG surface. A theoretical model of this interfacial process has been suggested recently (Takahashi, Saitoh, and Maekawa, 2009).

The interfacial momentum transfer results in a net torque on the surface magnetic moments in the YIG film (Ando, *et al.*, 2008; Liu and Vignale, 2011):

$$\boldsymbol{\tau} = C\frac{\gamma J_s}{M_s T}\hat{\mathbf{m}}\times\hat{\boldsymbol{\sigma}}\times\hat{\mathbf{m}} \tag{4.1}$$

where $\hat{\mathbf{m}}$ is a unit vector along the magnetic moment direction of the YIG surface spins, γ is the absolute value of the Gyromagnetic ratio, M_s is the saturation magnetization of the YIG film, T is the effective thickness of the YIG surface layer where the spins are involved in the momentum transfer, and C is a phenomenological coefficient which describes the properties of the Pt/YIG interface such as the spin mixing conductance. J_s is the density of the spin current in the Pt layer, which can be written as

$$J_s = \theta_{SH} J_c = \theta_{SH}\frac{|V_a|}{\rho L} \tag{4.2}$$

where θ_{SH} and J_c are the spin Hall angle of and the charge current in the Pt element, respectively. The torque $\boldsymbol{\tau}$ is exerted on the surface magnetic moments in the YIG film, but its effect is extended to other moments across the YIG thickness via dipolar and exchange interactions.

One can write the moment vector $\hat{\mathbf{m}}$ as $\mathbf{m}_0+\mathbf{m}(t)$, where $\mathbf{m}_0$ is along the precession axis and is typically considered being static and $\mathbf{m}(t)$ is perpendicular to the precession axis and is dynamical. The magnitude of $\mathbf{m}(t)$ defines the spin-wave amplitude. If one takes the small-signal approximation, namely, $|\mathbf{m}(t)|<<|\mathbf{m}_0|$, one can rewrite Equation (4.1) as

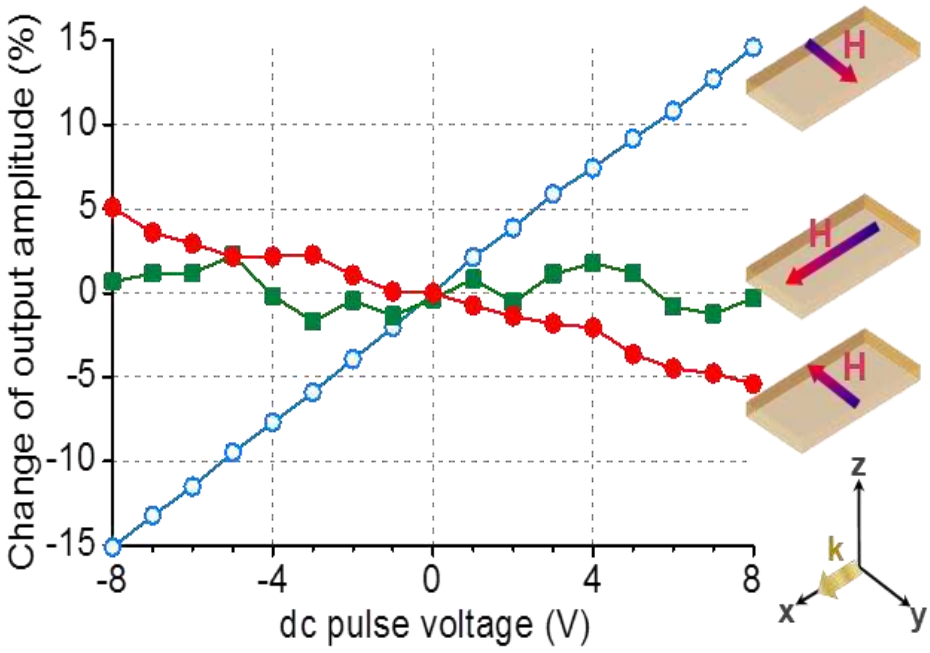

Figure 15. Relative change in output pulse amplitude as a function of dc pulse voltage applied to the Pt film for three different field orientations, as indicated.

$$\boldsymbol{\tau} = \mathrm{sgn}(-\mathbf{m}_0 \cdot \hat{\boldsymbol{\sigma}}) C \frac{\gamma J_s}{M_s T} \mathbf{m}(t) \tag{4.3}$$

With this equation, one can qualitatively understand the results shown in Figure 14, as discussed below.

First, when $V_a>0$, the vector $\hat{\boldsymbol{\sigma}}$ is along the $-y$ direction, as shown in Figure 13, and the torque $\boldsymbol{\tau}$ is parallel to the moment $\mathbf{m}(t)$ and tends to open up the precession cone. As a result, the spin-wave pulse is amplified and its saturation power level is raised up. Second, when $V_a<0$, $\hat{\boldsymbol{\sigma}}$ is along the $+y$ direction and $\boldsymbol{\tau}$ is anti-parallel to $\mathbf{m}(t)$. The net effect is that the spin-wave pulse is attenuated and saturates to a lower power level. Third, Equations (2) and (3) also indicate that $|\boldsymbol{\tau}|$ increases with $|V_a|$. This explains the behavior shown in Figure 14(c).

The above interpretation was supported by measurements performed with the direction of $\hat{\boldsymbol{\sigma}}$ fixed and the direction of $\mathbf{m}_0$ varied. The representative data are given in Figure 15. The Figure shows $(V\text{-}V_0)/V_0$ as a function of V_a. The open circles show the same data as in Figure 14(c), which were measured for H=683 Oe. The solid circles show the data for H=-683 Oe. This "negative field" supports the propagation of spin waves with a wave vector $\mathbf{k}$ near the bottom surface of the YIG film (Kabos and Stalmachov, 1994; Stancil and Prabhakar, 2009). The squares show the data for a field of 1074 Oe in the $+x$ direction. This field orientation supports the propagation of backward volume spin waves (Kabos and Stalmachov, 1994; Stancil and Prabhakar, 2009). For the volume wave measurements, the frequency of the input microwave pulse was 5.036 GHz. All other parameters were the same as cited above.

Three results are evident in Figure 15. (1) A reversal of the field orientation from the $+y$ direction to the $-y$ direction leads to opposite behavior, and this is true for both $V_a>0$ and $V_a<0$. This observation agrees with the expectation of Equation (4.3), namely, that a flip of $\mathbf{m}_0$ results in a switching between the $\boldsymbol{\tau}\|\mathbf{m}$ and $\boldsymbol{\tau}\|(-\mathbf{m})$ configurations and a corresponding switching between the "positive damping" and "negative damping" roles of $\boldsymbol{\tau}$. (2) For a field applied along the length of the YIG strip, the effects of V_a on V are insignificant. This agrees with the prediction of Equation (4.1), namely, that the net effect of $\boldsymbol{\tau}$ is zero over each precession period when $\mathbf{m}_0$ and $\hat{\boldsymbol{\sigma}}$ are normal to each other. (3) The ISS effects on the spin waves with larger amplitude near the bottom surface are weaker than those on the waves with larger amplitude near on the top surface. This may indicate that the efficiency of transfer of the ISS effects on the surface spins to other spins decreases with film thickness.

Turn now to the evaluation of the ISS-produced changes in the decay rate η and damping constant α of the spin waves. One can use the following equation to model the propagation of a spin-wave pulse $u(x, t)$ along an YIG strip

$$i\frac{\partial u}{\partial t} = [\omega_0 + v_g(-i\frac{\partial}{\partial x} - k_0)]u - i\eta u + i\Delta\eta u \tag{4.4}$$

where ω_0 and k_0 are the spin-wave carrier frequency and wavenumber, respectively. $\Delta\eta$ describes the ISS-produced change in η. It is clear from the above discussion that the sign of $\Delta\eta$ depends on sgn($\mathbf{m}_0\cdot\hat{\boldsymbol{\sigma}}$); and the magnitude of $\Delta\eta$ increases with $|\boldsymbol{\tau}|$ (and thereby with $|V_a|$). To perform the quantitative calculation of $\Delta\eta$, one needs to know the spin mixing conductance at the YIG/Pt interface and consider the specific spin-wave configuration. For a qualitative discussion below, one introduces a phenomenological expression

$$\Delta\eta = \mathrm{sgn}(\mathbf{m}_0\cdot\hat{\boldsymbol{\sigma}})\lambda\frac{\theta_{SH}|V_a|}{\rho L} \tag{4.5}$$

where the coefficient λ describes the efficiency of the change of η due to the ISS process. One can use Equation (4.4) to determine the spatial variation of the peak amplitude of the pulse $u(x, t)$. Assuming A_0 and A are the peak amplitudes of $u(x, t)$ at $x=L$ for $V_a=0$ and $V_a\neq 0$, respectively, one then obtains

$$\frac{A-A_0}{A_0} = e^{\Delta\eta L/v_g} - 1 \tag{4.6}$$

This ratio equals to $(V\text{-}V_0)/V_0$. Thus, one can use the data in Figure 15 and Equation (6) to estimate$\Delta\eta$.

Figure 16 gives the ISS-produced changes in η and α for the experimental configurations which are the same as for the data shown in Figure 14 (b) and (c). The left and right axes show $\Delta\eta$ and $\Delta\alpha$, respectively, as a function of J_s. The estimation of $\Delta\alpha$ was based on the assumption that η was close to the decay rate of a uniform mode. The estimation used $2\Delta\eta=\Delta\alpha\gamma(2H+4\pi M_s)$ (Craik, 1975), with γ=2.8 MHz/Oe and $4\pi M_s$=1750 G (Liu, Moriyama, Ralph, and Buhrman, 2011). The J_s values were obtained with Equation (4.2) and θ_{SH}=0.076. The data in Figure 16 clearly show that one can control, either enhance or mitigate, the decay of a spin wave through the ISS process. Fitting the $\Delta\eta$ values with Equation (4.5) yields $\lambda=1.03\times10^{-2}$ m^2·Hz/A for the $H\|(+y)$ case and $\lambda=0.33\times10^{-2}$ m^2·Hz/A for the $H\|(-y)$ case.

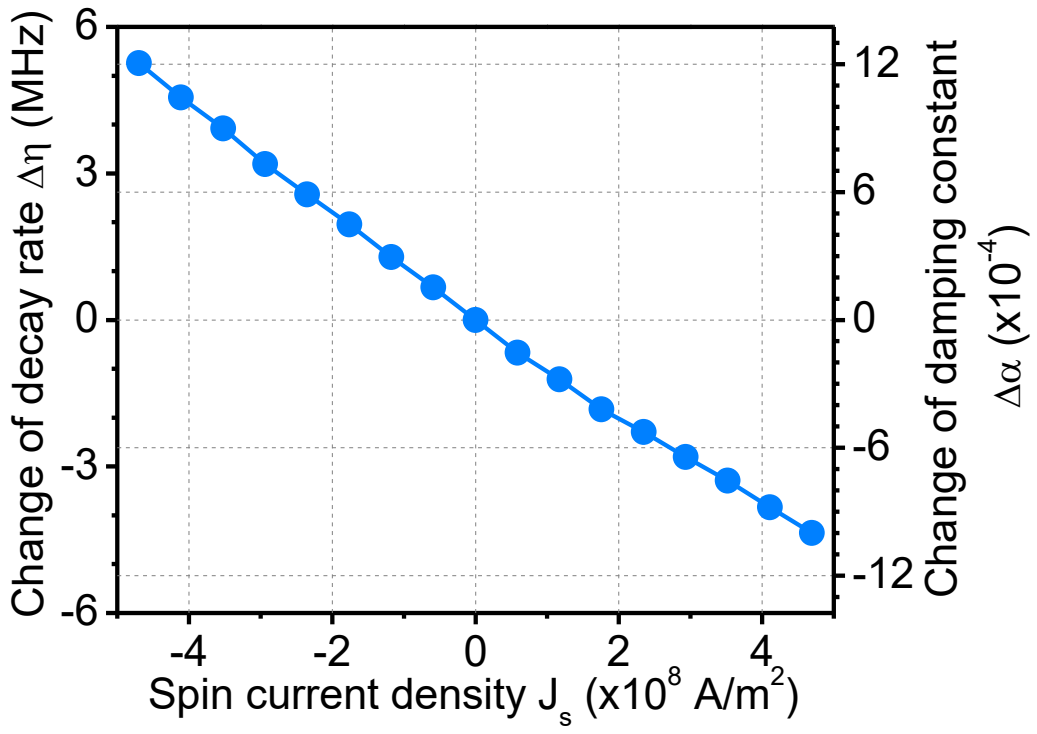

Figure 16. Change in spin-wave decay rate and damping constant as a function of spin current density in the Pt layer.

In addition to the spin current, the electric current in the Pt layer also produces ohmic heating and Oersted fields, but both have negligible influences on spin waves for the configurations in the present work. Figure 17 shows representative data. Graph (a) gives $(V\text{-}V_0)/V_0$ as a function of V_a. The circles give the same data as in Figure 14(c), for which the dc pulse width was 300 ns. The crosses give the data measured with a dc pulse width of 900 ns. One sees an almost perfect agreement between the two sets of data. This indicates that the heating effect is very weak. Graph (b) gives the relative change of the output amplitude as a function of a small shift in H. The data were measured for V_a=0. Other parameters are the same as cited above. A ±1 Oe field shift range was considered because the estimated value of the current-produced field was less than 1 Oe. The data in (b) show that the field-induced amplitude change is less than 2%. This small change probably results from the shift of the spin-wave dispersion curve with the field (Kabos and Stalmachov, 1994; Stancil and Prabhakar, 2009). The dispersion shift can give rise to a shift of the transmission profile (see Figure 14(a)) along the frequency axis and a corresponding change in transmission loss for a specific spin wave.

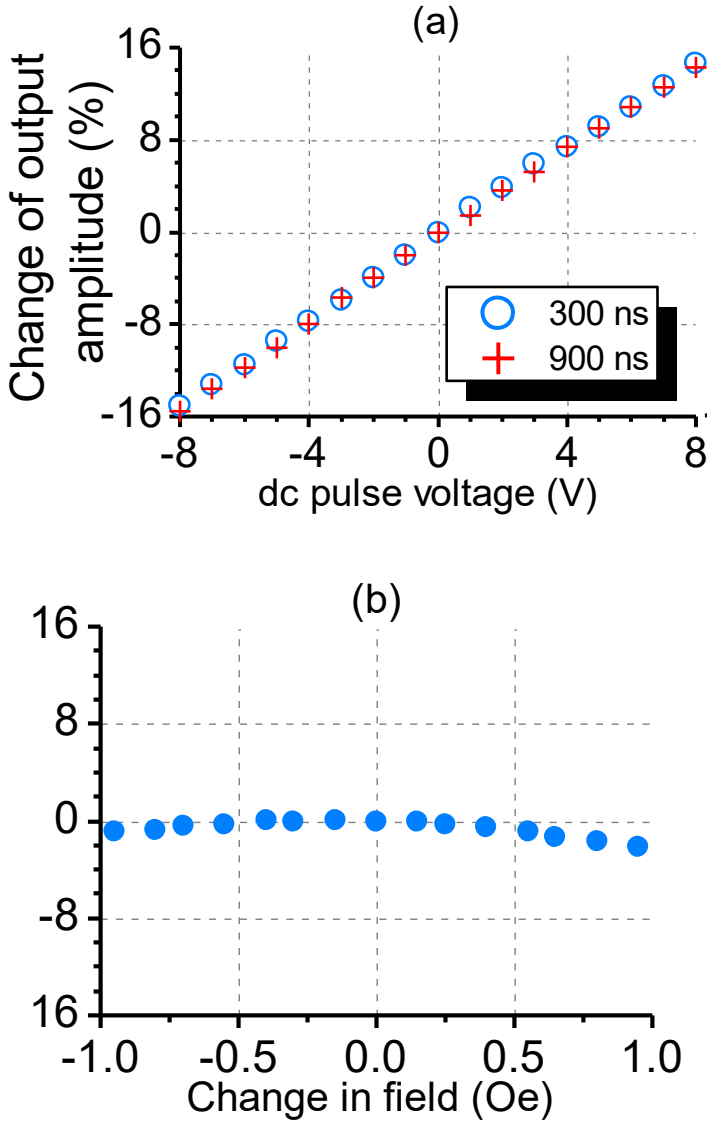

Figure 17. (a) Relative change in output pulse amplitude as a function of dc pulse voltage for two dc pulse durations. (b) Relative change in output pulse amplitude as a function of a shift in magnetic field.

4.5 **Control of spin waves with large input currents**

In the last section, an amplification of a spin wave up to 16% is demonstrated with the help of a spin current generated in the Pt layer by the spin Hall effect. However, there are still several open questions remaining to be answered. First of all, is it possible to realize a larger

amplification beyond 16% by applying larger electrical currents to the Pt layer? Second, Equations (4.5) and (4.6) implies that the amplification should increase exponentially as the applied voltage across the Pt layer is increased. Will this be the case? Third, is there any frequency or wavenumber dependences for the amplification response?

In order to answer these questions, a dc pulse generator with the maximum output voltage of 150 V is used to apply dc voltages across the Pt layer. Special attention need to be paid in the case where large bias voltages are applied. First, due to large input voltages, the ohimic heating effect may be very significant. In order to minimize the heating effect, short dc voltage pulses with low repletion rates were used. More discussions on this concern are given in the end of this section. Second, the magnetic fields generated by large currents may shift the spin-wave transmission band significantly. To take into account the magnetic field effect and at the same time avoid any heating in the sample, the spin-wave amplitude frequency characteristic (AFC) in the presence of a dc voltage on the Pt layer was measured in the pulse region. Here the signal to the transducer is a microwave pulse with a duration of 1 μs, and the signal applied on the Pt film is a dc voltage pulse which has the same duration as and is synchronized with the microwave pulse. The spin-wave pulse signal is detected by the output transducer and monitored with a fast oscilloscope. The frequency of the input microwave pulse is swept over a certain range in order to map the spin-wave AFC. The transmission coefficient is measured as a function of the input microwave frequency. Here the transmission coefficient is defined as,

$$S_{21} = 20 \log \frac{V_{\text{out}}}{V_{\text{in}}} \tag{4.6}$$

where V_{in} and V_{out} are the voltage amplitudes of the input and output microwave pulses, respectively. Figure 18 shows the measurement configurations.

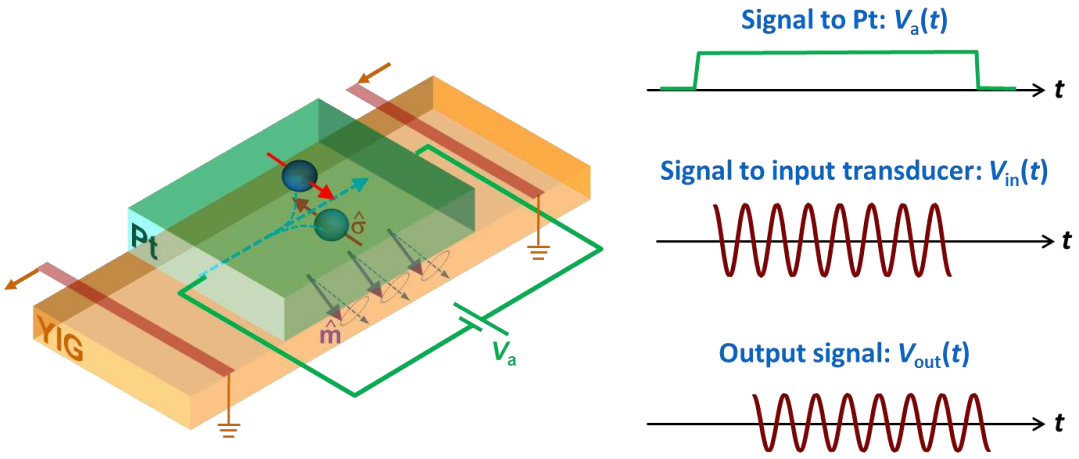

Figure 18. Schematic of spin-wave amplitude frequency characteristic (AFC) measurement configurations.

For the data presented below, the YIG film strip had a length of 16 mm, a width of 1.6 mm, and a thickness of about 5 μm. The Pt layer was grown on the top of the YIG film by the PLD technique and was 18 nm thick. The resistance between the two ends of the Pt strip was 112 Ohm. The separation between the input and output transducers was about 9 mm. The input microwave pulse power was kept constant at 15 dBm. This input power level was chosen to insure that the output signals were sufficiently strong for detection, while at the same time the nonlinear damping was not involved.

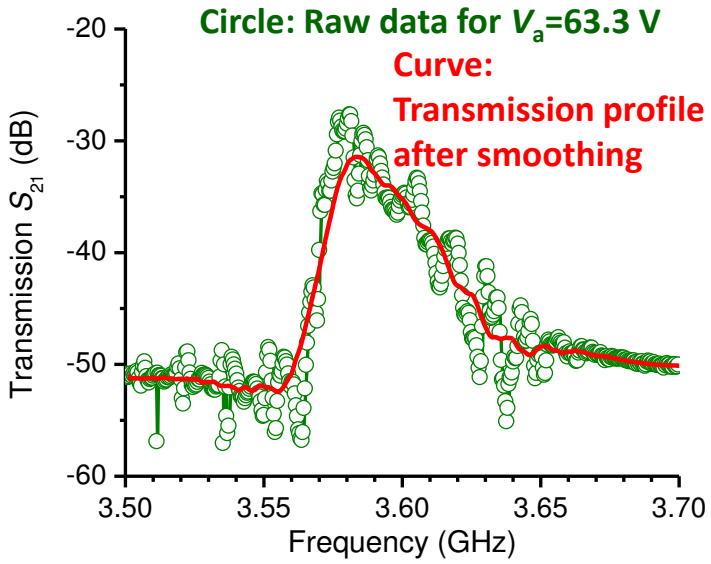

Figure 19. Transmission profile for the structure shown in Figure 18. The circles show the raw data for a dc pulse voltage of 63.3 V applied to the Pt layer. The red curve shows a transmission profile after smoothing the raw data.

Figure 19 gives a representative transmission profile measured with the method described above. The circles in the Figure show the raw data which were taken with a dc voltage pulse of 63.3 V applied to the Pt layer. The frequency is swept with a step of 1 MHz and a range of 200 MHz. As can be seen from the Figure, the noise level of the raw data is relatively high. In order to obtain useful information for further analysis, a smoothing of the raw data is carried out sequentially in each 20 MHz span. The transmission result after the smoothing is shown as the red curve in the Figure.

Figure 20 shows the transmission profiles (after smoothing) obtained with three different dc pulse voltages applied across the Pt layer. Here the red curve shows the transmission profile obtained for a positive applied voltage of 63.3V, the blue curve shows the transmission profile in the absence of dc pulses, and the green curve shows the profile for a negative applied voltage.

For all the curves shown in the Figure, the data were taken with the same input microwave power and the same external magnetic field.

Several important points can be made about the data shown in Figure 20. First, it can be seen that, with positive dc pulses applied, the transmission profile has higher amplitude compared to the one obtained in the absence of dc pulses. This "higher amplitude" indicates that the application of the dc pulses gives rise to the amplification of the spin-wave signal and a corresponding increase in the output signal amplitude. On the other hand, with negative dc pulses applied, the transmission profile has lower amplitude compared to the one measured in the absence of dc pulses. This "lower amplitude" behavior indicates a decrease in the output signal amplitude or the attenuation of the spin-wave signal in the presence of negative dc pulses. Second, the transmission band is shifted to low frequencies in the presence of positive dc pulses and is shifted to high frequencies in the presence of negative dc pulses. This shifting of the transmission band is a direct result of the dc pulse-produced magnetic field. Finally, it is worth to mention that, although not shown here, the transmission profile measured in the absence of dc pulses matches very well with the transmission response of the structure measured by a vector network analyzer.

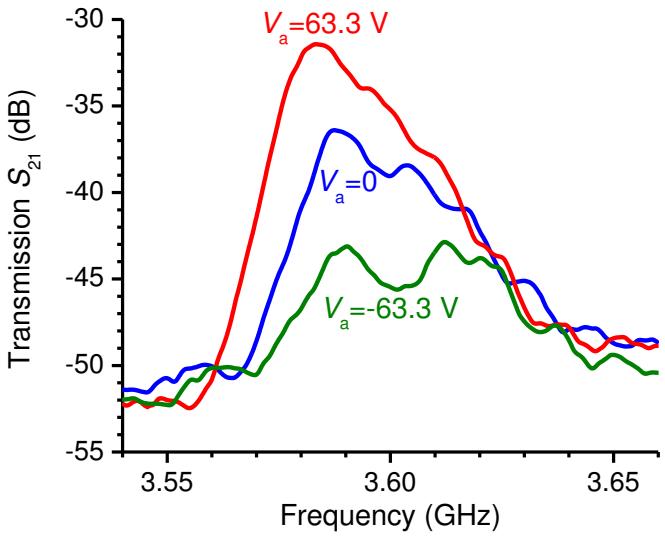

Figure 20. Transmission profiles (after smoothing) obtained for three different voltages applied to the Pt layer.

In order to quantitatively evaluate the amplification as a function of frequency or wavenumber, the magnetic field-caused frequency shift of the transmission band needs to be corrected. The corrections were carried out with three steps as follows. (1) The magnitude of the magnetic field produced by the electric current in the Pt layer was estimated. (2) The corresponding change in the spin-wave frequency was calculated by using the dispersion relation of magneto-static surface waves (see Equation (2.19)). (3) The obtained frequency change was then used to correct the frequencies of the measured transmission profile.

Figure 21 gives the data that show the above-described corrections. Graph (a) shows a series of transmission profiles measured for different input dc pulse voltage levels. Here the voltage is increased from 0 V to 132.4 V with a step of about 30 V. It is evident that, with an increase in the pulse voltage, the transmission band not only show a higher amplitude, but also shifts to the left. As discussed above, the "higher amplitude" is due to the ISS-produced

spin-wave amplification, while the "left-shift" results from the electric current-produced magnetic field. Graph (b) shows the transmission profiles after the corrections. One can see that, after the corrections, all the transmission profiles are located in the same frequency range. Also, the weak dips in the different profiles occur at the same frequencies. These dips may result from the partial pinning of the spins on the YIG film surface.

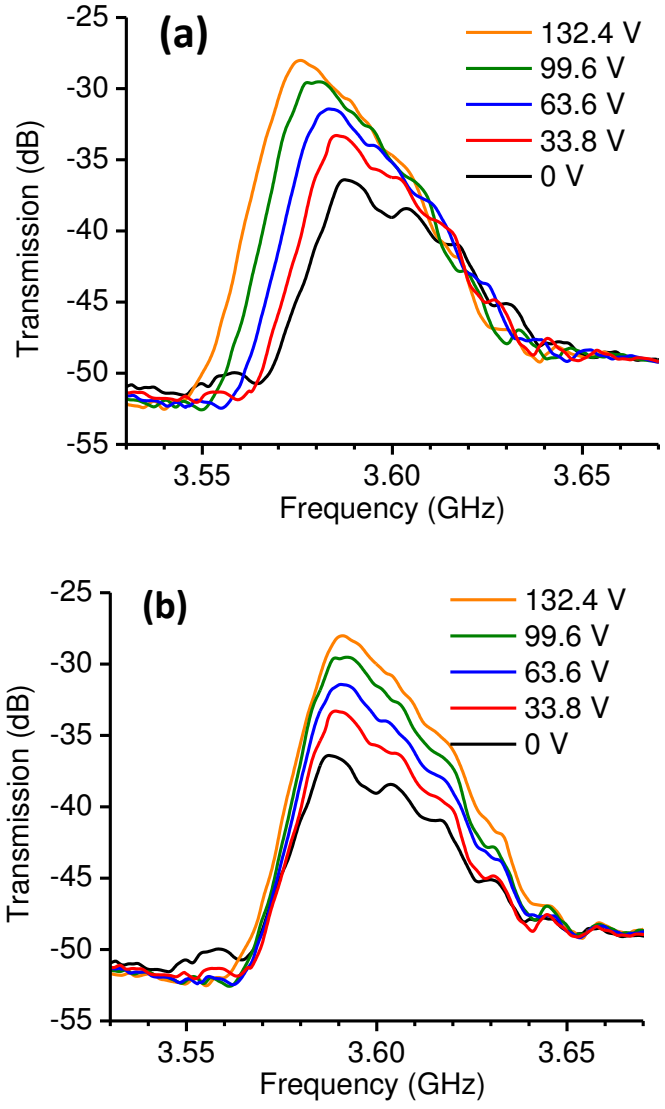

Figure 21. (a) Transmission profiles measured with a series of gradually increased dc pulse voltages. (b) Transmission profiles with the magnetic field-caused frequency shifting corrected.

The amplification as a function of frequency can now be determined by subtracting the corrected transmission data for a certain applied voltage from the transmission data obtained in the absence of dc pulses. Figure 22 shows representative data on the amplification vs. frequency response. The Figure shows four responses obtained for different dc pulse voltages, as indicated. Figure 23 shows the amplification as a function of the dc pulse voltage for two different frequencies, as indicated.

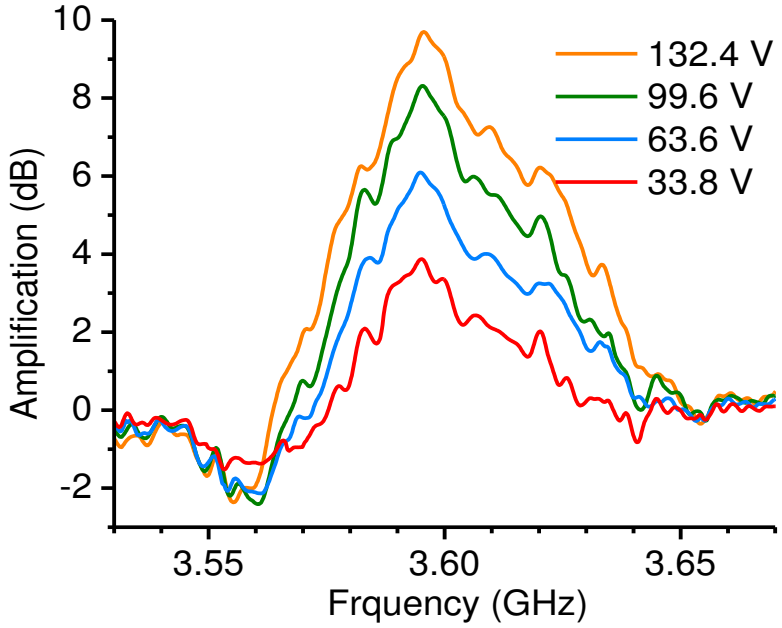

Figure 22. Amplification as a function of frequency obtained for four different dc pulse voltages.

Three important results can be seen from the data in Figs. 22 and 23. First, significant amplifications were observed for large dc pulse voltages. At an applied voltage of 130 V, for example, the maximal amplification is about 10 dB, which corresponds to a 200% increase in spin-wave amplitude. Second, the amplification as a function of the applied voltage shows nearly linear behavior. This linear behavior is unexpected since Equations (4.5) and (4.6) indicate an exponential increase in amplification with the applied voltage. Third, the

amplification is indeed frequency- or wavenumber-dependent. Although the physical mechanisms for this dependence is not clear, additional experiments indicate that the dependence is not a nonlinear effect, is not associated with the group velocity property, and does not result from the ohm heating effect, as discussed below.

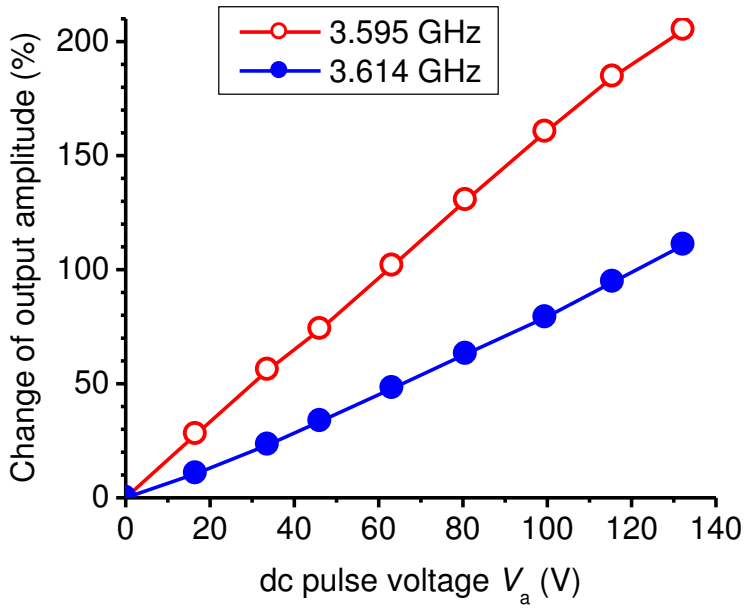

Figure 23. The change of output amplitude as a function of DC pulse voltage.

Figure 24 shows the transmission profiles measured with three different input microwave power levels, as indicated. The upper graph shows the data taken for a dc pulse voltage of 46.2 V, and the lower graph shows the data for a dc pulse voltage of 99.6V. For both graphs, the change in the transmission profile with the input microwave power is insignificant. This indicates that there are no nonlinear effects in the experiments with an input power of 15 dBm or lower. The small changes at the edges of the transmission band is most likely due to the fact that the instrument sensitivity is low for weak transmissions at low input microwave power

levels. Note that the data in Figs. 22 and 23 were obtained with an input power level of 5 dBm. Thus, one can see that the above-described frequency dependence is not a nonlinear effect.

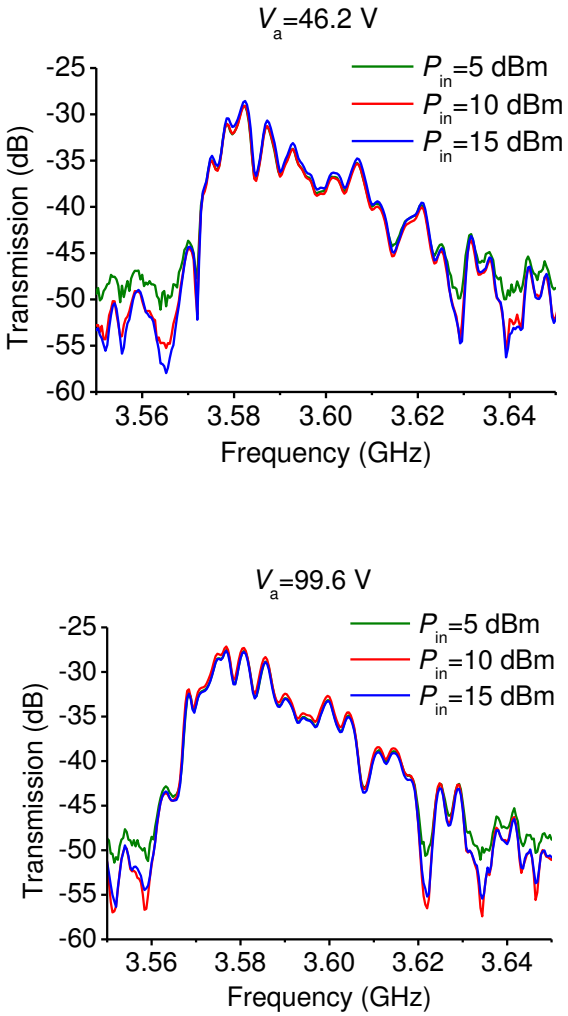

Figure 24. Transmission profiles measured with different input microwave power levels, as indicated. The upper and lower graphs give the data obtained for different dc pulse voltages, as indicated.

Figure 25 shows the relative phase change as a function of the input microwave frequency measured for the same structure in the absence of dc pulses. The slope of this phase-frequency response is inversely proportional to the group velocity of the spin wave in the YIG film. It can be seen from the data in Figure 25 that the phase-frequency response shows nearly linear

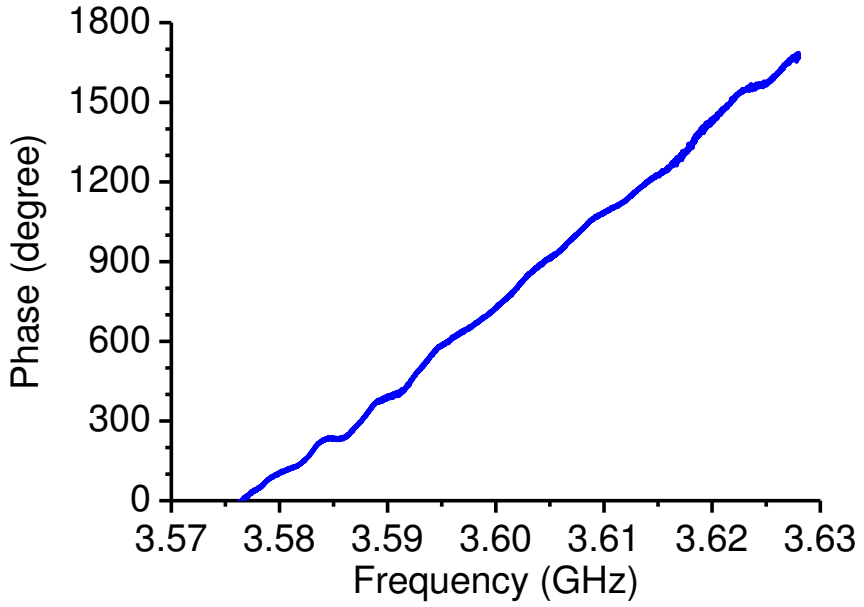

Figure 25. Change of spin-wave phase as a function of frequency for the structure shown in Figure 18. No dc pulses were applied to the Pt layer.

behavior. This behavior indicates that the group velocity is almost constant in the frequency range where the experiments were conducted. Therefore, the above-described frequency-dependent amplification is not due to the variation of the spin-wave group velocity with the frequency.

The heating effect was examined by measuring the transmission responses at two different input microwave durations. If there exists a heating effect, the frequency of the transmission band should shift as one varies the microwave pulse duration. This expectation results from two facts: (1) The longer the microwave pulse is, the stronger the heating effect; and (2) the heating can lead to a decrease in the saturation magnetization, and the latter gives rise to a decrease in the spin-wave frequency. Figure 26 shows representative data on the effects of microwave pulse duration. It is evident that there is almost no change in the transmission

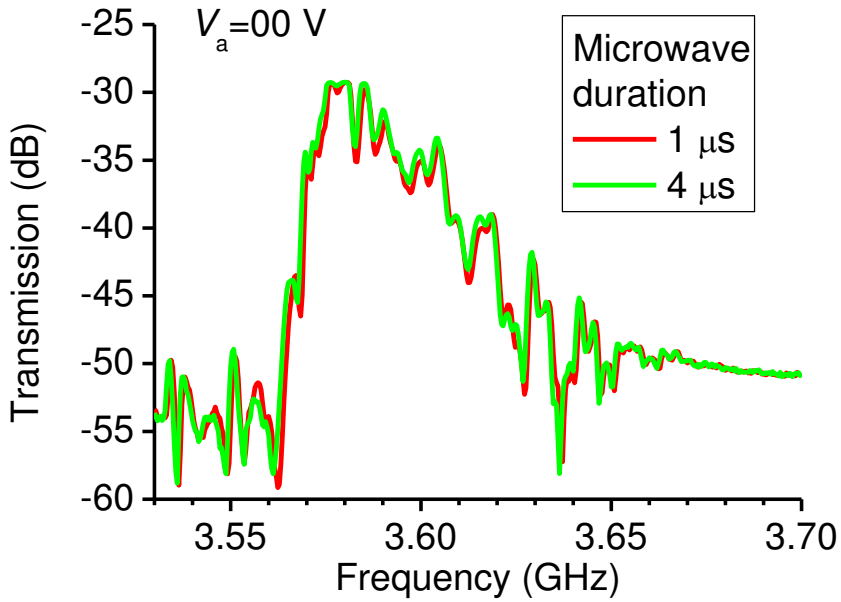

Figure 26. Transmission profiles measured at two different input microwave pulse durations, as indicated.

profile when the input microwave duration is changed from 1μs to 4μs. This indicates that the frequency dependence presented above is not a heating effect.

In summary, the control of spin waves propagating in ferrimagnetic insulator films through the ISS effect was demonstrated for the first time. The experiment utilized a YIG thin film strip with an ultrathin Pt capping layer. It was found that one can control the amplitude and saturation behavior of a spin-wave pulse simply through the application of a dc pulse to the Pt layer. Future work that is of great interest includes the realization of decay-free spin-wave propagation via the ISS effect, the development of an appropriate theoretical model for the above-presented effects, and the demonstration of control of propagating spin waves in metallic films via interfacial spin penetration.

CHAPTER 5

CHAOTIC SPIN-WAVE SOLITONS IN MAGNETIC FILM FEEDBACK RINGS

The work described in Chapters 3 and 4 was mainly on linear spin waves. In contrast, this chapter and the following two chapters concerns nonlinear spin waves. In this chapter, the first observation of chaotic bright solitons in magnetic film active feedback rings is reported. At some ring gain level, one observes the self-generation of spin-wave bright soliton pulses in the ring. When the pulse circulates in the ring, its amplitude varies chaotically with time. Numerical simulations based on a gain-loss nonlinear Schrödinger equation reproduce the observed chaotic responses. Chapters 6 and 7 present results on dark solitons in magnetic film strips.

5.1 **Introduction to chaotic spin-wave solitons**

If one amplifies the output signal from a dissipative transmission line and then feeds it back to the input of the line, one creates an active feedback ring system – a driven damped system. In the steady state of this system, the energy loss of the wave in the dissipative line is compensated by the energy gain provided by the amplifier. Examples of this type of ring system include fiber ring lasers (Luo, Tee, and Chu, 1998; Zhao, Tang, and Liu, 2006; Soto-Crespo and Akhmediev, 2004), magnetic film feedback rings (Wu, Kalinikos, and Patton, 2005; Wu, Kalinikos, Carr, and Patton, 2006; Demidov and Kovshikov, 1998; Demokritov, *et al.*, 2003), and electromagnetic transmission line oscillators (Ham, Li, and Ricketts, 2006; Ricketts, Li, nad Ham, 2006). These systems are excellent test beds for studies of nonlinear dynamics and, therefore, have attracted considerable research interest. The two main focus areas are (1) *envelope solitons* and (2) *chaos*. For (1), the main work has been on the demonstration of

envelope solitons in a wide variety of ring configurations (Zhao, Tang, and Liu, 2006; Wu, Kalinikos, Carr, and Patton, 2006; Ricketts, Li, and Ham, 2006; Soto-Crespo and Akhmediev, 2004; Demokritov, *et al.*, 2003). For (2), the main focus has been on the use of various configurations to demonstrate chaotic excitations through different nonlinear processes (Luo, Tee, and Chu, 1998; Soto-Crespo and Akhmediev, 2004; Zhao, Tang, and Liu, 2006; Demidov and Kovshikov, 1998; Wu, Kalinikos, and Patton, 2005; Ricketts, Li, and Ham, 2006; Ham, Li, and Ricketts, 2006) and the development of new models to describe chaotic excitations in certain ring systems (Luo, Tee, and Chu, 1998; Zhao, Tang, and Liu, 2006; Soto-Crespo and Akhmediev, 2004).

Recent theoretical work showed that the active feedback system could also support *chaotic solitons.* Specifically, Soto-Crespo *et al*. (Soto-Crespo and Akhmediev, 2005), Zhao *et al*. (Zhao, Tang, and Liu, 2006), and Karar *et al.* (Karar, Smy, and Steele, 2008) reported optical envelope solitons that circulated in fiber feedback rings and had their amplitudes varying with time in a chaotic manner. This discovery opened a completely new paradigm in the field of nonlinear science. This is because solitons and chaos are usually considered to exist in opposite physical regimes and present two totally unconnected aspects of nonlinear dynamics (Ablowitz and Segur, Solitons and the Inverse Scattering Transform, 1985; Kivshar and Agrawal, 2003; Addison, 1997). In spite of the significance of this result, however, the experimental demonstration of such chaotic solitons has been rather limited. The only demonstration so far was done by Zhao *et al*. for optical soliton pulses in fiber feedback rings (Zhao, Tang, and Liu, 2006); however, neither the solitonic nature of the pulses nor the chaotic nature of their behavior was confirmed.

This chapter reports on the first experimental demonstration and modeling of chaotic spin-wave solitons in magnetic film active feedback rings. As the ring gain is increased to a certain threshold level, one observes the self-generation of spin-wave envelope solitons that circulates in the ring with constant amplitude. With a further increase in the ring gain, this soliton pulse develops into a chaotic soliton - a soliton whose amplitude changes chaotically with time. The pulse has a hyperbolic secant shape and a flat phase profile across its width, which are the signatures of a soliton. The overall time-domain signal resulting from the circulation of the pulse shows a finite correlation dimension and a positive Lyapunov exponent, both of which are signature of chaos. Numerical simulations, based on a gain-loss nonlinear Schrödinger equation (GLNLS), reproduced the observed responses. At relatively low ring gain levels, there is even a quantitative agreement between the numerical and experimental results.

It is important to emphasize that, although these results were obtained for a magnetic film feedback ring, the work has implications for other driven damped nonlinear systems, including optical fiber rings (Luo, Tee, and Chu, 1998; Soto-Crespo and Akhmediev, 2004; Zhao, Tang, and Liu, 2006) and electromagnetic transmission line oscillators (Ricketts, Li, and Ham, 2006; Ham, Li, and Ricketts, 2006). It is also important to highlight that this work demonstrates a new type of chaotic microwave pulse generator. Chaotic microwave sources are critically needed by chaotic radar (Liu, Zhu, Hu, and Jiang, 2007; Dimitriev, Kyarginskii, Panas, Puzikov, and Starkov, 2003) and chaotic communications.

5.2 **Magnetic film active feedback rings**

Figure 27 shows a schematic diagram of a magnetic film feedback ring. The ring consists of a YIG thin film strip and two microstrip transducers placed over the YIG strip to excite and

detect spin waves (Dimitriev, Kyarginskii, Panas, Puzikov, and Starkov, 2003). The output signal from the detection transducer was fed back to the excitation transducer through a microwave amplifier and an adjustable microwave attenuator. The YIG strip was magnetized by a static magnetic field applied parallel to the YIG strip length. This film-field configuration supports the propagation of backward volume spin waves along the YIG strip and, at the same time, prohibits three-wave processes (Chen, Tsankov, Nash, and Patton, 1994; Stancil, 1993). The ring signal was sampled through a directional coupler, with feeds to a spectrum analyzer for frequency analysis and an oscilloscope for temporal signal measurements. For the data presented below, the YIG strip was 5.6 μm thick, 2.1 mm wide, and 52 mm long. The magnetic field was 938 Oe. The microstrip transducers were 50 μm wide and 2 mm long elements. The transducer separation was held at 5.5 mm. The microwave amplifier had a peak output power of 2 W and a linear response over the frequency range of 1-8 GHz.

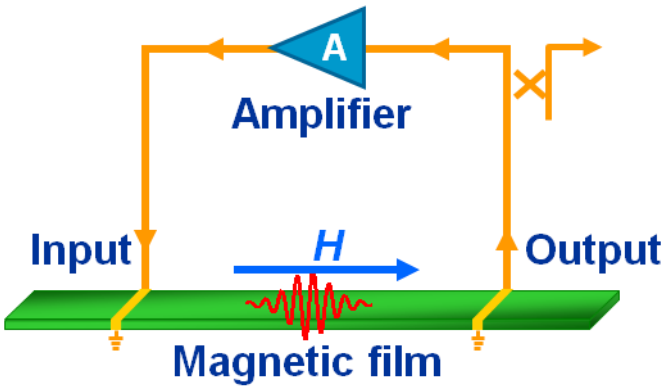

Figure 27. Schematic of a magnetic film strip-based active feedback ring.

The feedback ring can have a number of resonance eigenmodes that exhibit low decay rates (Wu, Kalinikos, Carr, and Patton, 2006). The frequencies of these modes can be determined by the phase condition $k(\omega)l+\phi_e=2\pi n$, where k is the spin-wave wavenumber, ω is the frequency, l is

the transducer separation, ϕ_e is the phase shift introduced by the electronic circuits, and n is an integer. At a low ring gain G, all eigenmodes experience an overall net loss, and there is no spontaneous signal in the ring. If the ring gain is increased to a certain level, here taken as $G = 0$, the eigenmode with the lowest decay rate will start to self-generate in the ring. As a result, in the time domain one will obtain a continuous wave response. A further increase in G leads to the excitation of additional modes and a comb-like frequency spectrum, which, in the time domain, corresponds to a spin-wave soliton that circulates in the ring; and then to the broadening of each mode in the frequency spectrum, which, in the time domain, corresponds to the realization of chaotic solitons as reported below. Here, both the excitation of new modes and the mode broadening are realized through four-wave interactions. At even higher gain levels, one obtains the circulation of two or more spin-wave pulses in the ring. Note that the first demonstration of solitons in magnetic film feedback rings was carried out by Kalinikos *et al*. (Kalinikos, Kovshikov, and Patton, 1997). That demonstration also used the backward volume spin-wave configuration, but the solitons were excited by the use of external microwave pulses and appropriate interruption to the ring.

5.3 **Experimental observation of chaotic solitons**

Figure 28 shows representative power spectra for ring signals obtained at different ring gains. In each panel, the bottom diagram shows the full spectrum, and the top diagrams present ×32 expanded views for the three main peaks in the bottom diagram. All diagrams have the same vertical power scale. The three top diagrams for the same main peak also have the same frequency scale. The peak widths in all the diagrams are instrument limited.

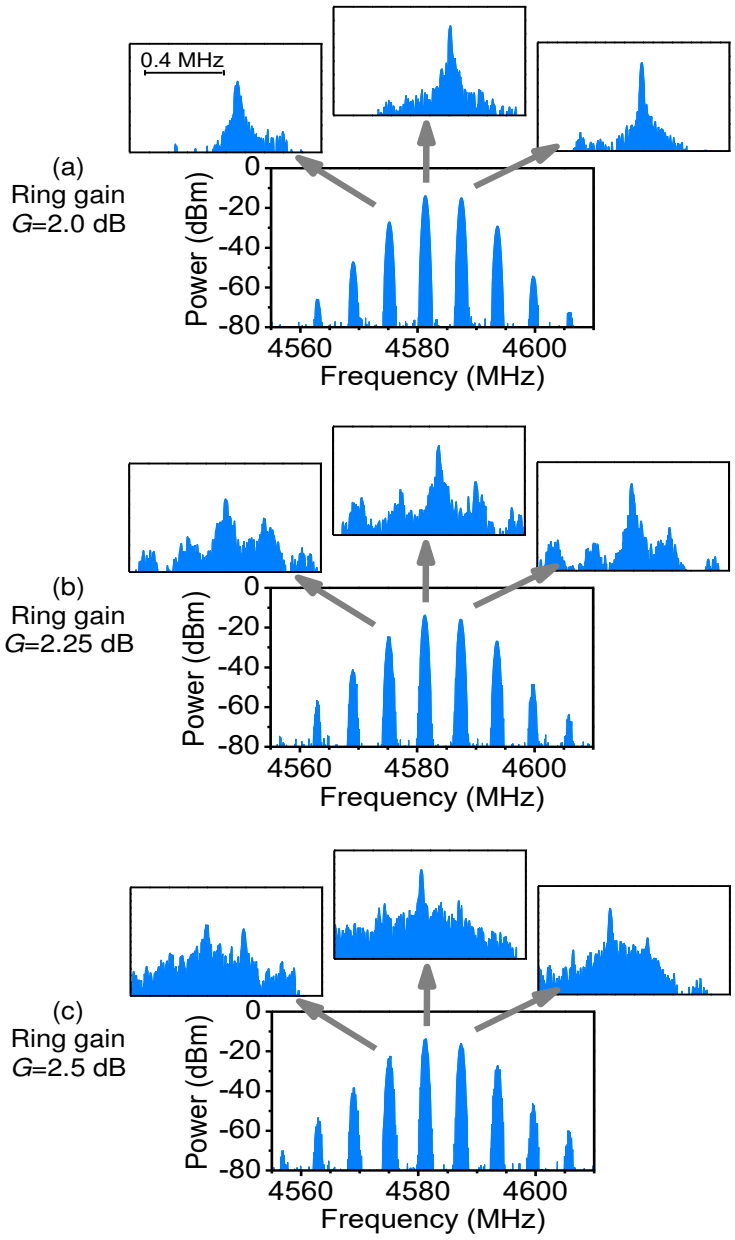

Figure 28. Spectra for ring signals obtained at different ring gain levels, as indicated.

The data in Figure 28 demonstrate three results. (1) On a large frequency scale, as shown in all the bottom diagrams, the power spectrum has a comb-like structure. With an increase in *G*, this comb spectrum remains the same, except that there is a weak growth in mode intensity.

(2) On a smaller frequency scale, each mode consists of a narrow single peak for G=2.0 dB. With an increase in G, one observes the excitation of new sideband peaks near the initial single peak, as shown in the top diagrams in (b), and then the wash out of those modes and the realization of broad spectra, as shown in the top diagrams in (c). (3) There is a slight shift of the modes to lower frequencies. This shift agrees with the fact that backward volume spin waves have a negative nonlinearity coefficient. (Chen, Tsankov, Nash, and Patton, 1994)

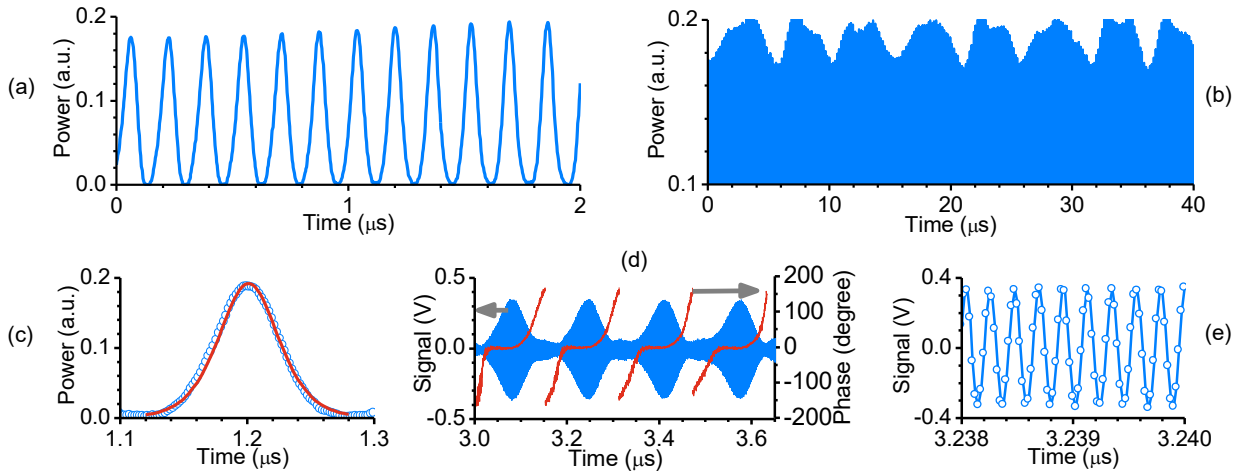

Figure 29. Time-domain signal obtained at G=2.5 dB: (a)-(c) power profiles; (d)-(e) carrier waves. In (c), the circles show the actual data and the curve shows a hyperbolic secant function fit. The curves in (d) show the relative phase profiles of the corresponding pulses.

The time-domain signal obtained at G=2.0 dB consists of a uniform train of pulses. This signal corresponds to the clean comb spectrum in Figure 28(a) and results from the continuous circulation of a single spin-wave soliton in the ring (Wu, Kalinikos, Carr, and Patton, 2006). With an increase in G to 2.25 dB, the train becomes chaotic – the amplitude of the pulse varies chaotically with time. This corresponds to the excitation of new side modes shown in Figure 28(b) and is the onset of chaos. With a further increase in G, one observes stronger chaotic behavior.

Figure 29 shows the time-domain signal obtained at G=2.5 dB. Graphs (a) and (b) show the power profile of the signal in different time and power scales. Graph (c) shows one pulse in (a) in an expanded time scale. The circles are data, and the curve is a fit to a hyperbolic secant squared function. Graph (d) shows the carrier waves (left axis) and phase profiles (right axis) for four pulses. Each phase profile shows the phase of the carrier wave relative to a reference continuous wave whose frequency was given by the main frequency of the carrier wave of the pulse. Graph (e) shows the carrier wave of one pulse in (d) in an expanded time scale.

The data in Figure 29(a)-(b) show a train of chaotic pulses. This train corresponds to the circulation of a single spin-wave soliton pulse whose amplitude changes chaotically with time. The data in (c) shows a perfect hyperbolic secant function fit. The data in (d) show flat phase profiles across the central portions of the pulses. These results clearly confirm the solitonic nature of the pulses. The waveform in (e) and the clean phase profiles in (d) show that, in spite of the chaotic variation in amplitude, the soliton has a coherent carrier wave as a conventional soliton.

Figure 30 shows representative data that confirm the chaotic nature of the time-domain signals. Graph (a) shows a 3D attractor. Graph (b) shows plots of correlation sum C vs. probing distance r for embedding dimensions m=2-20. Graphs (c) and (d) show the correlation dimension and maximal Lyapunov exponent, respectively, as a function of m. The squares in (c) are for the G=2.25 dB signal. All other data in Figure 30 are for the G=2.5 dB signal. The approaches for attractor construction and correlation sum calculation are the same as in (Wu, Hagerstrom, Eykholt, Kondrashov, and Kalinikos, 2009). The calculation of the maximal Lyapunov exponents involved the following steps: (Rosenstein, Collins, and De Luca, 1993) (1) construction of the attractor; (2) identification of the nearest neighbor point to each of the points

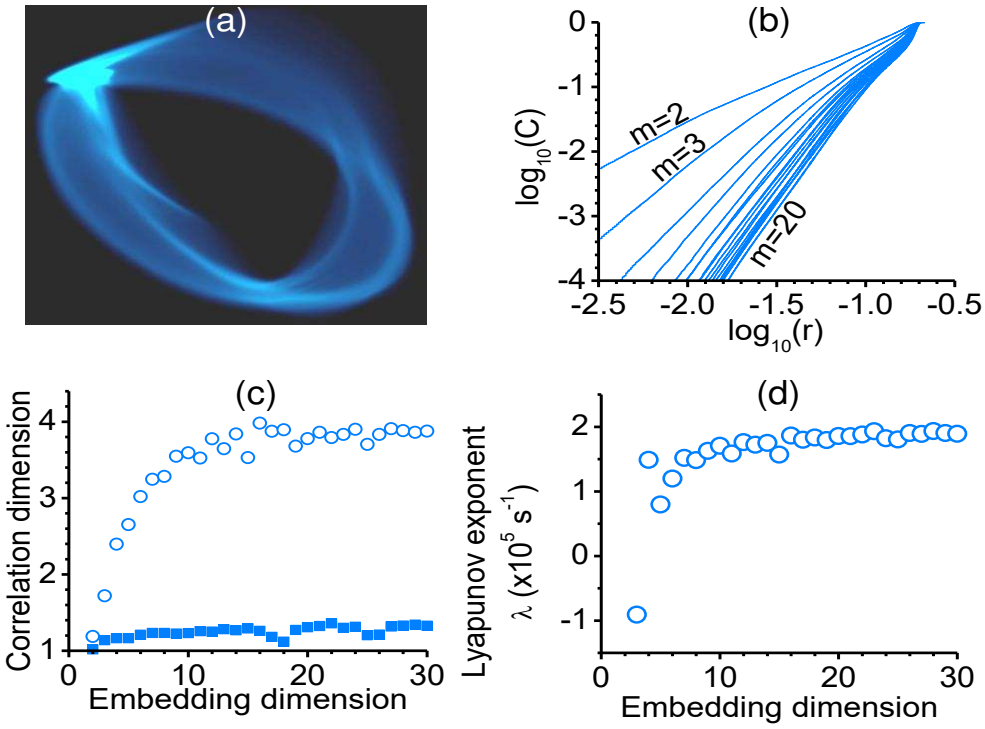

Figure 30. Chaotic characterization of time-domain ring signals.

on the attractor; (3) examination on how these points separate as time increases; (4) average of the logs of the separations for a given time; (5) plotting of the average as a function of time; and (6) determination of the slope of the linear region in the plot. The obtained slopes were taken to be the maximal Lyapunov exponent □.

The attractor in Figure 30(a) is smooth and has a visible structure. The correlation plots in (b) all show a linear regime, in which the slopes of the plots yield the dimension data shown in (c). The data in (c) clearly demonstrate saturation behavior and indicate a fractal dimension of about 1.27 for the *G*=2.25 dB signal and a higher dimension of about 3.83 for the *G*=2.5 dB signal. The response in (d) shows a saturation of λ at about 1.9×10^5 s^{-1}. These results clearly confirm the chaotic nature of the measured signals. Note that the anomalously negative value

of λ for m=3 is due to the fact that the embedding dimension m is less than the fractal dimension of the attractor.

5.4 **Numerical simulations of chaotic solitons**

The above-described responses were reproduced by numerical modeling. The modeling was carried out in collaboration with Professor Lincoln Carr's group in Colorado School of Mines. The results described in this section were mainly obtained by Mr. Justin Anderson from the Carr's group.

Numerical modeling was performed with the following GLNLS equation:

$$i\frac{\partial u}{\partial t} = \left[-\frac{D}{2}\frac{\partial^2}{\partial x^2} + iL + (N + iC)|u|^2 + (S + iQ)|u|^4 \right] u, \tag{5.1}$$

where u is a unitless spin-wave amplitude, D is the dispersion, N and S are the cubic and quintic nonlinearity, respectively, t is the 'temporal' evolution coordinate, x is the 'spatial' coordinate of propagation boosted to the group velocity of the envelope, and L, C, and Q are the linear, cubic, and quintic gains (if positive) or losses (if negative), respectively. Note that similar equations have been used to model exciton-polariton Bose-Einstein condensates (Amo, et al., 2009) and mode-locked lasers (Ablowitz and Horikis, 2009).

The measurements indicate that nonlinearity and dispersion are the dominant sources of envelope shaping for spin waves and that the losses present in the ring are fully compensated by the amplifier. This imposed two constraints on modeling. (1) The coefficients N and D must be orders of magnitude larger than L, C, and Q. (2) The linear amplifier must compensate both the linear and nonlinear losses present in the film, requiring a net averaged linear gain (L>0).

The dissipative terms represent the net gain and loss processes occurring in the ring averaged over several round trip times. One expects the use of this approximation to be valid when the time scale of envelope modulation is greater than the soliton round trip time. This condition is met by all ring gains in this work.

Simulations were performed using adaptive time-step Runga-Kutta for 'temporal' evolution and pseudospectral techniques for 'spatial' propagation. Periodic boundary conditions mimicked the propagation of a single soliton around the ring. Experimentally measured *D* and *N* values were used to generate a stable soliton train which then numerically propagated in the YIG strip with higher order nonlinearity. The cubic dissipation represented nonlinear loss processes ($C<0$). $Q>0$ was used to saturate the nonlinear loss. All simulations were run with $\max(|u|^2)<1$ and the quintic nonlinearity was evaluated separately as a higher order nonlinearity ($S < 0$) and as a high-power saturation of cubic nonlinearity ($S > 0$). Finite correlation dimensions were observed numerically only for $S > 0$. The amplitude of envelope modulation was seen to vary with the magnitude of *S*, while increases in gain quickly destroyed the solitonic nature of the pulse.

Figure 31 illustrates typical simulation data. The left and right columns show data for chaotic solitons with amplitude variations of 2.0% and 5.1%, respectively. These two variation levels are chosen because they match the experimental variations of the G=2.25 dB and G=2.5 dB signals, respectively. The simulation used the following parameters: $N = -9.0\times10^9$ rad/s, $D = 4.5\times10^3$ cm^{2}rad/s, $L = 5.9\times10^5$ rad/s, $C = -5.9\times10^5$ rad/s, and $Q = 5.9\times10^5$ rad/s. The value of S was taken as 6.0×10^9 rad/s for the data with 2.0% variation and 12.0×10^9 rad/s for the data with 5.1% variation. The top and middle rows give power profiles in different time scales, which show trains of chaotic solitons just like those in Figure 105 (a)-(c). The two graphs in the bottom row show the correlation dimension data. The left one indicates a fractal dimension of about 1.26, which closely matches that of the G=2.25 dB signal. The right one indicates a dimension of about 1.66, which is lower than that of the G=2.5 dB signal. One can see that the simulations reproduced measured responses in terms of the amplitude variation and qualitative structure for all gains. The correlation dimensions were reproduced only at low gains. The

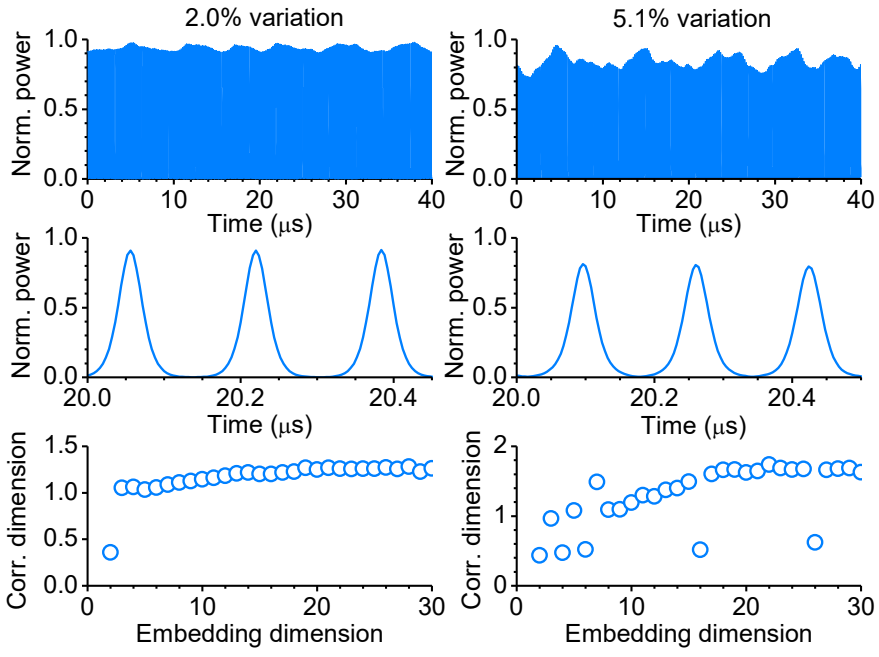

Figure 31. Simulation results for chaotic spin-wave solitons.

lack of a quantitative agreement for the high dimensional chaos suggests that the periodic nature of the active feedback is not negligible and the use of averaged gain parameters is not appropriate for G>2.25dB. Preliminary studies of an iterative GLNLS model for the feedback ring indicate promise for high gain descriptions without the use of a saturated nonlinearity.

In summary, this chapter reports on the experimental observation of a spin-wave soliton that circulates in a magnetic film feedback ring with chaotically varying amplitude. The observed responses were reproduced by numerical simulations. There are two additional points of note. (1) There is a recent work on the propagation of a chaotic train of soliton-like spin-wave pulses in a YIG element (Ustinov, *et al.*, 2011). Two significant differences exist between that previous work and the present work. First, different nonlinear systems were used. The YIG element in (Ustinov, Demidov, Kondrashov, Kalinikos, and Demokritov, 2011) represents a dissipative system, rather than the driven ring system considered in the present work and in the theoretical prediction of chaotic solitons (Soto-Crespo and Akhmediev, 2005; Karar, Smy, and Steele, 2008; Zhao, Tang, and Liu, 2006). Second, the nonlinear objects observed are different. In that work, the soliton-like pulses have their amplitudes differing chaotically from one to another, and it is unknown whether the amplitude of each pulse changes chaotically. In stark contrast, the present work involves a single soliton only. This soliton circulates in the ring with its amplitude changing chaotically from one round trip to another. (2) The present work was realized in a regime where three-wave interactions were prohibited. Recent work has shown that soliton-like pulses with a chaotic phase modulation can develop in a regime where both three- and four-wave processes are allowed (Beginin, Grishin, and Sharaevsky, 2008).

CHAPTER 6

OBSERVATION OF SPIN-WAVE DARK SOLITON PAIRS IN YTTRIUM IRON GARNET THIN FILMS

The formation of a pair of dark solitons from a single nonlinear black spin-wave pulse was observed for the first time. The experiments were carried out with a long and narrow magnetic yttrium iron garnet film strip in a surface-spin-wave configuration. The black spin-wave pulses were excited by the use of microwave black pulses – large-amplitude microwaves with narrow square-like dips. Pairs of black solitons were observed in certain input power and input black pulse width ranges. For each pair, the two solitons show opposite π phase jumps and an overall phase change of zero. Beyond those power and width ranges, one also observed pairs of gray solitons that also showed opposite phase jumps and a zero total phase change. The formation of a single black soliton was also observed, but only for an input black pulse that was very narrow. The experimental observations were re-produced by numerical simulations based on the complex Ginzburg-Landau equation.

6.1 **Introduction**

Due to dispersion, a narrow dip on a continuous wave broadens as the wave propagates. If the wave amplitude is large, the dip broadening can be further enhanced by the nonlinearity. This is true for waves that have an attractive nonlinearity. For waves with a repulsive nonlinearity, however, the nonlinearity can give rise to a self-narrowing effect which can cancel the dispersion-produced broadening of the dip. When a fine balance is achieved between the two effects, the dip on the continuous wave can evolve into a stable localized excitation – an envelope dark soliton. (Hasegawa & Kodama, 1995; Kivshar & Luther-Davies, 1998;

Remoissenet, 1999; Slavin & Zaspel, 2002; Sulem & Sulem, 1999) There are two types of dark solitons, black and gray. When the dip amplitude at the soliton center goes to zero, one has a black soliton. When the amplitude at the dip is nonzero, one has a gray soliton. Both the black and gray solitons have a jump in the carrier wave phase at their centers. For black solitons, such a phase jump is exactly equal to π. For gray solitons, the jump is between 0 and π.

From a physical point of view, a straightforward way to excite a dark envelope soliton is to use a dark input pulse – a narrow dip in the amplitude or intensity of a continuous wave background. This approach has indeed been previously used to excite black envelope solitons, for example, for surface spin waves in magnetic yttrium iron garnet (YIG) thin film strips (Chen, Tsankov, Nash, & Patton, 1993) and for lasers in photorefractive crystals (Chen, Mitchell, & Segev, 1996). Theoretically, however, an initial dark signal should not evolve into a single dark soliton. Rather, it should develop into a pair of dark solitons that have opposite phase jumps and an overall phase change of zero. (Blow & Doran, 1985; Slavin, Kivshar, Ostrovskaya, & Benner, 1999; Chen, Segev, Singh, Coskun, & Christodoulides, 1997; Zhang, Lu, Guo, Li, & Liu, 2012) This phase condition is needed because of symmetry conservation, namely, that the initial experimental signal has no phase difference across the dark region, and the zero-phase-change property should be conserved. (Blow & Doran, 1985) Experimentally, the formation of such a dark soliton pair from a single dark input signal has been observed not only for temporal solitons in optical fibers, (Krokel, Halas, Giuliani, & Grischkowsky, 1988; Weiner, et al., 1988) but also for spatial optical solitons in Kerr-like media, (Luther-Davies & Yang, 1992) photovoltaic media, (Taya, Bashaw, Fejer, Segev, & Valley, 1996) and photorefractive crystals,

(Chen, Mitchell, & Segev, 1996) but the phase signature of the solitons, namely, opposite phase jumps, has never been demonstrated so far.

6.2 Experiment setup and parameters

This chapter reports the first unambiguous experimental evidence for opposite phase jumps of dark soliton pairs. The experiments were carried out with a YIG film strip in a surface-spin-wave configuration (Kabos & Stalmachov, 1994; Stancil & Prabhakar, 2009) and used as an input signal a single black spin-wave pulse with no phase change. A pair of black solitons with opposite π phase jumps was observed in certain input power and input pulse width ranges. Beyond those ranges, one also observed pairs of gray solitons that also showed opposite phase jumps and an overall phase change of zero. The formation of a single black soliton from a dark pulse, similar to that reported previously, (Chen, Tsankov, Nash, & Patton, 1993) was also observed, but only for an initial black pulse that was very narrow. The experimental results were supported by numerical simulations which made use of the complex Ginzburg-Landau equation (Kovalev & Kosevich, 1976; Barashenkov & Makhankov, 1988) and the experimental parameters.

Figure 32(a) shows a schematic diagram of the experimental setup. The core components include a long and narrow YIG thin film strip and two microstrip line transducers placed on the top the YIG strip for the excitation and detection of spin waves. The YIG film strip is magnetized to saturation by an external magnetic field which is applied in the plane and perpendicular to the length of the YIG film strip. This film/field configuration supports the propagation of surface spin waves (Kabos & Stalmachov, 1994; Stancil & Prabhakar, 2009) which show a repulsive nonlinearity. (Sulem & Sulem, 1999; Wu M. , 2011) The microwave

switch is fed by a continuous microwave source and is controlled by a fast pulse generator. It generates black microwave pulses for the excitation transducer. The signals from the detection transducer are analyzed directly by a fast oscilloscope and a spectrum analyzer, without using any microwave amplifiers or diodes.

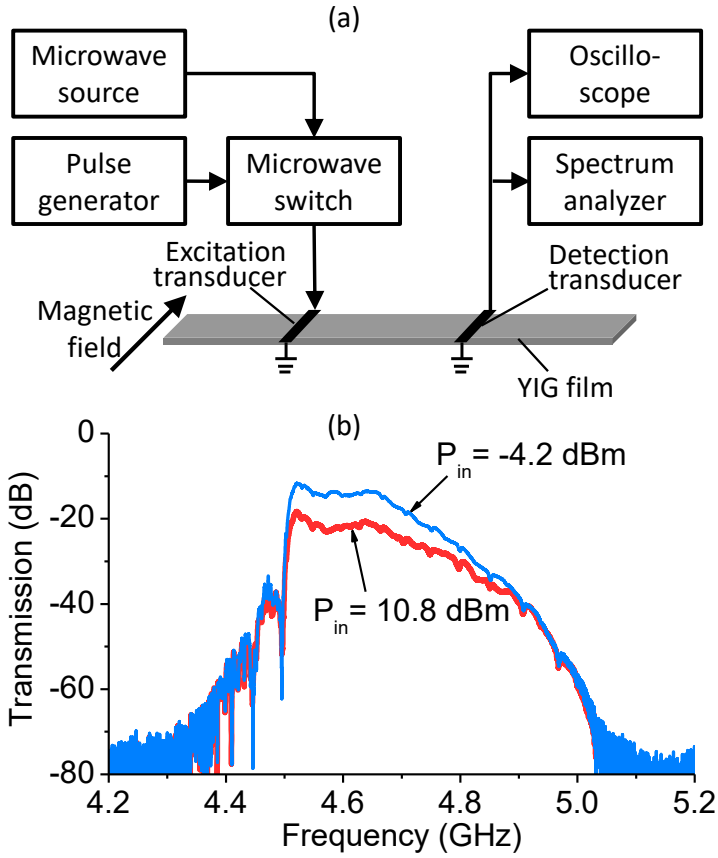

Figure 32. (a) Schematic of the experimental configuration. (b) Transmission responses of the transducer/YIG/transducer structure measured at two different input power levels (P_{in}), as indicated.

For the experimental data presented below, the YIG film strip was 5.6 μm thick, 2 mm wide, and 50 mm long. It was cut from a larger single-crystal YIG wafer grown on a gadolinium gallium garnet substrate by liquid phase epitaxy. The magnetic field was set to 909 Oe. The microstrip line transducers were 50 μm wide and 2 mm long and were end-shorted. The

separation of the two transducers was set to 6.8 mm. The input pulses applied to the excitation transducer were square-like dips on a continuous microwave signal, with the amplitude at the dips less than 5% of the amplitude of the microwave background. The power level of the microwave background was controlled by a microwave amplifier and a tunable microwave attenuator inserted between the microwave switch and the excitation transducer. The amplifier had a 30 dB dynamic range, a peak output power of 2 W, and a linear response from 2 to 8 GHz. These characteristics ensured that the nonlinear response of the system was determined solely by the YIG film.

Figure 32(b) shows the transmission responses (S_{21}) of the transducer/YIG/transducer structure measured at two different input power levels (P_{in}), as indicated. One can see three results from the data in Figure 32(b). (1) The spin-wave frequency range is about 4.5-5.0 GHz. For the data presented below, the carrier wave frequencies of the input signals all fell within this frequency range. (2) The transmission profiles are relatively smooth. This indicates that the spins on the film surfaces are unpinned and a repulsive nonlinearity is expected for the entire 4.5-5.0 GHz frequency range. In films with strongly pinned surface spins, one has a repulsive nonlinearity only in narrow frequency ranges. (Kalinikos & Slavin, 1986; Kalinikos, Kovshikov, & Slavin, 1988) (3) The transmission for P_{in}=10.8 dBm is notably smaller than that for P_{in}=-4.2 dBm. This difference results from nonlinear damping, (Scott, Patton, Kostylev, & Kalinikos, 2004) which was considered in the numerical simulations presented below.

6.3 **Experiment results on black solitons**

Figures 33 and 34 present representative experimental data for the formation of dark solitons. Figure 33 shows the output signals measured for a fixed input black pulse width

τ_{in}=29 ns and different P_{in} levels, as indicated. Here P_{in} denotes the power level of the microwave background of the signals applied to the excitation transducer. In contrast to Figure 33, Figure 4 shows the output signals obtained for a fixed input power P_{in} =8.3 dBm and different pulse widths, as indicated. In both the Figures, the voltage waves are shown in light blue, while the corresponding phase profiles are shown in light red. The black and gray solitons are marked with "**B**" and "**G**", respectively. Note that all the data were obtained with an input carrier wave frequency of 4.609 GHz, and the phase profiles show the phase data of the output signals relative to the phase of a reference continuous wave with the same frequency as the input carrier waves. (Nash, Kabos, Staudinger, & Patton, 1998)

The data in Figs. 33(a) and (b) show the key results of this work – the demonstration of a pair of black solitons. For each soliton, the dip almost goes to zero and the phase shows a π jump at its center. For each pair, the phase jumps of the two solitons are opposite, and the overall phase change is zero. With an increase in P_{in}, from 3.3 dBm to 8.3 dBm, the black soliton pair evolves into a pair of gray solitons, as shown in Figure 33(c). For each gray soliton, the dip amplitude is nonzero and the phase jump is less than π (about 0.92π). Nevertheless, the two solitons have opposite phase jumps and the total phase change is almost zero, the same as the black soliton pairs in Figs. 33(a) and (b). When P_{in} is increased to 13.3 dBm and then to 18.3 dBm, one observes only a single gray soliton, as shown in Figs. 33(d) and (e). With a further increase in P_{in}, one observes non-solitonic waveforms only, as shown in Figure 33(f). Note that, independent of the value of P_{in}, the zero-phase-change condition is always satisfied.

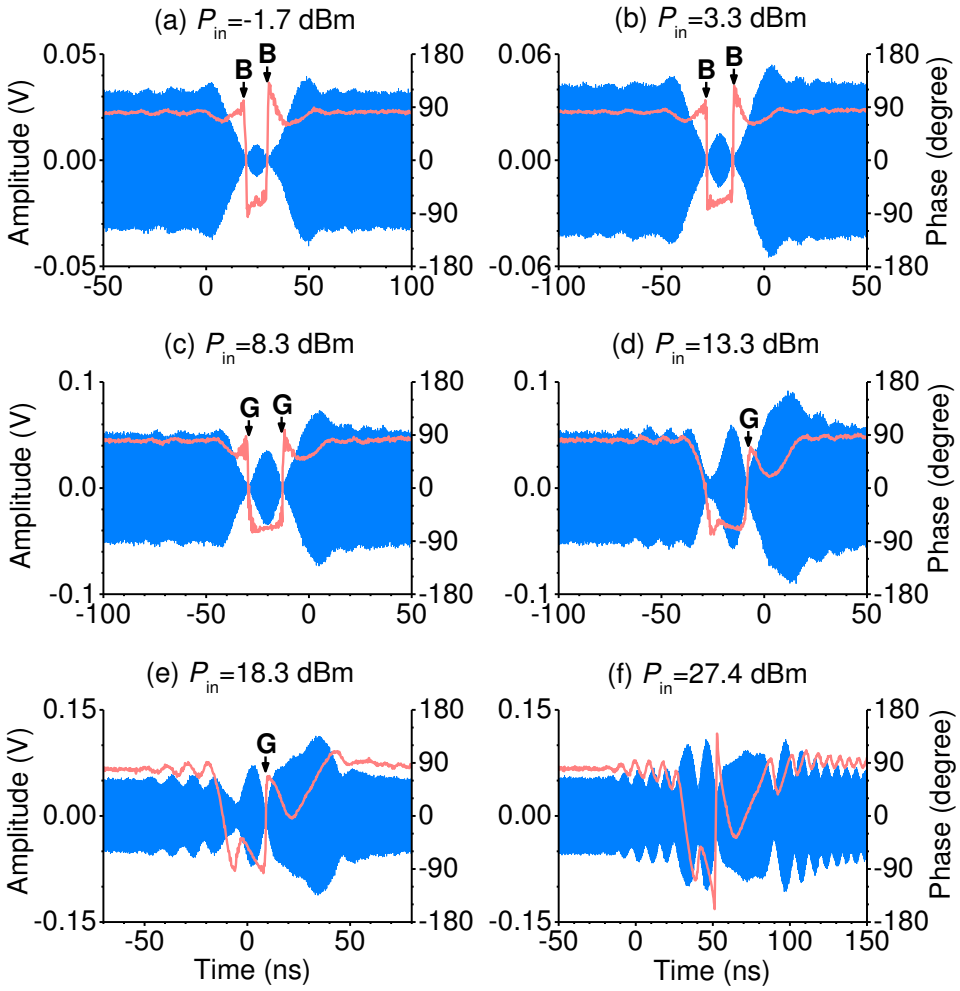

Figure 33. Output signals obtained for a fixed input pulse width of 29 ns and different input power levels (P_{in}), as indicated. The voltage wave signals are shown in light blue, while the wave phase profiles are shown in light red. The black and gray solitons are marked by "**B**" and "**G**", respectively.

The data in Figure 34 show that the formation of dark soliton pairs also depends on the width of the initial black pulse. Figure 34(b) shows a pair of black solitons obtained at τ_{in}=29 ns. It is essentially the same as the pairs shown in Figs. 33(a) and (b). For a narrower initial black pulse with τ_{in}=23 ns, however, one observes only a single black soliton, as shown in Figure 34(a). As discussed shortly, this single black soliton is similar to the one reported. (Chen, Tsankov, Nash, & Patton, 1993) In contrast, for broader initial pulses, one observes multiple gray solitons or non-solitonic dips, as shown in Figs. 34(c)-(f). At τ_{in}=71 ns, for example, the

signal consists of three gray solitons and two non-solitonic dips, as shown in Figs. 34(e). It should be noted that the overall phase change is always zero for all the data shown in Figure 34, the same as for the data in Figure 33.

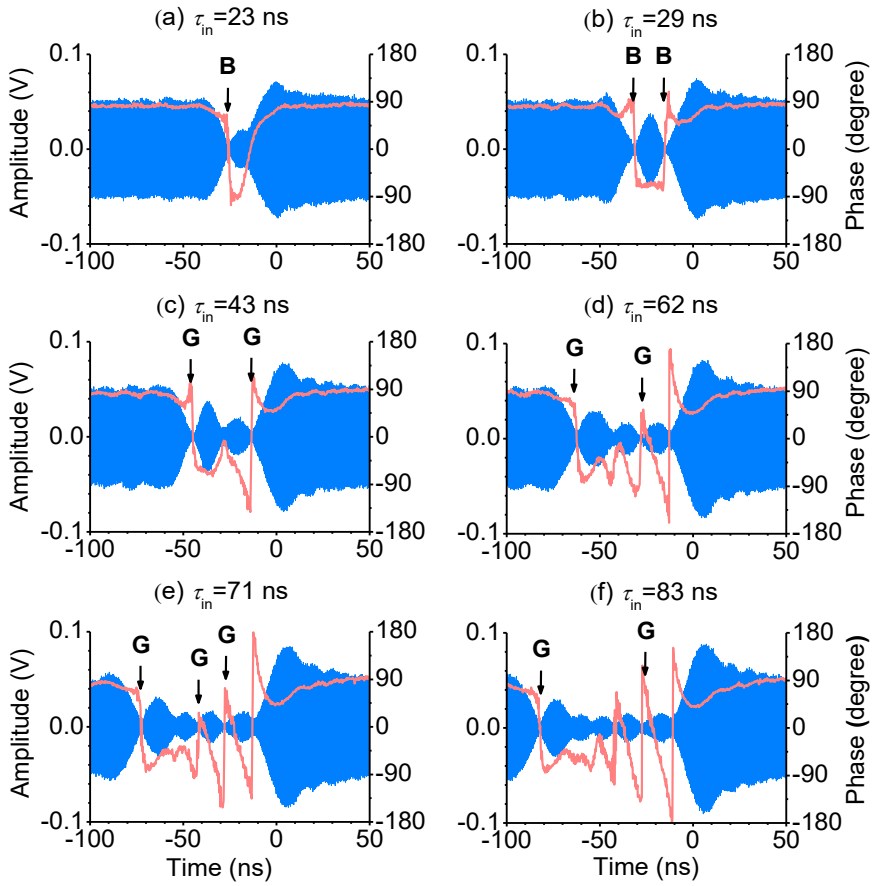

Figure 34. Output signals obtained for a fixed input power of 8.3 dBm and different input pulse widths (τ_{in}), as indicated. The voltage wave signals are shown in light blue, while the wave phase profiles are shown in light red. The black and gray solitons are marked by "**B**" and "**G**", respectively.

The above-presented experimental results can be reproduced by numerical simulations using the so-called complex Ginzburg-Landau equation (Kovalev & Kosevich, 1976; Barashenkov & Makhankov, 1988)

$$\mathrm{i}\left[\frac{\partial u}{\partial t}+v_{\mathrm{g}}\frac{\partial u}{\partial x}+\eta u\right]-\frac{1}{2}D_2\frac{\partial^2 u}{\partial x^2}-\frac{1}{6}D_3\frac{\partial^3 u}{\partial x^3}+\left(N+\mathrm{i}\nu\right)|u|^2 u=0 \tag{6.1}$$

where u is the spin-wave amplitude, x is the spatial coordinate, t is the temporal coordinate, v_{g} is the group velocity, η is the damping coefficient, D_2 is the dispersion coefficient, D_3 is the third-order dispersion coefficient, N is the nonlinearity coefficient, and ν is the nonlinear damping coefficient. In comparison with the standard nonlinear Schrödinger equation, (Remoissenet, 1999) equation (6.1) incorporates three additional terms – one describes the third-order dispersion and the other two describe the linear and nonlinear damping of the spin waves. These additional terms are required in order to re-produce the experimental responses.

The simulations used the split-step method to solve the derivative terms with respect to x and used the Runge-Kutta method to solve the equation with the rest of the terms. (Weideman & Herbst, 1986) The split-step method uses Fourier transformation to convert the space domain (x) of the equation into the wave-number domain (k), turning the differential parts of the equation into simpler linear algebra. A high-order Gaussian-type dip, instead of a square black pulse, was used in simulations as the initial black pulse. The use of a square pulse as an initial black pulse gave rise to numerical noise due to the discontinuities at the pulse edges. Though it is also possible to use the fundamental Gaussian function, a high-order Gaussian dip better resembles the experimental situation.

Figure 35 shows representative simulation results. In each row, the gray dashed curves show the envelope and phase profiles of the signal measured at certain P_{in} and τ_{in} values, as indicated, while the light blue and light red curves show the simulated envelope and phase profiles, respectively. The simulations presented in Figs. 35(a), (b), and (c) were carried out

with "u_{in}=7×10^{-5} and τ_{in}=29 ns", "u_{in}=8×10^{-4} and τ_{in}=29 ns", and "u_{in}=8×10^{-4} and τ_{in}=23 ns", respectively, where u_{in} denotes the background amplitude of the initial spin-wave signal. The other parameters used are as follows: v_g=3.6×10^6 cm/s, η=5.28×10^6 rad/s, D_2=-3×10^3 rad·cm^2/s, D_3=1 rad·cm^3/s, N=-1×10^{10} rad/s, and v =6.28×10^9 rad/s. Among these parameters, u_{in} is the only fitting parameter, while all others were calculated based on the properties of the YIG film sample. Note that the experimental and numerical results in Figure 35 are normalized in amplitude and shifted in time for the purpose of easy comparisons.

One can see from the data in Figure 35 that the experimental responses can be well reproduced by numerical simulations. Furthermore, the simulations presented in Figure 35 together with additional simulations indicate two important results as follows. First, a black spin-wave pulse genetically evolves into a pair of black solitons, as in Figs. 33(a) and (b) and Figure 34(b), or a pair of gray solitons, as in Figs. 33(c), for a certain initial power range and a certain initial pulse width range. All of the soliton pairs show an overall phase change of zero. These results agree with theoretical expectations. (Blow & Doran, 1985; Chen, Segev, Singh, Coskun, & Christodoulides, 1997; Zhang, et al., 1998) Second, when the initial black pulse is too narrow to evolve into a soliton pair, it may develop into a single black soliton-like object as shown in Figure 35(c). This is similar to that reported previously (Chen, Tsankov, Nash, & Patton, 1993) and is consistent with the standard nonlinear Schrödinger equation model. The existence of a single black soliton, however, does not break the zero-phase-change condition. This is clearly shown by the two phase profiles shown in Figure 35(c). The simulated profile shows a phase jump of -π at the soliton center, a gradual increase in the phase for the waveforms both leading and following the soliton, and an overall phase change of zero. The experimental profile shows a slightly different feature - the phase undergoes a jump of -π at the soliton's

center and a gradual phase increase of π for the waveform following the soliton. Besides, the simulations also indicated that the slight asymmetry of the experimental amplitude and phase profiles was associated with the third-order dispersion.

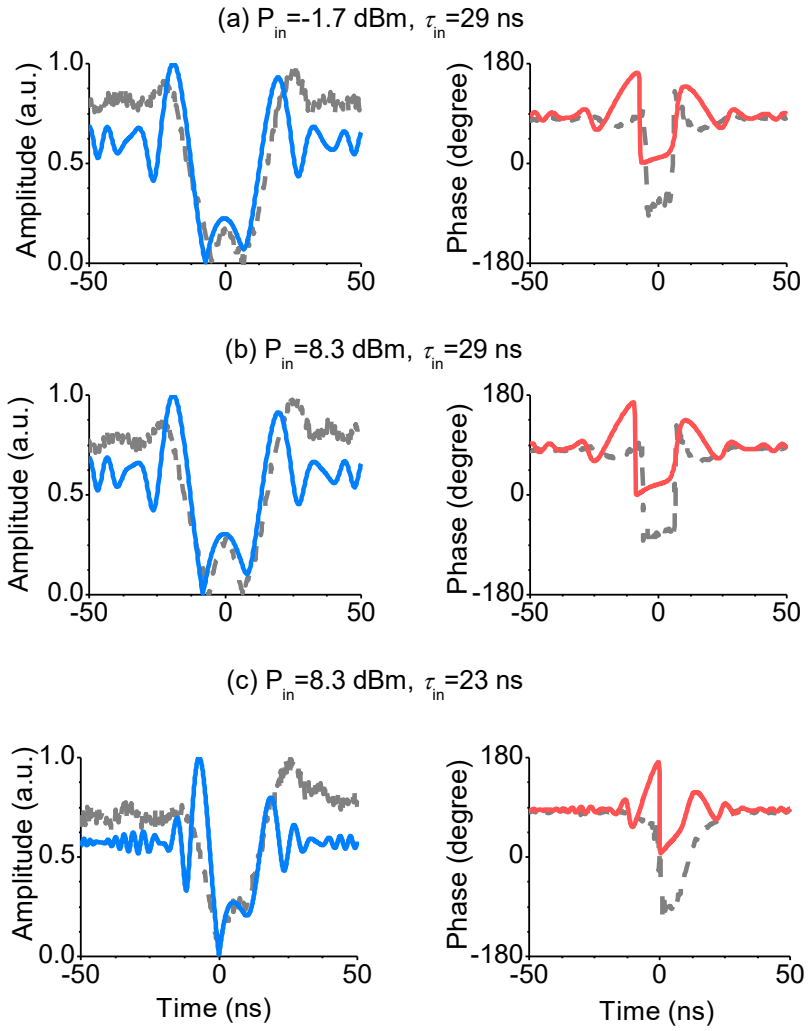

Figure 35. Comparisons between experimental data and numerical simulations. The gray dashed curves show the data measured at different input power or input pulse widths, as indicated. The light blue and light red curves show the simulated envelope and phase profiles, respectively. The simulations shown in (a), (b), and (c) were obtained with "$u_{in}=7\times10^{-5}$ and $\tau_{in}=29$ ns", "$u_{in}=8\times10^{-4}$ and $\tau_{in}=29$ ns", and "$u_{in}=8\times10^{-4}$ and $\tau_{in}=23$ ns", respectively. For easy comparisons, all the profiles were normalized in amplitude and shifted in time.

Several important points should be noted. First, in addition to providing the first experimental evidence for the intrinsic phase characteristic of dark solitons pairs, this work also demonstrates that dark soliton pairs not only exist in optical systems, (Chen, Mitchell, & Segev, 1996; Krokel, Halas, Giuliani, & Grischkowsky, 1988; Weiner, et al., 1988; Luther-Davies & Yang, 1992; Taya, Bashaw, Fejer, Segev, & Valley, 1996) but also take place in spin-wave systems, thereby indicating the universal feature of the dark soliton pair phenomenon. Second, previous work on spatial solitons has also indicated that an initial dark signal could also develop into a sequence of dark solitons whose number is more than two and is even. (Chen, Mitchell, & Segev, 1996; Chen, Segev, Singh, Coskun, & Christodoulides, 1997) Future work is of importance that demonstrates such development for temporal dark solitons and studies the phase features of the solitons. Third, the numerical simulations in this work indicate that the complex Ginzburg-Landau equation (Kovalev & Kosevich, 1976; Barashenkov & Makhankov, 1988) appears to be a more accurate model for nonlinear spin waves in magnetic thin films than the standard nonlinear Schrödinger equation, although the latter has been proved to be a generally good model for many different types of nonlinear waves. (Remoissenet, 1999; Sulem & Sulem, 1999) Finally, the simulations in this work also revealed the existence of a soliton triplet that consists of a bright soliton embraced by two black solitons. The data in Figure 33(c) presents a similar effect. Future study, both experimental and theoretical, on such soliton triplets is of great interest.

In summary, this chapter reported on the formation of black soliton pairs from nonlinear black spin-wave pulses. For each soliton, the dip almost goes to zero and the phase shows a π jump at its center. For each pair, the phase jumps of the two solitons have opposite signs, and the overall phase change is zero. The formation of such black soliton pairs requires the initial

black pulses to have appropriate power and widths. Beyond them, the formation of a gray soliton pair is also possible, which also shows opposite phase jumps and a zero overall phase change as the black soliton pairs. When the initial pulses are too narrow to support black or gray soliton pairs, they can evolve into single black solitons. This is consistent with the standard nonlinear Schrödinger equation (Remoissenet, 1999; Sulem & Sulem, 1999) and the previous experimental observation. (Chen, Tsankov, Nash, & Patton, 1993)

CHAPTER 7

FORMATION OF BRIGHT SOLITONS FORM WAVE PACKETS WITH REPULSIVE NONLINEARITY

Formation of bright envelope solitons from wave packets with a repulsive nonlinearity was observed for the first time. The experiments used surface-spin-wave packets in magnetic yttrium iron garnet (YIG) thin film strips. When the wave packets are narrow and have low power, they undergo self-broadening during the propagation. When the wave packets are relatively wide or their power is relatively high, they can experience self-narrowing or even evolve into bright solitons. The experimental results were reproduced by numerical simulations based on a modified nonlinear Schrödinger equation model.

7.1 Introduction

Solitons are a universal phenomenon in nature, appearing in systems as diverse as water, optical fibers, electromagnetic transmission lines, deoxyribonucleic acid, and ultra-cold quantum gases. The formation of solitons from large-amplitude waves can be described by paradigmatic nonlinear equations, one of which is the nonlinear Schrödinger equation (NLSE). In the terms of the NLSE model, two classes of envelope solitons, bright and dark, can be excited in nonlinear media. A bright envelope soliton is a localized excitation on the envelope of a large-amplitude carrier wave. It typically takes a hyperbolic secant shape and has a constant phase across its width. (Nash, Kabos, Staudinger, & Patton, 1998) A dark envelope soliton is a dip or null in a large-amplitude wave background. When the dip goes to zero, one has a black soliton. When the amplitude at the dip is nonzero, one has a gray soliton. A dark soliton has a jump in phase at its center. For a black soliton, such a phase jump equals to π. For a gray soliton, the phase jump is between 0 and π. The envelope of a dark soliton can be described by

a unique function. (Remoissenet, 1999) For a black soliton, this function is typically a hyperbolic tangent function.

According to the NLSE model, the formation of a bright soliton from a large-amplitude wave packet is possible in systems with an attractive (or self-focusing) nonlinearity and is prohibited in systems with a repulsive (or defocusing) nonlinearity. The underlying physics is as follows. The attractive nonlinearity produces a pulse self-narrowing effect; at a certain power level the self-narrowing can balance the dispersion-induced pulse self-broadening and give rise to the formation of a bright envelope soliton. In contrast, in systems with a repulsive nonlinearity the nonlinearity induces self-broadening of the wave packet, just as the dispersion does, and thereby disables the formation of a bright soliton. Previous experiments show good agreements with these theoretical predictions: the formation of bright solitons from wave packets has been demonstrated in different systems with an attractive nonlinearity, (Chen, Tsankov, Nash, & Patton, 1994) while the self-broadening has been observed for wave packets in systems with a repulsive nonlinearity. (Chen, Tsankov, Nash, & Patton, 1993)

7.2 **Experimental results obtained with transducer structures**

This chapter reports on the first observation of the formation of bright solitons from wave packets with a repulsive nonlinearity. The experiments made use of spin waves traveling along long and narrow magnetic yttrium iron garnet ($Y_3Fe_5O_{12}$, YIG) thin film strips. The YIG strips were magnetized by static magnetic fields applied in their planes and perpendicular to their length directions. This film/field configuration supports the propagation of surface spin waves with a repulsive nonlinearity. (Stancil D. D., 1993) To excite a spin wave packet in the YIG strip, a microstrip line transducer was placed on one end of the YIG strip and was fed with a

microwave pulse. As the spin wave packet propagates along the YIG strip, it was measured by either a secondary microstrip line or a magneto-dynamic inductive probe located above the YIG strip. When the input microwave pulse is relatively narrow and has relatively low power, one observes the broadening of the spin wave packet during its propagation. At certain large input pulse widths and high power levels, however, the spin wave packet undergoes self-narrowing and evolves into a bright envelope soliton. The formation of this soliton is contradictory to the prediction of the standard NLSE model, but was reproduced by numerical simulations with a modified NLSE model that took into account damping and saturable nonlinearity.

Figure 36 shows representative data on the formation of bright solitons from surface spin-wave packets. Graph (a) shows the experimental configuration. The YIG film strip was cut from a 5.6-μm-thick (111) YIG wafer grown on a gadolinium gallium garnet substrate. The strip was 30 mm long and 2 mm wide. The magnetic field was set to 910 Oe. The input and output transducers were 50-μm-wide striplines and were 6.3 mm apart. The input microwave pulses had a carrier frequency of 4.51 GHz. Note that, in Figure 1 and other Figures as well as the discussions below, P_{in} denotes the nominal microwave pulse power applied to the input transducer, τ_{in} denotes the half-power width of the input microwave pulse, P_{out} is the power of the output signal, and τ_{out} represents the half-power width of the output pulse. In Figure 36, graphs (b), (c), (d), (f), and (g) give the power profiles of the output signals measured with different P_{in} and τ_{in} values, as indicated. The circles in (d) shows a fit to the hyperbolic secant squared function. (Ablowitz & Segur, Solitons and the Inverse Scattering Transform, 1985; Remoissenet, 1999) Graph (e) shows the corresponding phase (θ) profile of the signal shown in (d). Here, the profile shows the phase relative to a reference continuous wave whose frequency equals to the carrier frequency of the input microwave. (Nash, Kabos, Staudinger, & Patton, 1998)

Graph (h) shows the change of τ_{out} with P_{in} for a fixed τ_{in}, as indicated, while graph (i) shows the change of τ_{out} with τ_{in} for a fixed P_{in}, as indicated.

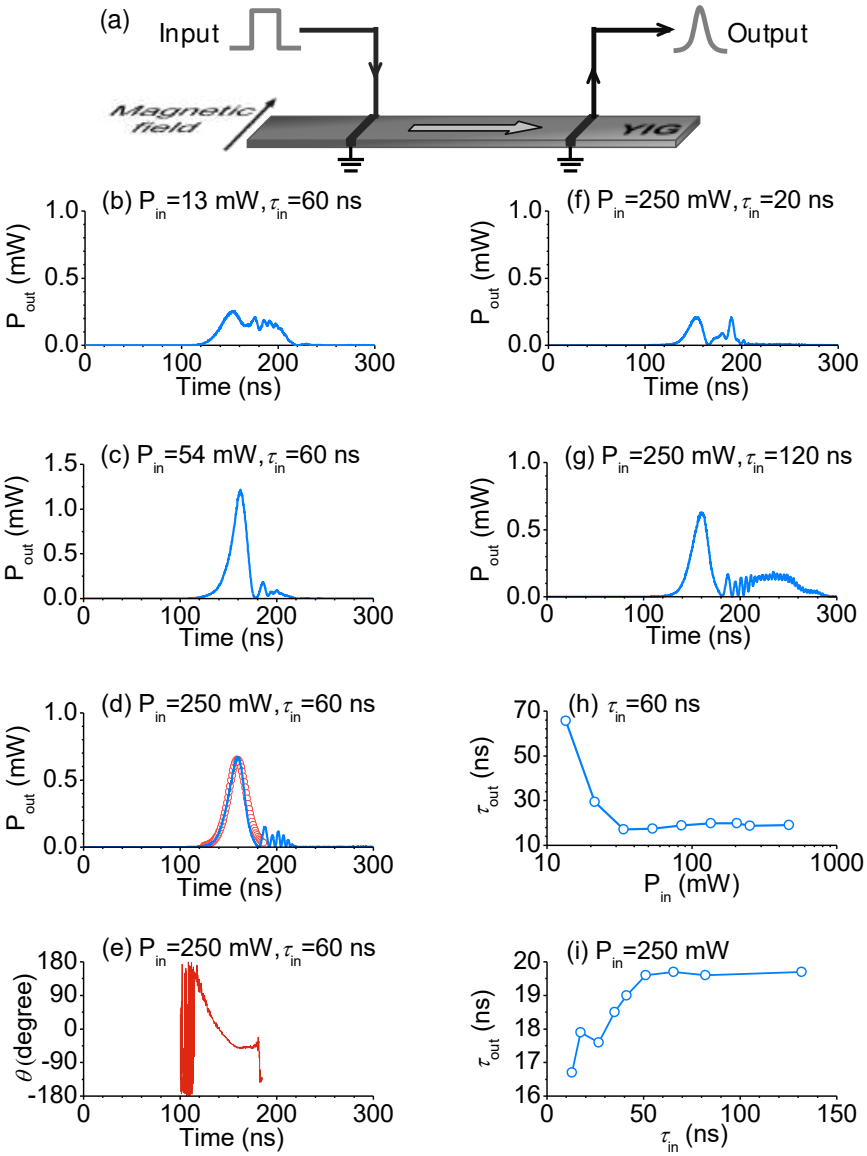

Figure 36. Propagation of spin-wave packets in a 2.0-mm-wide YIG strip. (a) Experimental setup. (b), (c), (d), (f), and (g) Envelopes of output signals obtained at different input pulse power levels. (P_{in}) and widths (τ_{in}). (e) Phase (θ) profile for the signal shown in (d). (h) Width of output pulse (τ_{out}) as a function of P_{in}. (i) Width of output pulse as a function of τ_{in}.

The data in Figure 36 show three important results. (1) The data in Figs. 36 (b)-(e) and (h) show the change of the output signal with the input power P_{in}. One can see that the output pulse is broader than the input pulse when P_{in}=13 mW, as shown in (b), and is significantly narrower when P_{in}>30 mW, as shown in (c), (d), and (h). This indicates that the spin-wave packet undergoes self-broadening at low power and self-narrowing at relatively high power. (2) The data in Figs. 36 (d), (f), (g), and (i) show the change of the output signal with the input pulse width τ_{in}. It is evident that the width of the output pulse increases with τ_{in} when τ_{in}<50 ns and then saturates to about 19.5 ns when τ_{in}>50 ns. These results indicate that the spin-wave packet experiences strong self-narrowing when it is relatively broad. (3) The pulses shown in (d) and (g) are indeed bright solitons. As shown representatively in (d) and (e), they have a hyperbolic secant shape and a constant phase profile at their centers, which are the two key signatures of bright solitons. (Ablowitz & Segur, Solitons and the Inverse Scattering Transform, 1985; Nash, Kabos, Staudinger, & Patton, 1998)

The data from Figure 36 clearly demonstrate the formation of bright solitons from surface spin-wave packets when the energy of the initial signals (the product of P_{in} and τ_{in}) is beyond a certain level. This result is contradictory to the predictions of the NLSE model. One possible argument is that the width of the YIG strip might play a role in the observed formation of bright solitons. To rule out this possibility, similar measurements were carried out with a YIG strip that is an order of magnitude narrower. The main data are as follows.

7.3 **Experiment results obtained with a scanning probe**

Figure 37 gives the data measured with a 0.2-mm-wide YIG strip. This Figure is shown in the same format as in Figure 36. In contrast to the data in Figure 36, the data here were

measured by a 50-Ω inductive probe, (Wu, Kalinikos, & Patton, 2004) rather than a secondary microstrip transducer. The distance between the input transducer and the inductive probe was about 2.6 mm. The magnetic field was set to 1120 Oe. The input microwave pulse had a carrier frequency of 5.07 GHz.

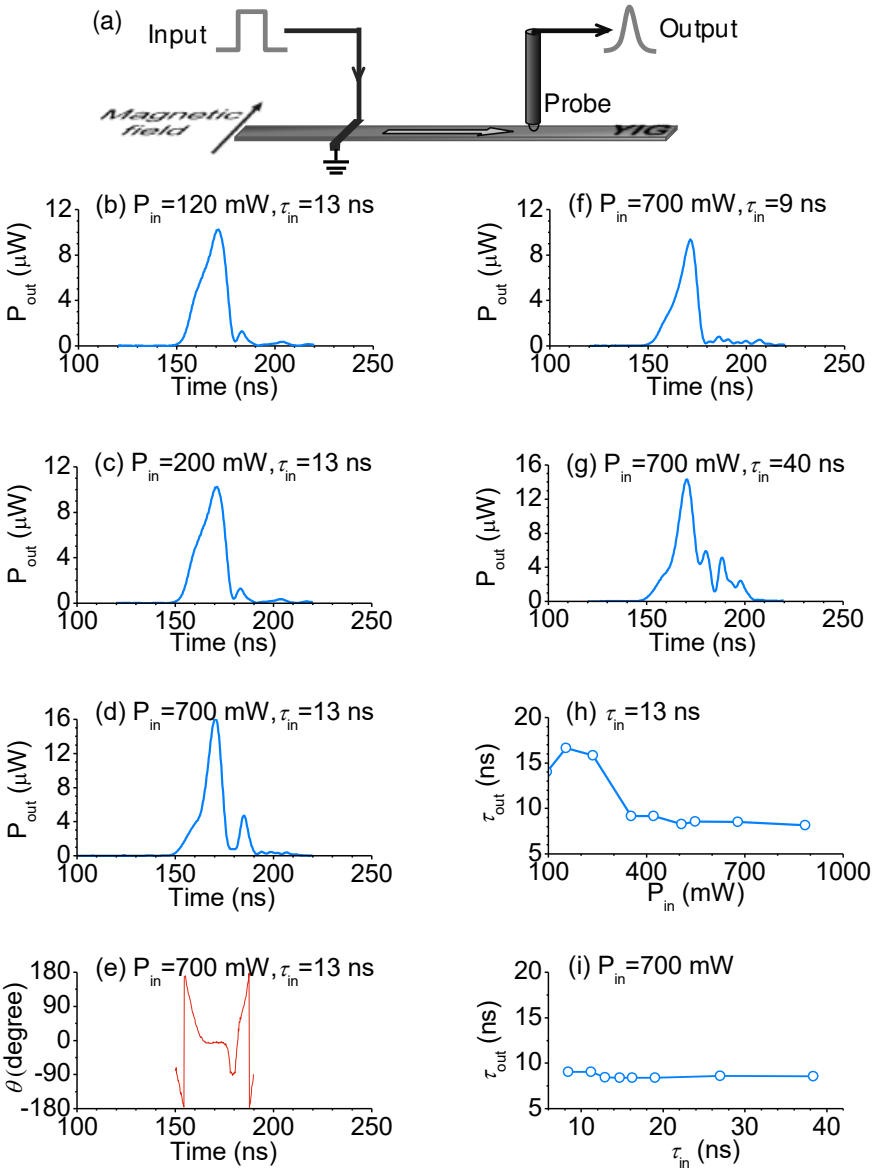

Figure 37. Propagation of spin-wave packets in a 0.2-mm-wide YIG strip. (a) Experimental setup. (b), (c), (d), (f), and (g) Envelopes of output signals obtained at different input pulse power levels (P_{in}) and widths (τ_{in}). (e) Phase (θ) profile for the signal shown in (d). (h) Width of output pulse (τ_{out}) as a function of P_{in}. (i) Width of output pulse as a function of τ_{in}.

The data in Figure 37 show results very similar to those shown in Figure 36. Specifically, the low- power, narrow spin-wave packets undergo self-broadening, as shown in (b), (c), (f), and (h); as the power and width are increased to certain levels, the spin-wave packets experience self-narrowing, as shown in (h) and (i), and can also evolve into solitons, as shown in (d), (e), and (g). Therefore, the data in Figure 37 clearly confirm the results from Figure 36. This indicates that the formation of solitons reported here is not due to any effects associated with the YIG strip width. Note that the solitons shown in Figure 38 are narrower than those shown in Figure 36. This difference results mainly from the fact that the spin-wave amplitudes and dispersion properties were different in the two experiments. The spin-wave dispersion differed in the two experiments because the magnetic fields were different and the wave numbers of the excited spin-wave modes were also not the same.

Turn now to the spatial formation of solitons from surface spin-wave packets. Figure 38 shows representative data. Graph (a) gives the profile of an input signal. The power and carrier frequency of the input signal were 700 mW and 5.07 GHz, respectively. Graphs (b)-(f) give the corresponding output signals measured with the same experimental configuration as depicted in Figure 37(a). The signals were measured by placing the inductive probe at different distances (x) from the input transducer, as indicated. The red curves in (b)-(f) are the corresponding phase profiles.

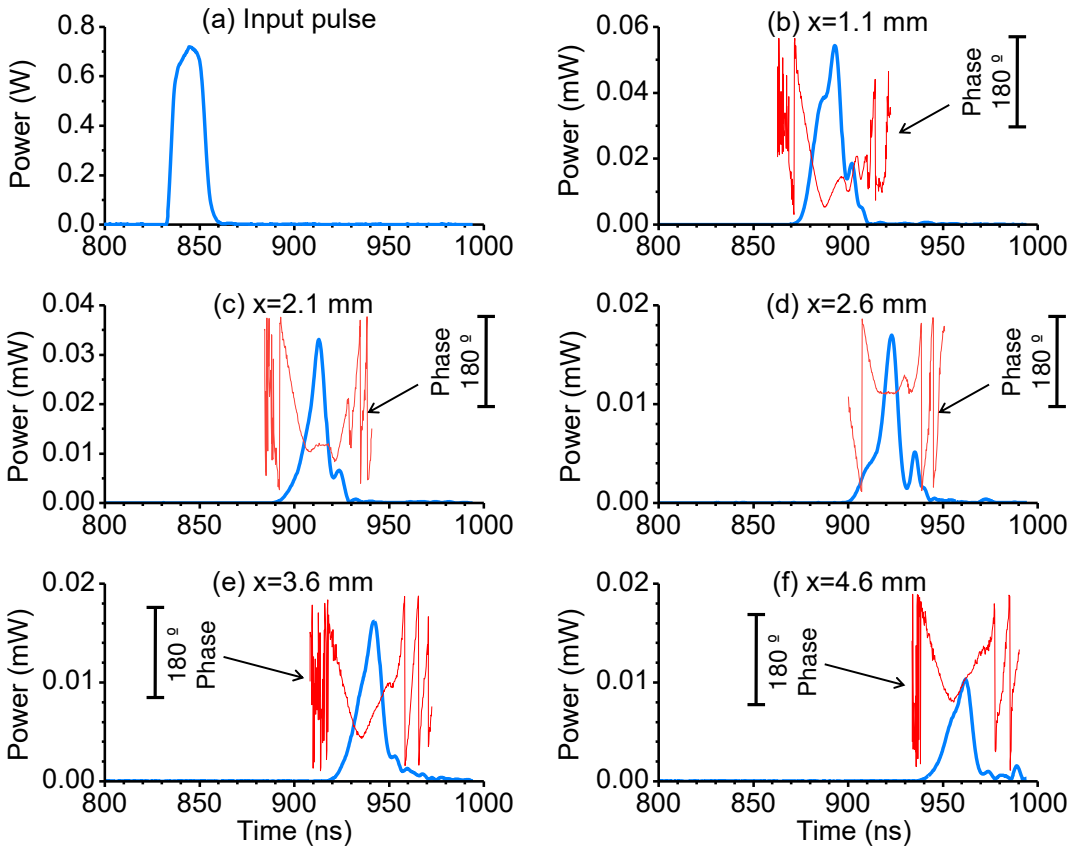

Figure 38. Spatial formation of a spin-wave soliton in a 0.2-mm-wide YIG strip. (a) Profile of an input signal. (b)-(f) Profiles of output signals measured by an inductive probe placed at different distances (x) from the input transducer. The red curves in (b) and (f) are the corresponding phase profiles.

The data in Figure 38 show the spatial evolution of a spin-wave packet. At x=1.1 mm, the packet has a width similar to that of the input pulse. As the packet propagates to x=2.1 mm, it develops into a soliton, which is not only much narrower than both the initial pulse and the packet at x=1.1 mm but also has a constant phase at its center portion, as shown in (c). At x=2.6 mm, the packet has a lower amplitude due to the magnetic damping but still maintains its solitonic nature, as shown in (d). As the packet continues to propagate further, it loses its solitonic properties and undergoes self-broadening, as shown in (e) and (f), due to significant reduction in amplitude. Note that the phase profiles for all the signals in (b), (e), and (f) are not

constant. These results support the above-drawn conclusion, namely, that it is possible to produce a bright soliton from a surface spin-wave packet.

The data in Figure 38 also indicate the other two important results. (1) The development of a soliton takes a certain distance, about 2 mm for the above-cited conditions, due to the fact that the nonlinearity effect needs a certain propagation distance to develop. (2) The soliton exists only in a relatively short range, about 1-2 mm for the above-cited conditions, due to the damping of carrier spin waves. To increase the "life" distance or lifetime of a spin-wave soliton, one can take advantage of parametric pumping (Bagada, Melkov, Serga, & Slavin, 1997) or active feedback (Wu M. , 2011) techniques.

7.4 **Simulation results with modified NLS equation**

As mentioned above, the soliton formation presented here is contradictory to the standard NLSE model. However, it can be reproduced by numerical simulations based on the equation

$$i\left[\frac{\partial u}{\partial t}+v_g\frac{\partial u}{\partial x}+\eta u\right]-\frac{1}{2}D\frac{\partial^2 u}{\partial x^2}+\left(N|u|^2+S|u|^4\right)u=0 \tag{7.1}$$

where u is the amplitude of a spin-wave packet, x and t are spatial and temporal coordinates, respectively, v_g is the group velocity, η is the damping coefficient, D is the dispersion coefficient, and N and S are the cubic and quintic nonlinearity coefficients, respectively. The quantic nonlinearity term is included because the cubic nonlinearity is insufficient to capture the experimental observations presented above. This additional term is an expansion to the lowest order of saturable nonlinearity. The simulations used the split-step method to solve the derivative terms with respect to x and used the Runge-Kutta method to solve the equation with the rest of the terms. (Weideman & Herbst, 1986; Pathria & Morris, 1990) A high-order Gaussian profile was taken in simulations for the input pulse because it is much closer to the

experimental situation than a squared pulse. The use of a square pulse as in the input pulse gave rise to numerical noise due to the discontinuity at the pulse's edges. The use of a fundamental Gaussian function did not considerably change the simulation results. It should be noted that both the standard and modified NLSE models are for nonlinear waves in one-dimensional (1D) systems, and previous work had demonstrated the feasibility of using the 1D NLSE models to describe nonlinear spin waves in quasi-1D YIG film strips. (Zhang, et al., 1998; Wang, Sun, Wu, Tiberkevich, & Slavin, 2011)

Figure 39 shows representative results obtained for different initial pulse amplitudes (u_0), as indicated. In each panel, the left and right diagrams show the power and phase profiles, respectively. The simulations were carried out for a 20-mm-long 1D film strip and a total propagation time of 250 ns. The film strip was split into 9182 steps, and the temporal evolution step was set to 0.05 ns. The input pulse was a high-order Gaussian profile with an order number of 20 and a half-power width of 15 ns. The other parameters used are as follows: v_g=3.8×10^6 cm/s, η=3.1×10^6 rad/s, D=-4.7×10^3 rad·cm^2/s, N=-10.1×10^9 rad/s, and S=1.8×10^{12} rad/s. Among these parameters, v_g, D, η, and N were calculated according to the properties of the YIG film, and the S was optimized for the reproduction of the experimental responses.

The profiles in Figure 39 indicate that, at low initial power, the pulse is broader than the initial pulse and has a phase profile which is not constant at the pulse center, as shown in (a) and (b); at relatively high power, however, the pulse is not only significantly narrower than the initial pulse but also has a constant phase across its center portion, as shown in (c). These results agree with the experimental results presented above.

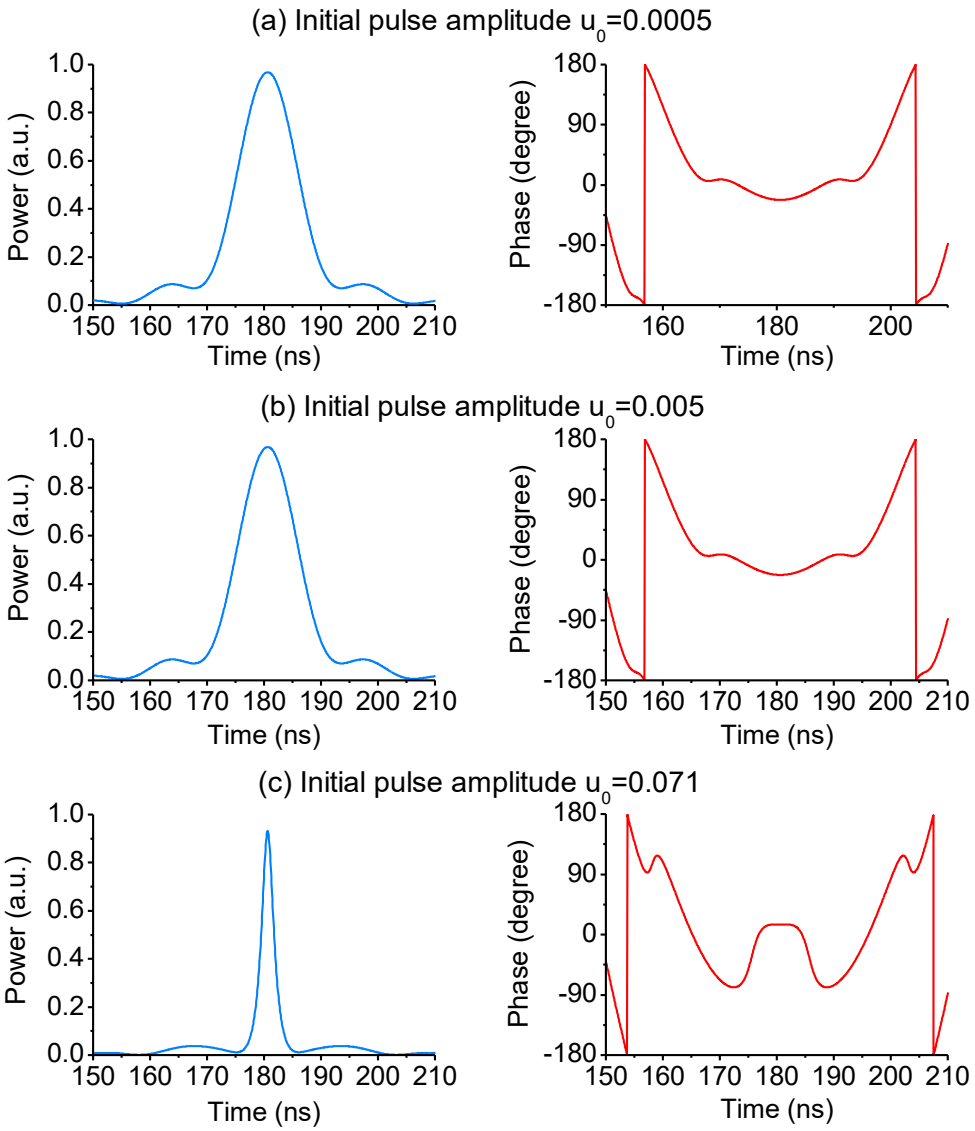

Figure 39. Power (left) and phase (right) profiles of spin-wave packets propagating in a YIG strip. The profiles were obtained from simulations with different initial pulse amplitudes, as indicated, for a propagation distance of 4.9 mm.

The reproduction of the experimental responses with the modified NLSE model indicates the underlying physical processes for the formation of bright solitons from surface spin-wave packets. In comparison with the standard NLSE, the additional terms in the modified equation are ηu and $S|u|^4 u$. The term ηu accounts for the damping of spin waves in YIG films,

while the term $S|u|^4 u$ is needed for the reproduction of the experimental responses. Since the sign of *S* was opposite to that of *N*, the term $S|u|^4 u$ played a role opposite to $N|u|^2 u$ and caused nonlinearity saturation. In particular, for the configuration cited for Figure 39(c) the term $S|u|^4 u$ overwhelmed the term $N|u|^2 u$, resulting in a repulsive-to-attractive nonlinearity transition and the formation of a bright soliton. Thus, one can see that the saturable nonlinearity played a critical role in the formation of the bright solitons from surface spin-wave packets. It should be noted that the saturable nonlinearity has been known as a critical factor for the formation of solitons in optical fibers. (Gratz & Herrmann, 1991).

In summary, this chapter reports the first observation of the formation of bright solitons from surface-spin-wave packets propagating in YIG thin films. The formation of such solitons was observed in YIG film strips with significantly different widths. The spatial evolution of the solitons was measured by placing an inductive probe at different positions along the YIG strip. The experimental observation was reproduced by numerical simulations based on a modified NLSE model. The agreement between the experimental and numerical results indicates that the saturable nonlinearity played important roles in the soliton formation.

CHAPTER 8

SUMMARY AND OUTLOOK

This chapter summarizes the work presented in this thesis and suggests future work that is relevant to this work and is of great interest.

8.1 Summary and conclusion

In order to realize an easy control of spin waves propagating in magnetic films and mitigate the spin-wave damping problem for future applications, a method based on the spin Hall effect has been developed and demonstrated. It is shown that, by growing a nanometer thick Pt film on the top of a YIG thin film, the damping of the YIG film can be controlled by applying an electrical current through the Pt capping layer. The mechanism is explained by the fact that the spin current is generated due to the spin Hall effect in the Pt layer which exerts a torque onto the magnetic moments in the YIG film. A summary of the results was published in an Applied Physics Letters paper (Wang, *et al.*, 2011). It is further shown that, the amplitude of spin waves propagating in the YIG film can be controlled by utilizing this method. A maximum of 30% change in amplitude has been reported in a Physical Review Letters paper (Wang, Sun, Wu, Tiberkevich, and Slavin, 2011). A more than 10 dB amplification/attenuation in amplitude is also demonstrated with larger input currents through the Pt film. A manuscript of the results is in preparation.

This thesis also reports the excitations of several new types of solitons. First, the excitation of chaotic spin wave solitons in magnetic film feedback rings was demonstrated for the first time. A paper that reports the main experimental and simulation results was published in another Physical Review Letter paper (Wang, *et al.*, 2011). The excitations of a pair of black solitons

with two 180^{o} phase jump were also demonstrated for the first time. This observation competes the observation of the most fundamental solitons predicted by the NLS model. At the same time, the excitations of bright solitons in a medium with repulsive nonlinearity were demonstrated, which was further explained by a simulation work based on a high-order NLS model. Several papers are in preparation to report the above results.

8.2 **Future work**

For the interaction between the spin currents produced by the spin Hall effect and the magnetic moments in ferromagnetic insulators, a lot of work still needs to be done. First, an effort can be made to search for new materials that can give larger spin Hall angles than Pt. Recently, β-tantalum has been found as a material that can generate spin currents with an intensity several times larger than that of Pt (Liu, *et al.*, 2012). It is possible that there are other heavy metals which will give an even larger spin Hall angle than β-tantalum. Second, the Pt film used in this study has a negative effect, namely, that it can severely increase the damping of the adjacent magnetic material. It still has to be understood why the damping is increased so much after a Pt layer is grown on the top of a YIG film. New materials, such as β-tantalum, however, do not lead to a significant increase in the damping of the adjacent magnetic material. At last, it might be possible that, by growing Pt/Ta on the top of low-damping YIG films, the magnetization switching can be realized by the use of the spin current generated via the spin Hall effect. Such magnetization switching has already been demonstrated in magnetic metallic materials (Liu, *et al.*, 2012). To realize the magnetization switching in a magnetic insulator, two things need to be done. First, a method to grow ultra-thin YIG films with small damping has to be found. The spin current required to switch magnetic moments is expected to be proportional to the damping constant of the magnetic material (Ralph and Stiles, 2008).

Therefore, a low-damping YIG film is critical to realize the magnetization switching with spin currents. Second, a metallic material with a large spin Hall angle needs to be found. This material, at the same time, should not increase the damping of the YIG film when it is deposited on the YIG film. β-tantalum may be a good candidate. This, however, still needs to be further investigated.

On the nonlinear spin wave side, future work on the roles and physics explanations of the additional terms in the high-order NLS equation will be of great interest. In this work, in order to explain the behavior of chaotic solitons and also bright solitons excited in media with repulsive nonlinearity, additional terms have been added into the NLS equation. However, the underlying physics behind the addition of each term is still not very clear. Additionally, other possibilities of nonlinear excitations, for example, solitons with chaotic spin waves as the carrier waves (Wu, 2011), are very interesting from the fundamental point of view and deserves further investigations.

REFERENCES

Ablowitz, M. J., & Horikis, T. P. (2009). *Physical Review A*, 79,063845.

Ablowitz, M. J., & Segur, H. (1985). *Solitons and the Inverse Scattering Transform.* Philadelphia: SIAM.

Adam, J. D., Davis, L. E., Dionne, G. F., Schloemann, E. F., & Stitzer, S. N. (2002). *IEEE Transactions on Microwave Theory and Techniques*, 50, 721.

Addison, P. S. (1997). *Fractals and Chaos.* Bristol: Institue of Physics.

Agustsson, J. S., Arnalds, U. B., Ingason, A. S., Gylfason, K. B., Johnsen, K., Olafsson, S., & Gudmundsson, J. T. (2008). *Journal of Physics: Conference Series*, 100, 082006.

Akhmediev, N., Soto-Crespo, J. M., & Town, G. (2001). *Physical Review E*, 63, 056602.

Amo, A., Lefrere, J., Pigeon, S., Adrados, C., Ciuti, C., Carusotto, I., . . . Bramati, A. (2009). *Nature Physics*, 5,805.

Ando, K., Takahashi, S., Harii, K., Sasage, K., Ieda, J., Maekawa, S., & Saitoh, E. (2008). *Physical Review Letters*, 101, 036601.

Bagada, A. V., Melkov, G. A., Serga, A. A., & Slavin, A. N. (1997). *Physical Review Letters*, 79, 2137.

Bance, S., Schrefl, T., Hrkac, G., Goncharov, A., Allwood, D. A., & Dean, J. (2008). *Journal of Applied Physics*, 103, 07E735.

Barashenkov, I. V., & Makhankov, V. G. (1988). *Phys. Lett. A*, 128, 52.

Bauer, M., Mathieu, C., Demokritov, S. O., Hillebrands, B., Kolodin, P. A., Kostylev, M. P., . . . Slavin, A. N. (1998). *IEEE Transactions on Magnetics*, 34, 1381.

Beginin, E. N., Grishin, S. V., & Sharaevsky, Y. P. (2008). *JETP Letters*, 88,647.

Bischof, B., Slavin, A. N., Benner, H., & Kivshar, Y. (2005). *Physical Review B*, 71, 104424.

Blow, K. J., & Doran, N. J. (1985). *Phys. Lett.*, 107A, 55.

Bouchbinder, E. (2003, Decemeber). *The Nonlinear Schrodinger Equation.* Retrieved from http://lvov.weizmann.ac.il/Course/Non-Linear-ShredingerEq.pdf

Bullough, R. K., & Caudrey, P. J. (1980). *Solitons.* New York: Springer-Verlag.

Burtsev, S., Camassa, R., & Timofeyev, I. (1998). *Journal of Computational Physics*, 147, 166.

Chen, M., Tsankov, M. A., Nash, J. M., & Patton, C. E. (1993). *Physical Review Letters*, 82, 2583.

Chen, M., Tsankov, M. A., Nash, J. M., & Patton, C. E. (1994). *Physical Review B*, 49,12773.

Chen, Z., Mitchell, M., & Segev, M. (1996). *Opt. Lett.*, 21, 716.

Chen, Z., Segev, M., Singh, S. R., Coskun, T. H., & Christodoulides, D. N. (1997). *J. Opt. Soc. Am. B*, 14, 1407.

Craik, D. J. (1975). *Magnetic Oxide.* London: John Wiley.

Day, C. (2005). *Physics Today*, 58 No. 2, 17.

Dehghan, M., & Taleei, A. (2010). *Numerical Methods for Partial Differential Equations*, 26, 979.

Demidov, V. E., & Kovshikov, N. G. (1998). *Technique Physics Letters*, 24(4), 274.

Demokritov, S. O., Serga, A. A., Demidov, V. E., Hillebrands, B., Kostylev, M. P., & Kalinikos, B. A. (2003). *Nature*, 426,159.

Dimitriev, A. S., Kyarginskii, B. E., Panas, A. I., Puzikov, D. Y., & Starkov, S. O. (2003). *Technique Physical Letters*, 29(1), 72.

Dmitriev, V. F., & Kalinikos, B. A. (1988). Excitation of propagating magnetization waves by microstrip transducers. *Izv. Vvssh. Uchebn. Zaved. Fiz.*, Vol. 31, No. 11, 24-53.

Dyakonov, M. I., & Perel, V. I. (1971). *JETP Letters*, 13, 467.

Dyakonov, M. I., & Perel, V. I. (1971). *JETP Letters*, 13, 467.

Eshbach, J. R., & Damon, R. W. (1960). *Phys. Rev.*, 118, 1208.

Fuchs, G. D., Sankey, J. C., Pribiag, V. S., Qian, L., Braganca, P. M., Garcia, A. G., . . . Buhrman, R. A. (2007). *Applied Physics Letters*, 91, 062507.

Gilbert, T. (1955). *Physical Review*, 100, 1243.

Gratz, S., & Herrmann, J. (1991). *J. Opt. Soc. Am. B*, 8, 2296.

Gurevich, A. G., & Melkov, G. A. (1996). *Magnetization Oscillations and Waves.* New York: CRC Press.

Hagerstrom, A. M., Tong, W., Wu, M., Kalinikos, B. A., & Eykholt, R. (2009). *Physical Review Letters*, 102, 207202.

Hagerstrom, A. M., Wu, M., Eykholt, R., & Kalinikos, B. A. (2011). *Physical Review B*, 83, 104402.

Ham, D., Li, X., & Ricketts, D. S. (2006). *IEEE Comm. Mag.*, 44,126.

Hasegawa, A., & Kodama, Y. (1995). *Solitons in Optical Communications.* New York: Oxford.

Heinrich, B., & Bland, J. A. (2005). *Ultrathin Magnetic Structures: Fundamentals.* Berlin: Springer.

Hirsch, J. E. (1999). Spin Hall Effect. *Physical Review Letters*, 83, 1834–1837.

Hook, J. R., & Hall, H. E. (1991). *Solid State Physics.* John Wiley & Sons.

James, C. W., & Tukey, J. W. (1965). *Math. Comput.*, 19, 297.

Jedema, F. J., Filip, A. T., & Wees, B. J. (2001). *Nature*, 410, 345.

Kabos, P., & Stalmachov, V. S. (1994). *Magnetostaic Waves and Their Applications.* London: Chapman and Hall.

Kajiwara, Y., Harii, K., Takahashi, S., Ohe, J., Uchida, K., Mizuguchi, M., . . . Saitoh, E. (2010). *Nature*, 464, 262.

Kalarickal, S. S., Krivosik, P., Das, J., Kim, K. S., & Patton, C. E. (2008). *Physical Review B*, 77, 054428.

Kalinikos, B. A. (1980). *IEEE Proc. 127*, 4-10.

Kalinikos, B. A., & Slavin, A. N. (1986). *J. Phys. C: Solid State Phys.*, 19, 7013.

Kalinikos, B. A., Kovshikov, N. G., & Patton, C. E. (1997). *Physical Review Letters*, 78,2827.

Kalinikos, B. A., Kovshikov, N. G., & Slavin, A. N. (1983). *JETP Letters*, 38, 413.

Kalinikos, B. A., Kovshikov, N. G., & Slavin, A. N. (1988). *Zh. Eksp. Teor. Fiz.*, 94, 159.

Kalinikos, B. A., Scott, M. M., & Patton, C. E. (2000). *Physical Review Letters*, 84, 4697.

Karar, A. S., Smy, T., & Steele, A. L. (2008). *IEEE J. Quantum Electronics*, 44,254.

Kevrekidis, P. G., Frantzeskakis, D. J., & Carretero-Gonzalez, R. (2008). *Emergent Nonlinear Phenomena in Bose-Einstein Condensates.* Berlin: Springer-Verlag.

Kevrekkidis, P. G., Frantzeskakis, D. J., & Carretero-Gonzalez, R. (2008). *Emergent Nonlinear Phenomena in Bose-Einstein Condensates.* Berlin: Springer-Verlag.

Khitun, A., Bao, M., & Wang, K. L. (2010). *Journal of Physics D: Applied Physics*, 43, 264005.

Kivshar, Y. S., & Agrawal, G. P. (2003). *Optical Solitons.* New York: Academic.

Kivshar, Y. S., & Luther-Davies, B. (1998). *Phys. Rep.*, 298, 81.

Kolodin, P. A., Kabos, P., Patton, C. E., Kalinikos, B. A., Kovshikov, N. G., & Kostylev, M. P. (1998). *Physical Review Letters*, 80, 1976.

Kolodin, P. A., Kabos, P., Patton, C. E., Kalinikos, B. A., Kovshikov, N. G., & Kostylev, M. P. (1998). *Physical Review Letters*, 80, 1976.

Kovalev, A. S., & Kosevich, A. M. (1976). *Fiz. Nizk. Temp*, 2, 913.

Krivosik, P., & Patton, C. E. (2010). *PHYSICAL REVIEW B*, 82, 184428.

Krokel, D., Halas, N. J., Giuliani, G., & Grischkowsky, D. (1988). *Phys. Rev. Lett.* , 60, 29.

Laudau, L. D., & Lifshitz, E. M. (1935). Theory of the dispersion of magnetic permeability in ferromagnetic bodies. *Phys. Z. Sowietunion*, 8, 153.

Liu, L., Moriyama, T., Ralph, D. C., & Buhrman, R. A. (2011). *Physical Review Letters*, 106, 036601.

Liu, L., Pai, C., Li, Y., Tseng, H. W., Ralph, D. C., & Buhrman, R. A. (2012). *Science*, 336, 555.

Liu, T., & Vignale, G. (2011). *Physical Review Letters*, 106, 247203.

Liu, Z., Zhu, X., Hu, W., & Jiang, F. (2007). *Int. J. Bifurcation Chaos*, 17,1735.

Luo, L., Tee, T., & Chu, P. (1998). *J.Opt.Soc.Am.B*, 15,972.

Luther-Davies, B., & Yang, X. (1992). *Opt. Lett.*, 17, 496.

Mosendz, O., Vlanminck, V., Pearson, J. E., Fradin, F. Y., Bauer, G. E., Bader, S. D., & Hoffmann, A. (2010). *Physical Review B*, 82, 214403.

Nash, J. M., Kabos, P., Staudinger, R., & Patton, C. E. (1998). *J. Appl. Phys.*, 83, 2689.

Niimi, Y., Morata, M., Wei, D. H., Deranlot, C., Basletic, M., Hamzic, A., . . . Otani, Y. (2011). *Physical Review Letters*, 99, 126601.

Orszag, S. (1969). *Phys. Fluids Supp. II*, 12, 250.

Pathria, D., & Morris, J. L. (1990). *J. Comp. Phys.*, 87, 108.

Ralph, D. C., & Stiles, M. D. (2008). *Journal of Magneization and Magnetic Materials*, 320, 1190.

Remoissenet, M. (1999). *Waves Called Solitons: Concepts and Experiments.* Berlin: Springer-Verlag.

Ricketts, D. S., Li, X., & Ham, D. (2006). *IEEE Trans. Microw. Theory Techn.*, 54,373.

Rosenstein, M. T., Collins, J. J., & De Luca, C. J. (1993). *Physica D*, 65,117.

Schneider, T., Serga, A. A., Leven, B., Hillebrands, B., Stamps, R. L., & Kostylev, M. P. (2008). *Applied Physics Letters*, 92, 022505.

Scott, M. M. (2002). *Nonlinear magnetostatic spin waves: Induced modulational instability and envelope solitons.* PhD Thesis.

Scott, M. M., Kostylev, M. P., Kalinikos, B. A., & Patton, C. E. (2005). *Physical Review B*, 71, 174440.

Scott, M. M., Patton, C. E., Kostylev, M. P., & Kalinikos, B. A. (2004). *Journal of Applied Physics*, 95, 6294.

Serga, A. A., Andre, A., Demokritov, S. O., Hillebrands, B., & Slavin, A. N. (2004). *Journal of Applied Physics*, 95, 6607.

Slavin, A. N., & Zaspel, C. E. (2002). *Journal of Applied Physics*, 91, 8673.

Slavin, A. N., Kivshar, Y. S., Ostrovskaya, E. A., & Benner, H. (1999). *Physical Review Letters*, 82, 2583.

Soto-Crespo, J. M., & Akhmediev, N. (2004). *Physical Review E*, 70,066612.

Soto-Crespo, J. M., & Akhmediev, N. (2005). *Physical Review Letters*, 95,024101.

Sparks, M. (1964). *Ferromagnetic-relaxation Theory.* New York: McGraw-Hill.

Stancil, D. D. (1993). *Theory of Magnetostatic Waves.* Springer-Verlag.

Stancil, D. D., & Prabhakar, A. (2009). *Spin Waves: Theory and Applications.* New York: Springer.

Sulem, C., & Sulem, P. L. (1999). *The nonlinear Schrodinger equation: self-focusing and wave collpse.* New York: Springer.

Takahashi, S., Saitoh, E., & Maekawa, S. (2009). *Journal of Physics Conference Series*, 200, 062030.

Takahashi, S., Saitoh, E., & Maekawa, S. (2010). *Journal of Physics: Conference Series*, 200, 062030.

Taya, M., Bashaw, M. C., Fejer, M. M., Segev, M., & Valley, G. C. (1996). *Opt. Lett.*, 21, 943.

Ustinov, A. B., & Kalinikos, B. A. (2007). *Applied Physics Letters*, 25, 252510.

Ustinov, A. B., & Kalinikos, B. A. (2008). *Applied Physics Letters*, 93, 102504.

Ustinov, A. B., Demidov, V. E., Kondrashov, A. V., Kalinikos, B. A., & Demokritov, S. O. (2011). *Physical Review Letters*, 106,017201.

Vila, L., Kimura, T., & Otani, Y. (2007). *Physical Review Letters*, 99, 226604.

Wang, Z., Hagerstrom, A., Anderson, J. Q., Tong, W., Wu, M., Carr, L. D., . . . Kalinikos, B. A. (2011). *Physical Review Letters*, 107, 114102.

Wang, Z., Sun, Y., Song, Y., Wu, M., Schultheiß, H., Pearson, J. E., & Hoffmann, A. (2011). *Applied Physics Letters*, 99, 162511.

Wang, Z., Sun, Y., Wu, M., Tiberkevich, V., & Slavin, A. (2011). *Physical Review Letter*, 98, 212505.

Weideman, J. A., & Herbst, B. M. (1986). *SIAM Journal on Numerical Analysis*, 23, 485.

Weiner, A. M., Heritage, J. P., Kawkins, R. J., Thurston, R. N., Kirschner, E. M., Leaird, D. E., & Tomlinson, W. J. (1988). *Phys. Rev. Lett*, 61, 2445.

Wu, M. (2011). Nonlinear Spin Waves in Magnetic Film Feedback Rings. In R. E. Stamps, *Solid State Physics, Vol 62* (pp. 163-224). Elsevier Inc. Academic Press.

Wu, M., & Kalinikos, B. A. (2008). *Physical Review Letters*, 101, 027206.

Wu, M., Hagerstrom, A. M., Eykholt, R., Kondrashov, A., & Kalinikos, B. A. (2009). *Physical Review Letters*, 102,237203.

Wu, M., Kalinikos, B. A., & Patton, C. E. (2004). *Physical Review Letters*, 93, 157207.

Wu, M., Kalinikos, B. A., & Patton, C. E. (2005). *Physical Review Letters*, 95,237202.

Wu, M., Kalinikos, B. A., Carr, L. D., & Patton, C. E. (2006). *Physical Review Letters*, 96,187202.

Wu, M., Kraemer, M. A., Scott, M. M., Patton, C. E., & Kalinikos, B. A. (2004). *Physical Review B*, 70, 054402.

Xia, H., kabos, P., Staudinger, R. A., Patton, C. E., & Slavin, A. N. (1998). *Physical Review B*, 58,2708.

Zhang, H. Y., Kabos, P., Xia, H., Staudinger, R. A., Kolodin, P. A., & Patton, C. E. (1998). *J. Appl. Phys.*, 84, 3776.

Zhang, Y. H., Lu, K. Q., Guo, J. B., Li, K. H., & Liu, B. Y. (2012). *Eur. Phys. J. D*, 66, 65.

Zhao, L., Tang, D. Y., & Liu, A. Q. (2006). *Chaos*, 16,013128.